ROYAL INSTITUTE
OF TECHNOLOGY

Ferroelectric domain engineering and characterization for photonic applications

Simonetta Grilli

Doctoral Thesis

Department of Physics
Royal Institute of Technology
Stockholm, Sweden 2006

Royal Institute of Technology
Laser Physics and Quantum Optics
Albanova
Roslagstullsbacken 21
SE-10691 Stockholm, Sweden

TRITA-FYS 2006:40
ISSN 0280-316X
ISRN KTH/FYS/--06:40--SE

ISBN 91-7178-382-2

Cover picture: Optical diffraction pattern from a $LiNbO_3$ crystal engineered with an hexagonal periodic surface structure.

Ferroelectric domain engineering and characterization for photonic applications

© Simonetta Grilli, 2006

Grilli, Simonetta
Ferroelectric domain engineering and characterization for photonic applications
Laser Physics and Quantum Optics, Department of Physics, Royal Institute of Technology,
SE – 10691 Stockholm, Sweden.
TRITA-FYS 2006:40
ISSN 0280-316X
ISRN KTH/FYS/--06:40--SE
ISBN 91-7178-382-2

Abstract

Lithium niobate ($LiNbO_3$) and $KTiOPO_4$ (KTP) are ferroelectric crystals of considerable interest in different fields of optics and optoelectronics. Due to its large values of the nonlinear optical, electro-optic (EO), piezoelectric and acousto-optical coefficients, $LiNbO_3$ is widely used for laser frequency conversion using the quasi-phase matching (QPM) approach where the sign of nonlinearity has been periodically modulated by electric field poling (EFP). In the microwave and telecommunication field $LiNbO_3$ is used for surface acoustic devices and integrated optical modulators. KTP and its isomorphs, on the other hand, exhibit slightly lower nonlinear coefficients but have much higher photorefractive damage thresholds, so that it is mainly used in the fabrication of QPM devices for both UV, IR and visible light generation and in high power applications.

This thesis focus on different key issues: (1) accurate characterization of specific optical properties of $LiNbO_3$, which are of interest in nonlinear and EO applications; (2) *in-situ* visualization and characterization of domain reversal by EFP in $LiNbO_3$ and KTP crystals for a through understanding of the ferroelectric domain switching; (3) fabrication of periodic surface structures at sub-micron scale in $LiNbO_3$ for photonic applications. An interferometric method is used for accurate measurement of ordinary and extraordinary refractive indices in uniaxial crystals, which is of great interest in the proper design of QPM crystals. A digital holography (DH) based method is presented here for 2D characterization of the EO properties of $LiNbO_3$, which is considerably interesting in the applications where the proper design of the EO device requires a spatially resolved information about the EO behaviour and the existing pointwise techniques are not sufficient. A DH method for novel *in-situ* monitoring of domain reversal by EFP in both $LiNbO_3$ and KTP, is also presented here. The technqiue could be used as a tool for high fidelity periodic domain engineering but also provides information about domain kinetics, internal field and crystals defects.

Finally this thesis presents novel results concerning nanoscale periodic surface structuring of congruent $LiNbO_3$. Holographic lithography (HL) is used for sub-micron period resist patterning and electric overpoling for surface domain reversal. Surface structures are obtained by selective etching. Moiré effect is also used in the HL to fabricate complicated structures with multiple periods. The depth compatibility with waveguide implementation allows foreseeing possible applications of these structures for Bragg gratings or innovative photonic crystal devices, exploiting the additional nonlinear and EO properties typical of $LiNbO_3$.

Keywords: $LiNbO_3$, $KTiOPO_4$, interferometry, digital holography, electric field poling, electro-optic materials, holographic lithography, ferroelectric domains, nanostructures, microstructures.

To Luigi.

It pleases me as much to doubt as to know
Dante Alighieri, La Divina Commedia

Preface

The work presented in this thesis is the result of the doctoral studies started about four years ago in the Laser Physics and Quantum Optics Group, Department of Physics, at the Royal Institute of Technology (KTH). The experimental work has been performed partly in KTH and partly at the National Institute of Applied Optics (INOA) of the National Council of Research (CNR) in Naples, Italy, where I was holder of a Research Grant first and recently of a Researcher position.

The research work performed at the INOA laboratories have been funded by the Italian Ministero dell'Istruzione dell'Università e della Ricerca (MIUR) within the two Projects: *Microdispositivi fotonici in niobato di litio* (FIRB n. RBNE01KZ94); *Circuiti fotonici integrati per le telecomunicazioni ottiche e la sensoristica* (n. 77 DD n. 1105/2002).

This thesis consists of an introductory part providing a background to the work performed and the reprints of the publications.

List of publications

Publications included in the thesis

I. S. Grilli, P. Ferraro, S. De Nicola, A. Finizio, G. Pierattini, R. Meucci, "Whole optical wavefields reconstruction by digital holography," Optics Express 9, 294 (2001). http://www.opticsinfobase.org/abstract.cfm?id=65208

II. S. De Nicola, P. Ferraro, A. Finizio, P. De Natale, S. Grilli, G. Pierattini, "A Mach-Zehnder interferometric system for measuring the refractive indices of uniaxial crystals," Optics Communications 202, 9 (2002).

III. M. de Angelis, S. De Nicola, A. Finizio, G. Pierattini, P. Ferraro, S. Grilli, M. Paturzo, L. Sansone, D. Alfieri, P. De Natale, "Two-dimensional mapping of electro-optic phase retardation in lithium niobate crystals by digital holography," Optics Letters 30, 1671 (2005).

IV. S. Grilli, P. Ferraro, M. Paturzo, D. Alfieri, P. De Natale, M. de Angelis, S. De Nicola, A. Finizio, G. Pierattini, "*In-situ* visualization, monitoring and analysis of electric field domain reversal process in ferroelectric crystals by digital holography," Optics Express 12, 1832 (2004). http://www.opticsinfobase.org/abstract.cfm?id=79763

V. S. Grilli, P. Ferraro, D. Alfieri, P. De Natale, C. Canalias, V. Pasiskevicius, F. Laurell, "Characterization of fast dynamic evolution of ferroelectric domains in KTiOPO4 by digital holography," submitted to Optics Express.

VI. C. Canalias, V. Pasiskevicius, F. Laurell, S. Grilli, P. Ferraro, P. De Natale, "*In-situ* visualization of domain kinetics in flux grown $KTiOPO_4$ by digital holography," submitted to Applied Physics Letters.

VII. M. de Angelis, S. De Nicola, A. Finizio, G. Pierattini, P. Ferraro, S. Grilli, M. Paturzo, "Evaluation of the internal field in lithium niobate ferroelectric domains by an interferometric method," Applied Physics Letters 85, 2785 (2004).

VIII. M. Paturzo, D. Alfieri, S. Grilli, P. Ferraro, P. De Natale, M. de Angelis, S. De Nicola, A. Finizio, G. Pierattini, "Investigation of electric internal field in congruent $LiNbO_3$ by electro-optic effect," Applied Physics Letters 85, 5652 (2004).

IX. M. Paturzo, P. Ferraro, S. Grilli, D. Alfieri, P. De Natale, M. de Angelis, A. Finizio, S. De Nicola, G. Pierattini, F. Caccavale, D. Callejo, A. Morbiato, "On the origin of internal field in lithium niobate crystals directly observed by digital holography," Optics Express 13, 5416 (2005). http://www.opticsinfobase.org/abstract.cfm?id=84907

X. S. De Nicola, P. Ferraro, A. Finizio, S. Grilli, G. Coppola, M. Iodice, P. De Natale, M. Chiarini, "Surface topography of microstructures in lithium niobate by digital holographic microscopy," Measurement Science and Technology 15, 961 (2004).

XI. S.Grilli, P. Ferraro, S. De Nicola, A. Finizio, G. Pierattini, P. De Natale, M. Chiarini, "Investigation on reversed domain structures in lithium niobate crystals patterned by interference lithography," Optics Express 11, 392 (2003). http://www.opticsinfobase.org/abstract.cfm?id=71299

XII. S. Grilli, P. Ferraro, P. De Natale, B. Tiribilli, M. Vassalli, "Surface nanoscale periodic structures in congruent lithium niobate by domain reversal patterning and differential etching," Applied Physics Letters 87, 233106 (2005) [selected for The Virtual Journal of Nanoscale Science & technology].

XIII. S. Grilli, P. Ferraro, L. Sansone, M. Paturzo, S. De Nicola, G. Pierattini, P. De Natale, "Double-face and submicron two-dimensional domain patterning in congruent lithium niobate," IEEE Photonics Technology Letters 18, 541 (2006).

XIV. S. Grilli, C. Canalias, F. Laurell, P. Ferraro, P. De Natale, "Control of lateral domain spreading in congruent lithium niobate by selective proton exchange," accepted by Applied Physics Letters.

XV. G. Coppola, P. Ferraro, M. Iodice, S. De Nicola, S. Grilli, D. Mazzotti, P. De Natale, "Visualization of optical deflection and switching operations by a domain-engineered-based $LiNbO_3$ electro-optic device," Optics Express 11, 1212 (2003). http://www.opticsinfobase.org/abstract.cfm?id=72392

Publications not included in the thesis

A1. S. De Nicola, P. Ferraro, A. Finizio, S. Grilli and G. Pierattini, "Experimental demonstration of the longitudinal image shift in digital holography," Optical Engineering 42, 1625 (2003).

A2. E. Allaria, S. Brugioni, S. De Nicola, P. Ferraro, S. Grilli and R. Meucci, "Digital Holography at 10.6 μm," Optics Communications 215, 257 (2002).

A3. P. Ferraro, S. De Nicola, A. Finizio, G. Coppola, S. Grilli, C. Magro and G. Pierattini, "Compensation of the inherent wave front curvature in digital holographic coherent microscopy for quantitative phase contrast imaging," Applied Optics 42, 1938 (2003).

A4. E. Allaria, S. Brugioni, S. De Nicola, P. Ferraro, S. Grilli and R. Meucci, "Interferometric analysis of reorientational nonlinear phenomena at 10.6μm in a nematic liquid crystal," Applied Optics 42, 4827 (2003).

A5. S. De Nicola, P. Ferraro, G. Coppola, A. Finizio, G. Pierattini, S. Grilli, "Talbot self-image effect in digital holography and its application to spectrometry," Optics Letters 29, 1 (2004).

A6. G. Coppola, P. Ferraro, M. Iodice, S. De Nicola, A. Finizio, S. Grilli, "A digital holographic microscope for complete characterization of microelectromechanical systems," Measurement Science and Technology 15, 529 (2004).

A7. M. de Angelis, S. De Nicola, P. Ferraro, A. Finizio, S. Grilli, G. Pierattini, "Profile measurement of a one-dimensional phase boundary sample using a single shot phase-step method," Optics and Lasers in Engineering 43, 1305 (2005).

A8. P. Ferraro, S. Grilli, D. Alfieri, S. De Nicola, A. Finizio, G. Pierattini, B. Javidi, G. Coppola, V. Striano, "Extended focused image in microscopy by digital holography," Optics Express 13, 6738 (2005).

A9. P. Ferraro, D. Alfieri, S. Grilli, L. Sansone, S. De Nicola, A. Finizio, G. Pierattini, "Recovering correct phase information in multiwavelengths digital holographic microscopy by compensation of chromatic aberrations," Optics Letters 30, 2706 (2005).

A10. S. Grilli, P. Ferraro, D. Alfieri, M. Paturzo, L. Sansone, S. De Nicola, P. De Natale, "Interferometric technique for characterization of ferroelectric crystals properties and microengineering process," Fringe '05, The 5th International Workshop on Automatic Processing of Fringe Patterns, pg. 514 (Springer, W. Osten Ed.)

A11. S. Grilli, P. Ferraro, L. Sansone, M. Paturzo, S. De Nicola, A. Finizio, G. Pierattini, P. De Natale, "Engineering and characterization of ferroelectric microstructures for photonic crystal applications," Proc. SPIE 6182, 204 (2006) [Plenary Paper in the Session *Hot Topics in Photonics*].

Contents

Abstract **i**

Preface **v**

List of publications **vii**

Chapter 1. Introduction and motivations **1**
References 5

Chapter 2. General properties of $LiNbO_3$ and $KTiOPO_4$ **7**
2.1 Introduction 7
2.2 Structure and crystal growth 7
2.3 Ferroelectric properties 10
2.4 Optical properties 11
2.5 Periodic electric field poling 16
2.6 Piezoelectric properties 18
References 19

Chapter 3. Holography **21**
3.1 Introduction 21
3.2 Holography in general 21
3.2.1 Recording 21
3.2.2 Optical reconstruction 23
3.3 Digital holography 24
3.3.1 The CCD chip as a holographic recording device 24
3.3.2 Numerical reconstruction 26
3.3.3 Fresnel method 27
3.3.4 Convolution method 28
3.3.5 Comparison between Fresnel and convolution methods 29
3.4 Whole optical wavefield reconstruction by digital holography 30
3.4.1 Amplitude and phase distributions from simulated holograms 32
References 36

Chapter 4. Characterization of optical properties of $LiNbO_3$ crystals **37**
4.1 Introduction 37
4.2 Accurate measurement of the refractive indices 37
4.3 Two-dimensional mapping of the electro-optic coefficient 43
References 47

Chapter 5. Properties related to the electric field poling **49**
5.1 Introduction 49
5.2 In-situ characterization of domain switching in ferroelectric crystals 49
5.2.1 In-situ domain reversal imaging in $LiNbO_3$ by the RGI 51
5.2.2 In-situ domain reversal imaging in $LiNbO_3$ by the MZ 54
5.2.3 In-situ domain reversal imaging in $KTiOPO_4$ by the MZ 56
5.2.4 Comparison of domain switching dynamics 59
5.3 Characterization of internal field in $LiNbO_3$ 60

5.3.1 Evaluation of the static internal field 60
5.3.2 Evaluation of the elastic component of the internal field 62
5.3.3 Evidence of the internal field dependence on crystal defects 65
5.4 Topography characterization of relief structures in $LiNbO_3$ 69
5.4.1 Principle of the method 70
5.4.2 Experimental results 71
References 76

Chapter 6. Ferroelectric domain engineering for photonic applications 77
6.1 Introduction 77
6.2 Holographic lithography 77
6.3 Sub-micron domains obtained by electric field overpoling 78
6.3.1 Overpoling regime applied to 1D gratings 79
6.3.2 Overpoling regime applied to 2D gratings 81
6.4 Periodic nanoscale surface structuring by electric field overpoling 83
6.5 Complex surface structures by moiré holographic lithography 85
6.6 Double-face sub-micron surface structures 88
6.7 Possible applications for novel photonic crystal devices 90
6.8 Periodic domain engineering by proton exchange 91
References 94

Chapter 7. Electro-optic device based on domain engineered $LiNbO_3$ 95
7.1 Beam deflector 97
7.2 TIR-based switch device 101
References 103

Chapter 8. Description of the original work and author contribution 105

Chapter 9. Summary 111

List of acronyms 115

Acknowledgments 117

Papers I - XV

Chapter 1

Introduction and motivations

1.1 Background

Lithium niobate ($LiNbO_3$ or LN) and potassium titanyl phosphate ($KTiOPO_4$ or KTP) are ferroelectric nonlinear crystals widely used in the field of optics and photonics. $LiNbO_3$ was reported to be ferroelectric by Matthias and Remeika in 1949 and was grown from a lithium fluoride flux [1]. Later it was also grown from the melt by using the Czochralski pulling technique by Ballman [2] and Fedulov [3]. The interest in this material started to increase in the 1990's when a large number of technical publications related to $LiNbO_3$ began to appear in literature. The rapid growth of photonics for communications, data storage, display, biomedical and defence applications resulted in an increasing need for a versatile solid-state platform with a range of linear and nonlinear optical properties, much as silicon in semiconductor industry. The crystal growth for $LiNbO_3$ has been developed to an extent that high quality, single domain wafers of this material are nowadays commercially available at relatively low cost with diameters up to 4 inch and with significant homogeneity. Nowadays $LiNbO_3$ is widely used in the optical, laser and communications industry thanks to its high electro-optic (EO), piezoelectric (PZ), acousto-optic and nonlinear optical coefficients, transparency in a wavelength range from near UV to far infrared, large photovoltaic effect and photocurrents in doped crystals, and finally thanks to the possibility of patterning ferroelectric domains into various shapes and sizes [4]. In the field of lasers a not negligible second order nonlinear optical effect constitutes a valuable property, giving the possibility of realizing the key devices for building coherent sources emitting radiation from the UV to the IR spectral range [4,5]. This is achieved traditionally by birefringent phase-matching but in the last years much higher efficiency has been obtained in the generation of coherent radiation by using the quasi-phase-matched (QPM) interaction [6]. The laser sources emitting in the visible and UV find a wide variety of applications including fluorescent spectroscopy in bio-medicine, devices for printing and image recording, laser display systems and high-density optical storage. Those sources emitting in the near-to mid IR find main applications in the field of molecular spectroscopy including for example the development of gas sensing equipments. The operation of such QPM devices is based on the possibility of manipulating the ferroelectric crystals in order to produce ferroelectric domain structures, the so called "periodically poled" crystals, such as periodically poled LN (PPLN), which rank nowadays among the most efficient photonic components for frequency conversion applications [6]. The relatively high acousto-optic effect of $LiNbO_3$, combined with the PZ effect, gives the possibility of producing surface acoustic waves (SAW) to control light beams, with applications in the field of microwave communications as surface acoustic wave delay lines and filters [7]. In the field of fiber optic communication systems a wide variety of EO devices, such as switches and multiplexers where an electric field serves to control the light propagation along the medium, have been developed in $LiNbO_3$. In fact, $LiNbO_3$ is the EO material which best addresses the high demands in terms of switching time currently required in signal processing components. In addition the well established technology (titanium indiffused or annealed proton exchange [8]) for

waveguide fabrication in $LiNbO_3$ allows optical integration of those electro-optically controlled components.

KTP was first synthesized in 1890 by L. Ouvard [9] but it wasn't until the 1970's that Zumsteg, Bierlein and Gier identified the nonlinear optical properties of this crystal [10], which appear to be extremely desirable for several solid state laser applications. In fact, the unique combination of high nonlinear coefficients, high damage threshold and low photorefractive sensitivity makes it well suited for laser system applications requiring high power, high efficiency and/or durability. KTP can be phase matched at 1.06 μm but QPM frequency conversion processes are much more attractive for realizing nonlinear components. These, combined with diode-pumped solid-state lasers, allow the fabrication of compact and efficient new laser sources in the UV to the near-to-mid infrared wavelength range.

Periodically poled KTP (PPKTP) crystals present several advantages compared to the PPLN ones. The excellent nonlinearities of PPKTP crystals make them suitable for UV, visible and IR generation in high power applications thanks to the higher photorefractive damage threshold. The coercive field of KTP at room temperature is about one-order of magnitude lower than that of congruent $LiNbO_3$ so that thicker periodically poled structures can be easily fabricated giving access to higher optical powers. Moreover the anisotropic lattice structure of KTP limits the domain broadening [11], thus favouring the fabrication of dense domain gratings. Anyway KTP still cannot become as popular as $LiNbO_3$ for different reasons. First of all KTP crystals cannot be grown by Czochralski method so that the KTP wafers are not as large as those of $LiNbO_3$. The KTP material exhibits ionic conductivity which makes difficult the monitoring of the poling current during electric field domain inversion, thus requiring alternative monitoring techniques [11,12]. Such ionic conductivity varies from wafer to wafer and within the same wafer, thus reducing the yield of PPKTP crystals [13].

1.2 Motivations

Several current and future applications of $LiNbO_3$ and KTP materials include efficient first-order second harmonic generation of short wavelengths in the UV range by QPM interaction, EO modulators based on Bragg diffraction and photonic crystal (PC) structures. The QPM interaction in submicron periodically poled nonlinear crystals would provide new coherent sources in the UV range which find applications in optical data storage and display systems. Compared to the conventional EO modulators, the Bragg grating based modulators would provide lower drive voltages and faster response times. In particular, Bragg grating structures operating at the typical telecom wavelengths would be of great interest to the field of telecommunications for the fabrication of different optical components such as electrically controlled Bragg reflectors, beam steering devices and narrow band filters. When a continuous electric field is applied over such a structure, the opposite domains acquire positive and negative refractive index changes, depending on their orientations, and a multilayer-index stack is generated. Such a layered refractive index structure can work as a narrow band filter, with the bandwidth and reflectivity depending upon the magnitude of the applied field and the length of the structure. PCs implemented in nonlinear materials would provide additional functionalities in respect to the ones which are being developed in semiconductor substrates, with the new possibility to manipulate light by light itself [14]. Moreover the recent development of novel manufacturing techniques able to generate periodic surface

structures in lithium niobate is attracting interest for novel applications of this material in the emerging field of photonic bandgap devices [15]. In fact, innovative PC devices based on $LiNbO_3$ would be possible by using the additional functionalities related to its strong EO, PZ, nonlinear effects. However all of these applications require submicron domain periods that fall outside the current limit of routine fabrication capability and, as is often the case, a widespread technological application of these materials is preceded by a complete understanding of many of the fundamental physical processes occurring in these materials.

The motivations of this thesis were born in this research framework. This thesis focuses on different specific areas of interest including the characterization of specific properties of $LiNbO_3$ and KTP crystals and the implementation of new techniques for ferroelectric domain engineering and surface structuring of $LiNbO_3$ substrates with submicron periods. The novel characterization work presented in this thesis include accurate measurement of the ordinary and extraordinary refractive indices of $LiNbO_3$, two-dimensional mapping of the EO behaviour in $LiNbO_3$ crystals, *in-situ* characterization of specific properties related to the electric field domain reversal in $LiNbO_3$ and KTP crystals, such as domain switching kinetics and internal field. The method for measuring the refractive indices in uniaxial crystals is based on the rotation-dependent changes of the phase shift occurring in crystal slabs due to the variation of the optical path length. The measurements are based on interferometric type procedures and allow to evaluate ordinary and extraordinary indices with great accuracy compared to other techniques previously presented in literature [16-18]. Therefore this method is of great interest to the field of nonlinear applications where proper design of the nonlinear crystals for any specific application requires an accurate knowledge of the refractive indices [19,20]. The two-dimensional mapping of the EO induced phase shift in $LiNbO_3$ crystals is performed by a digital holography (DH) based method and is motivated by the many efforts performed to investigate the EO properties of $LiNbO_3$ due to its large involvement in the fabrication of EO controlled optical modulators. In fact, many techniques, such as polarimetric Senarmont type [21] and other interferometric methods [22] have been used for this purpose. Even though relatively highly sensitive measurements are provided by these techniques, the pointwise character of such measurements limit their usefulness to a restricted range of applications. For example, the methods in [22] and therein are useful as characterization tools in case of the bulk EO modulators used for telecom applications, where the EO response is of fundamental importance and its spatially resolved characterization is not strictly required. In fact the measured coefficient comes from either integration along the probe's beam direction or from an average in its millimetre sized transverse section. On the contrary, information about the two-dimensional (2D) distribution and degree of uniformity of the EO response is required in $LiNbO_3$ based photonic applications.

The characterization of properties related to the electric field poling is based on a DH technique where the linear EO and PZ effects occurring along the z crystal axis is used in order to image *in-situ* the domain switching dynamics. This technique would be useful for high fidelity control of domain patterning of ferroelectric crystals but also as a novel non-invasive tool for investigation of crystal properties. For example results concerning the characterization of domain kinetics in KTP crystals and internal field effects occurring in congruent $LiNbO_3$ are presented in this thesis. Finally this thesis presents the recent novel results concerning the fabrication of sub-micron period reversed domain gratings in congruent $LiNbO_3$ with both 1D and 2D geometries by using a relatively easy to accomplish method based on holographic

lithography patterning and overpoling. Moreover, these domain structures are transferred into the substrate by simple wet etching in appropriate acid solutions in order to fabricate novel sub-micron surface structures which could find interesting applications in the field of PC applications.

This thesis is organized as follows. Chapter 2 provides the basic information about the LiNbO3 and KTiOPO4 crystals which are useful for the appropriate understanding of the topics treated in the successive chapters. Chapter 3 intends to provide a general knowledge of holography and particularly digital holography which is largely applied in this thesis for different high resolution characterizations. Chapter 4 presents the results concerning the accurate measurement of the ordinary and extraordinary refractive indices of LiNbO3 and those related to the 2D mapping of its EO coefficient. Chapter 5 focuses on the application of DH for the in-situ characterization of ferroelectric properties related to the electric field poling in case of both $LiNbO_3$ and $KTiOPO_4$. Chapter 6 reports the results obtained recently in the fabrication of sub-micron period reversed domain patterns in $LiNbO_3$ and moreover of surface structures with 1D and 2D geometries. Chapter 7 describes the operation of two simple EO devices engineered in $LiNbO_3$ crystals and functioning as beam deflector and optical switch. Chapter 8 describes the papers included in this thesis and the corresponding contribution by the author. Finally Chapter 9 provides a brief summary of this thesis.

References Chapter 1

[1] B.T. Matthias, J.P. Remeika, Phys. Rev. 76, 1886 (1949).

[2] A.A. Ballman, J. Am. Ceram. Soc. 48, 112 (1965).

[3] S.A. Fedulov Z.I. Shapiro, P.B. Ladyzhenskii, Kristallografiya 10, 268 (1965).

[4] A. M. Prokhorov, Y.S. Kuziminov, *Physics and Chemistry of Crystalline Lithium Niobate*, Hilger, Bristol (1990).

[5] U. Simon, F.K. Tittel, in: F.B. Dunning, R.G. Hulet (Eds.), *Atomic, Molecular and Optical Physics: Electromagnetic Radiation*, vol. 29C, p. 231, Academic Press, New York (1997).

[6] M.M. Fejer, G. A. Magel, D. H. Jundt, and R. L. Byer, IEEE J. Quantum Electron. 28, 2631 (1992).

[7] A.A. Oliver (Ed.), *Acoustic surface waves*, Topics in Applied Physics, vol.24, Sringer (1978).

[8] E.L. Wooten, K.M. Kissa, A. Yi-Yan, E.J. Murphy, D.A. Lafaw, P.F. Hallemeier, D. Maack, D.F. Attanasio, D.J. Fritz, G.J. McBrien, D.E. Bossi, IEEE J. Sel. Top. Quantum Electron. 6, 69 (2000).

[9] L. Ouvrad, M. Troost, Compt. Rend. 121, 117 (1890).

[10] J.D. Bierlein, H. Vanherzeele, J. Opt. Soc. Am. B 6, 622 (1989).

[11] J. Hellström, R. Clemens, V. Pasiskevicius, H. Karlsson, and F. Laurell, J. Appl. Phys. 90, 1489 (2001).

[12] H. Karlsson, F. Laurell, L.K. Cheng, Appl. Phys. Lett. 74, 1519 (1999).

[13] H. Karlsson, F. Laurell, Appl. Phys. Lett. 71, 3474 (1997).

[14] J.D. Joannopoulos, P. R. Villeneuve, and S. Fan, Nature 386, 143 (1997).

[15] K. Sakoda, *Optical properties of photonic crystals*, Springer Edition (2005).

[16] D.F. Heller, O. Kafri, J. Krasinnski, Appl. Opt. 33, 3037 (1985).

[17] J.C. Bhattacharya, Appl. Opt. 40, 1658 (2001).

[18] S. De Nicola, G. Carbonara, A. Finizio, G. Pierattini, Appl. Phys. B 58, 133 (1994).

[19] M.M. Fejer, G.A. Magel, D.H. Jundt, R.L. Byer, IEEE L. Quantum Electron. 28, 2631 (1992).

[20] F.D. Bloss, *An introduction to the Method of Optical Crystallography*, Holt, New York (1961).

[21] P.C. Lemaire, and M. P. Georges, Opt. Mater. 4, 182 (1995).

[22] P. Ney, A. Maillard, M. D. Fontana, and K. Polgàr, J. Opt. Soc. Am. B 17, 1158 (2000).

Chapter 2

General properties of $LiNbO_3$ and $KTiOPO_4$

2.1 Introduction

Lithium niobate ($LiNbO_3$ or LN) is a human-made dielectric material that does not exist in nature. It was first discovered to be ferroelectric in 1949 [1] and it is now one of the most widely used electro-optic (EO) materials. $LiNbO_3$ is characterized by large pyroelectric, piezoelectric (PZ), nonlinear and EO coefficients and has useful acoustic and acousto-optic properties. This richness of large-magnitude physical effects has caused LN to become widely used in applications such as acoustic wave transducers, optical amplitude modulators, second-harmonic generators, beam-deflectors, dielectric waveguides, memory elements, holographic data processing devices, and others [2]. Potassium titanyl phosphate ($KTiOPO_4$ or KTP) is a non-centro-symmetric crystalline material which was first synthesised in 1890 [3]. It has been widely used in various nonlinear-optical applications, in particular in second harmonic generation (SHG) and optical parametric oscillation (OPO) devices based on pumping with 1 µm wavelength radiation from Nd lasers. This is due to a highly attractive combination of material properties including large nonlinearity, high damage threshold, large birefringent phasematching acceptance in angle and temperature, wide transmission, and good thermal and mechanical stability [4]. KTP and some of its isomorphs are available from several vendors and are today frequently used in commercial laser devices.

2.2 Structure and crystal growth

<u>Lithium niobate</u>

The structure of LN at room temperature belongs to the 3m group and consists of planar sheets of oxygen atoms in a distorted hexagonal close-packed configuration [5]. Octahedral interstices are formed, one third of which is occupied by niobium atoms, one third by lithium atoms while the rest is vacant. Figure 2.2-1 shows the schematic view of the Li and Nb atoms position respect to the oxygen planes. Above the Curie temperature T_c (around 1210 °C) the phase is paraelectric (no spontaneous polarization) while in the ferroelectric phase below T_c LN exhibits spontaneous polarization. In the paraelectric phase the Li atoms lie in an oxygen layer that is $c/4$ away from the the Nb atom while the Nb atoms are centred between oxygen layers. Conversely, in the ferroelectric phase the elastic forces of the crystal become dominant and force the lithium and niobium ions into new positions. Figure 2.2-2 shows the conventional hexagonal unit cell for LN, where the *c* axis is defined as the axis about which the crystal exhibits three-fold rotation symmetry [5]. The three equivalent *a* axes (a_1,a_2,a_3) of the conventional hexagonal unit cell are 120° apart, lie in a plane normal to the *c* axis and are chosen to be perpendicular to the mirror planes of symmetry [5].

The ferroelectric dipole axis is aligned along the *c* axis, resulting in a *c*+ and a *c*- face, both of which are normal to the *c* axis. The *c*+ face corresponds to the positive end of the dipole which becomes negative upon compression. This is due to the free charges which deposit on the *c* faces to compensate the spontaneous polarisation,

so that negative charges deposit on the *c*+ face and positive charges on the *c*- face. Under compression the niobium and lithium ions move closer to their paraelectric positions, reducing the intensity of the dipole. This results in excess of compensating charge on the two faces, so that the positive end of the dipole exhibits a negative charge under compression.

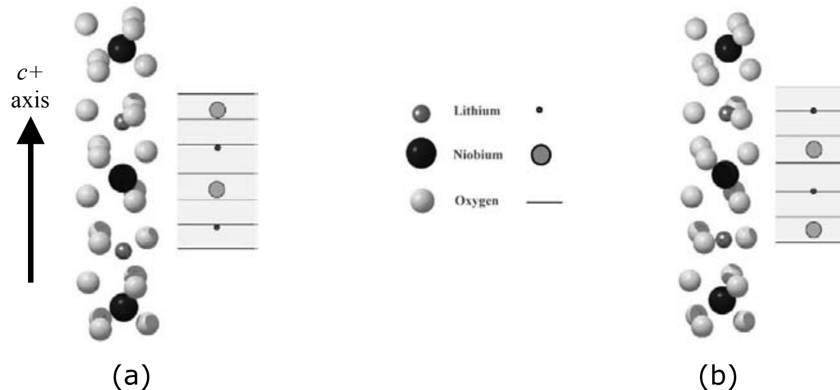

Fig. 2.2-1: Schematic view of the $LiNbO_3$ crystal structure in (a) ferroelectric phase (below T_c) and (b) paraelectric phase (above T_c). [5]

A Cartesian coordinate system (*x,y,z*) is used to describe the physical properties of LN. Conventionally, the z axis is chosen to be parallel to the *c* axis, while the *x* axis is chosen to be parallel to one of the equivalent *a* axes. The *y* axis is then chosen so that a right handed system is formed, resulting in the *y* axis lying in one of the mirror symmetry planes.

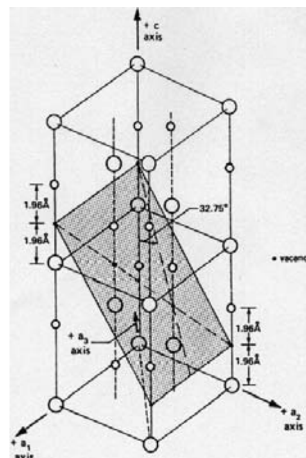

Fig. 2.2-2: Schematic view of the hexagonal unit cell of $LiNbO_3$ showing the hexagonal axes (c, a_1, a_2, a_3), where the large circles are Nb ions and small circles are the Li atoms.

LN was first grown in the early 1960s using the Czochralski technique [6]. The pure compound of the material to be grown is melted in a crucible in the growth station and a seed crystal suspended from a rotating seed rod is lowered into the furnace cavity. Growth of a crystal can be initiated by starting to slowly withdraw the seed rod so that new crystal material attaches to the solid seed. The composition of a given crystal depends on the proportions used in the starting materials. For example, the congruent composition contains 48.45 mol% Li_2O and 51.55 Nb_2O_5 [7]. In particular, stoichiometric LN (SLN), in common with many oxides, melts incongruently. Differences between stoichiometric and congruent composition LN are apparent at

the unit cell level [8]. In SLN with T_c=1470 K, the Li atom site is 100% occupied by Li and the Nb site is 100% occupied by Nb, as the O site is 100% occupied by O [8]. A SLN composition can be obtained by using a lithium rich melt or by adding K_2O during the growth process. Anyway, the growth of defect-free SLN crystals is quite difficult. Both mechanical twinning [9] and lithium excess micro-clusters are possible due to the composition variation in the melt-crystal interface during the growth of off-congruent LN crystals. However, there is not enough experimental evidence that gives a thorough understanding of such defects. Lithium excess micro-clusters are generated during the crystallization process. They are commonly present in a limited area close to the interface and come from the bottom of the crucible from which they are transported by the natural convection currents. The clusters force the formation of lithium aggregates in the crystal lattice, generating micro-regions with a different lattice structure.

Potassium titanyl phosphate

$KTiOPO_4$ belongs to the family of compounds that have the formula unit $MTiOXO_4$, where M can be K, Rb, Tl, NH4, or Cs and X can be P or As [4]. All these materials are orthorhombic and belong to the acentric point group mm2. In case of KTP the structure is characterized by chains of TiO_6 octahedra linked at two corners and by PO_4 tetrahedra which separate the chains, as shown in Fig. 2.2-3.

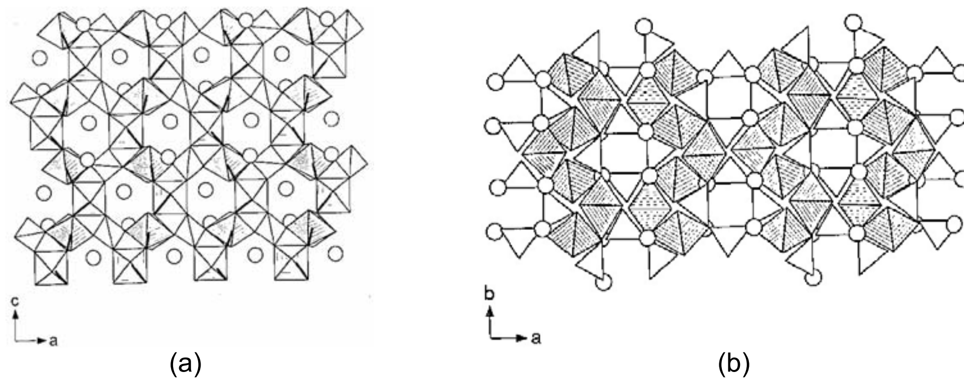

Fig. 2.2-3: Schematic view of the KTP crystal structure under (a) *a-c* projection and (b) *a-b* projection. Shaded elements are the Ti octahedra, open elements are the P tetrahedra, and open circles are the K. The short Ti-O bonds are shown as bold lines. [4]

There are two chains per unit cell. Alternating long and short Ti-O bonds occur along these chains generating a net *z* directed polarization and the major contribution to KTP's large nonlinear optic and EO coefficients. The K ions are weakly bonded to both the Ti octahedra and P tetrahedral, so that channels exist along the *z* axis whereby K can diffuse through a vacancy mechanism, with a diffusion coefficient several orders of magnitude greater than in the *xy* plane. Large single crystals of KTP can be grown by both flux and hydrothermal (Ht-KTP) techniques.

The flux technique is essentially a high-temperature solution growth process in which the KTP crystallizes out of a molten self-flux composition when cooled. Depending on the specific flux used, crystal growth can occur from approximately 700°C to approximately 1000°C. The flux is a solvent of the components of the crystal. A significant advantage of the flux process is the operation at atmospheric pressure without requiring sophisticated pressure equipment. However, to avoid growth striations and flux inclusions, uniform temperature and high levels of temperature control are required.

The hydrothermal process consists of sealing nutrient and seed crystals in a gold tube, inserting the tube into a high-pressure and high-temperature autoclave and growing crystals at constant pressure and temperature. This technique yields crystals of very good uniformity and optical quality. However, the process is more complicated and takes longer time, thereby increasing the price and limiting the availability of such crystals. Moreover, due to the equipment restrictions related to the high temperatures and pressures required, the size of the grown crystals is limited.

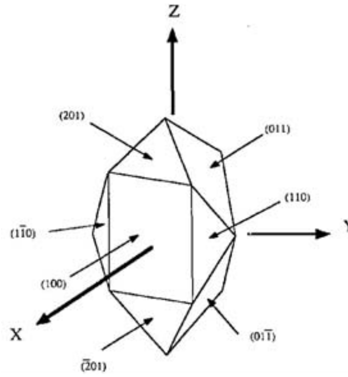

Fig. 2.2-4: Schematic view of the KTP crystal morphology. [4]

The KTP crystal morphology is similar for both flux and hydrothermal growth processes, and specifics depend on seed size and orientation. Figure 2.2-4 shows the schematic view of the KTP crystal morphology.

2.3 Ferroelectric properties

Ferroelectric crystals such as $LiNbO_3$ and $KTiOPO_4$ are characterised by displaying two or more states of different polarisation in the absence of external electrical fields [10]. They are part of a larger group of crystals, the pyroelectrics, which all have a spontaneous polarisation (P_s) not necessarily reversibly invertible. Thus all ferroelectrics are pyroelectric, although the contrary is not true. Similarly pyroelectrics are all part of the PZ crystal group, which is characterised by generating an electric field when subject to a mechanical strain. Thus ferroelectrics, such as LN and KTP, are also pyroelectric and piezoelectric. Ferroelectricity exists only in non-centrosymmetric crystals. In general a ferroelectric crystal does not exhibit the same polarisation orientation throughout. Each region with uniform polarisation is called "domain" and the distribution of domains forms the domain structure of the crystal. The spontaneous polarisation of a ferroelectric material usually decreases when heated and, as described in section 2.2, at the Curie temperature the crystal phase becomes paraelectric.

The spontaneous polarization P_s of a ferroelectric crystal may be reversed by the application of a suitable external electric field by means of the so called "electric field poling" (EFP) process (see section 2.5). The minimum field required for EFP is called the "coercive field" E_c, which varies with material and temperature. The spontaneous polarisation P_s can be defined by the amount of charge Q required to reverse a single domain crystal of a certain area A:

$$Q = \int I_{pol} dt = 2AP_S \qquad (2.3\text{-}1)$$

where I_{pol} is the charge transfer current flowing in the external circuit during EFP. In case of KTP, the anisotropic structure of the crystal lattice results in a velocity much higher for domain walls in the *x-y* plane than for walls in planes parallel to the *z*-axis. This is a favourable feature since domain broadening is limited when fabricating periodically poled structures along the *z*-axis. Conversely, the isotropic structure of LN causes velocity of domain walls in *x-y* plane equivalent to that along the *z* axis. Table 2.3-1 shows the values of the basic parameters related to the ferroelectric properties of LN and KTP crystals.

	T_c (°C)	P_s (c/m^2)	E_c (kV/mm)
$LiNbO_3$	1210	0.71	21
$KTiOPO_4$	946	0.14	2

Table 2.3-1: Values of the basic parameters related to the ferroelectric properties of LN and KTP. [11-13]

Built-in internal fields have been reported in ferroelectric crystals such as $LiTaO_3$ [14]: the spontaneous polarization measured as function of the applied external field exhibits an hysteresis loop. The presence of the so called “internal field” (IF) E_{int} is indicated by the large asymmetry in the loop. The magnitude of the IF can be determined empirically as $E_{int}=(E_{f1}-E_{r1})/2$ where E_{f1} and E_{r1} are the electric fields required for first forward and reverse poling, respectively.

2.4 Optical properties

LN is classified as a negative uniaxial crystal, having two different refractive indices for ordinary and extraordinary polarized light, n_o and n_e respectively, with $n_e<n_o$. Conversely KTP is a positive biaxial crystal with three different refractive index values n_x, n_y and n_z. Table 2.4-1 shows the refractive index values of congruent LN and flux-grown KTP crystals measured at room temperature for 632.8 nm. The index of refraction is also temperature dependent due to the thermo-optic effect. In case of LN the temperature dependant Sellmeier equations allow more accurate calculation of the refractive index [15]. In case of KTP the temperature derivative can be approximated by a Laurent series [16].

$LiNbO_3$ (negative uniaxial)	n_o=2.29 n_e=2.20
$KTiOPO_4$ (positive biaxial)	n_x=1.76 n_y=1.77 n_z=1.86

Table 2.4-1: Refractive index values of congruent LN [15] and flux-grown KTP [17] measured at room temperature for 632.8 nm.

LN is transparent to wavelengths from around 400 nm to about 5.5 μm [18] while the transparency range of KTP is from 350 nm to 4.5 μm. Figure 2.4-1 shows the absorption spectrum measured for congruent LN and flux-grown KTP.

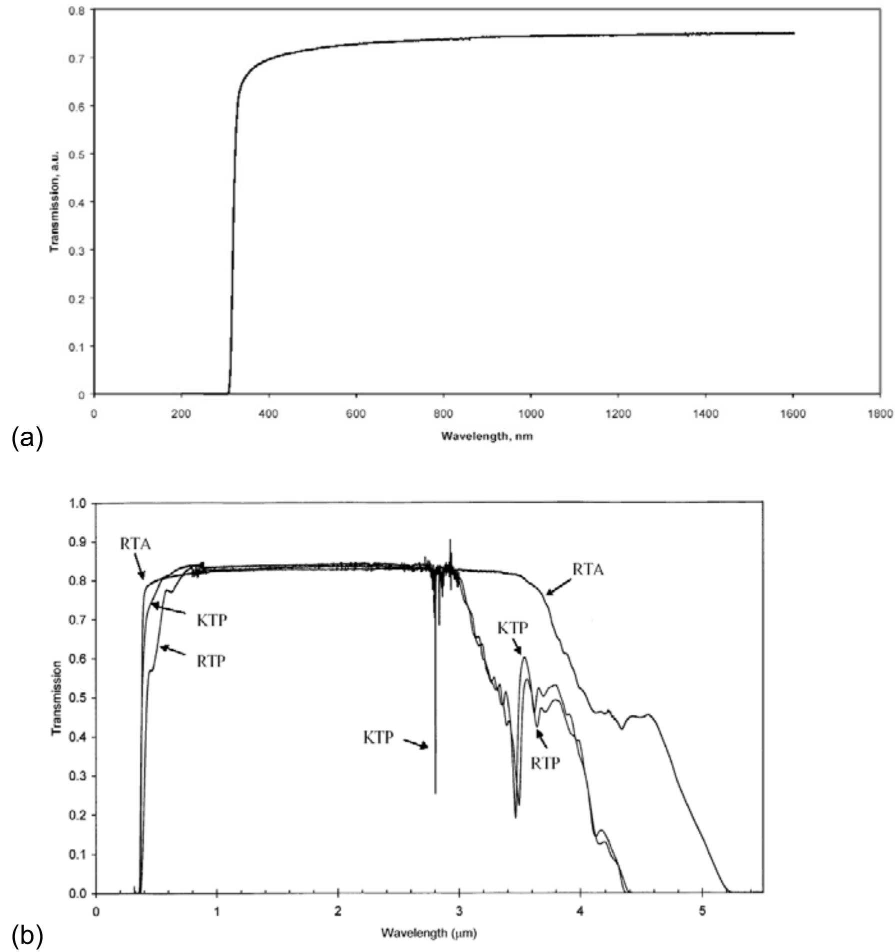

Fig. 2.4-1: Typical transmission spectrum of (a) congruent LN [19] and (b) flux-grown KTP [13], where the transmission spectra of other crystals from the KTP family are also shown.

$LiNbO_3$ and $KTiOPO_4$ are EO crystals. The linear EO effect, also known as Pockels effect, is a linear change in the refractive index ellipsoid induced by an applied electric field. This change is produced by the first power of the field, in contrast with the quadratic or Kerr EO effect. The change in the refractive index ellipsoid is expressed as

$$\Delta\left(\frac{1}{n^2}\right)_{ij} = \sum_k r_{ijk} E_k \tag{2.4-1}$$

where E_k are the components of the electric field and r_{ijk} represents the EO tensor which nonzero independent elements are determined by the crystal symmetry of the material. For example, in case of LN, the extraordinary index change derived from (2.4-1), when the electric field is applied along the crystal symmetry axis (*z*-axis), is

$$\Delta n_e = -\frac{1}{2} n_e^3 r_{33} E_3 \tag{2.4-2}$$

The structure of the EO tensor for LN and KTP is given below:

$$r_{ij} = \begin{bmatrix} 0 & -r_{22} & r_{13} \\ 0 & r_{22} & r_{13} \\ 0 & 0 & r_{33} \\ 0 & r_{42} & 0 \\ r_{42} & 0 & 0 \\ -r_{22} & 0 & 0 \end{bmatrix} \quad r_{ij} = \begin{bmatrix} 0 & 0 & r_{13} \\ 0 & 0 & r_{23} \\ 0 & 0 & r_{33} \\ 0 & r_{42} & 0 \\ r_{51} & 0 & 0 \\ 0 & 0 & 0 \end{bmatrix} \tag{2.4-3}$$

[LN] [KTP]

The non vanishing EO tensor elements and their values for LN and KTP are listed in Table 2.4-2.

$LiNbO_3$	r_{13}=10 pm/V r_{22}=6.7 pm/V r_{33}=32.2 pm/V r_{42}=32.6 pm/V
$KTiOPO_4$	r_{13}=9.5 pm/V r_{23}=15.7 pm/V r_{33}=36.6 pm/V r_{42}=9.3 pm/V r_{51}=7.3 pm/V

Table 2.4-2: Electro-optic tensor elements values for LN [20,21] and KTP [4] at room temperature for static electric field and light of 632.8 nm.

LN and KTP are the most widely used nonlinear crystals. Considering that the material response to electric fields is in general not linear, the electric polarisation can be expanded in powers of the field in the form:

$$P_i = \sum_j \varepsilon_0 \chi_{ij} E_j + \sum_{jk} 2d_{ijk} E_j E_k + \sum_{jkl} 4\chi^{(3)}_{ijkl} E_j E_k E_l + ... \tag{2.4-4}$$

The first right term is the usual linear dependence. The second term corresponds to the second order or quadratic nonlinearity, and next is the third order dependence. Only non-centrosymmetric crystals, as is the case of LN and KTP, can possess a non-vanishing d_{ijk} tensor [22]. Usually in these materials the second order processes are much more important in magnitude than those of higher orders for the moderate electric field commonly present in the materials. The second order nonlinear susceptibility tensor structure for LN and KTP is given below:

[LN] $$d_{ijk} = \begin{bmatrix} 0 & 0 & 0 & 0 & d_{15} & -2d_{22} \\ -d_{22} & d_{22} & 0 & d_{15} & 0 & 0 \\ d_{31} & d_{31} & d_{33} & 0 & 0 & 0 \end{bmatrix}$$

$$[\text{KTP}] \quad d_{ijk} = \begin{bmatrix} 0 & 0 & 0 & 0 & d_{31} & 0 \\ 0 & 0 & 0 & d_{32} & 0 & 0 \\ d_{31} & d_{32} & d_{33} & 0 & 0 & 0 \end{bmatrix} \qquad (2.4\text{-}5)$$

The main non-vanishing d_{ijk} second order nonlinear tensor elements for LN [23,24] and KTP [25], measured at 532 nm, are presented in Table 2.4-3.

$LiNbO_3$	d_{15}=d_{31}=-4.35 pm/V d_{22}=2.10 pm/V d_{33}=-27.2 pm/V
$KTiOPO_4$	d_{31}=1.4 pm/V d_{32}=2.65 pm/V d_{33}=10.7 pm/V

Table 2.4-3: Second-order nonlinear tensor elements for LN and KTP crystals. [23-25]

A number of nonlinear optical effects are observed as a result of the second order interaction. For accounting of this effects it is common to use the following nonlinear polarization expression:

$$P_i^{\omega_3} = d_{ijk}^{\omega_3:\omega_1,\omega_2} E_j^{\omega_1} E_k^{\omega_2} \qquad (2.4\text{-}6)$$

When the two field components are of the same wave of frequency ω, the nonlinear polarization will have a frequency 2ω, giving rise to the generation of a second harmonic new wave (SHG). Two different optical fields of frequencies ω_1 and ω_2 can be added to generate the sum frequency wave with $\omega_3=\omega_1+\omega_2$. In parametric amplification two waves of frequencies ω_1 and ω_2 with $\omega_1 > \omega_2$ and $I_1 >> I_2$ give rise to a new wave of frequency $\omega_3=\omega_1-\omega_2$, and the amplification of the ω_2 wave. In optical parametric oscillation (OPO) a wave of frequency ω_1 is decomposed in frequencies ω_2 and ω_3 such that $\omega 1=\omega 2+\omega 3$, provided the resonance of the system for at least one of the created frequencies. In order to obtain a practical intensity of the resulting wave, a phase matching condition is required for the new wave to be growing efficiently along the material in a coherent way. Phase matching conditions can be obtained in anisotropic materials for those propagation directions and polarizations for which the speed of waves of different frequencies are equal. For example in case of LN the exact birefringent phase matching condition for SHG is [22]

$$n_e^{2\omega} = n_o^{\omega} \qquad (2.4\text{-}7)$$

This is a very restrictive condition that can be fulfilled only for certain frequencies, propagation directions and sample temperatures. By fortune there is another possibility, more easy to fulfil, to obtain efficient wave generation by the so called quasi phase matching (QPM) disposition [26]. This can be obtained in materials where a property has a spatial periodic change of the proper period. In LN and KTP crystals this can be easily obtained with periodic domain structures, as described in Section 2.5. QPM by a periodic material structure is a technique to maintain the relative phase between the interacting waves in the material. In fact this method

corrects the relative phase mismatch at regular intervals by means of a structural periodicity of the nonlinear medium. In case of LN and KTP crystals, periodically alternated domain structures have been produced by different methods. In SHG a fundamental wave of frequency ω_1 and wavelength λ produces a polarization wave of frequency $2\omega_1$ through the second order nonlinear susceptibility. This polarization wave is forced by the fundamental wave, and then it travels with the same velocity $v_1=c/n_1$. The polarization wave radiates at each point of the material a free second harmonic optical wave, which travels with a velocity $v_2=c/n_2$. Because of the normal dispersion of the material, in general is $n_2 > n_1$, so that the fundamental and the second harmonic waves travel at different phase velocities. The sign of the energy transfer from one wave to the other is determined by the relative phase between them. The continuous increment of relative phase difference leads to an alternation in the direction of the flow of power between the waves. This produces an alternating growth and decay of the power of the second harmonic wave, which in general never gets a practical intensity. Along a propagation distance over which the relative phase changes in π the power is transferred to the second harmonic wave, and in the next equal distance the phase changes to 2π and the power is transferred to the fundamental wave. This distance, known as the coherence length L_c, is given by

$$L_c = \frac{\lambda}{4(n_2 - n_1)} \tag{2.4-8}$$

Of course, when the refractive indices are equal for both waves, for example using the birefringence properties of the material, this coherence length becomes infinite.

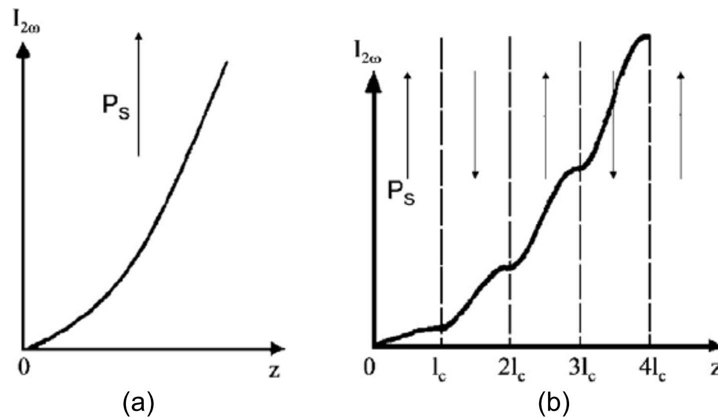

Fig. 2.4-2: Intensity of second harmonic generation as a function of the interaction length, (a) for exact birefringent phase matching, and (b) for quasi-phase matching in a periodically reversed LN sample with period $2L_c$.

In this situation of phase matching the electric field of the second harmonic wave grows linearly with the interaction length, and thus the intensity grows quadratically (see Fig.2.4-2).

Another possibility to obtain a final practical second harmonic wave is to produce a repeated inversion of the relative phase between the waves. One way to invert the phase of the generated wave is to change the sign of the nonlinear coefficient. This is done in LN and KTP by inversion of the direction of the ferroelectric domains. The highest efficiency of SHG in this situation is obtained when the inversion is done every coherence length, i.e. a change period of $2L_c$. This situation is illustrated in

Fig.2.4-2(b). Other longer periods can lead to a lower growth of the harmonic power. As it can be seen in Fig. 2.4-2, the second harmonic power grows more slowly using QPM than it does with birefringent phase matching. The greatest advantage of QPM lies in its ability to produce phase matching in situations which would otherwise be impossible, for example the use of nonlinear coefficients coupling waves of the same polarization. Non-linear coefficients of highest value can then be addressed. As the domain period can be changed, another advantage is the possibility to design a device operating at the desired wavelengths and temperature [26]. Additionally, the acceptance bandwidths can be significantly enhanced, leading to less critical phase matching. These structures can also be used to phase match other second order effects as parametric amplification or oscillation. Several methods have been developed to produce periodic domain structures in LN (PPLN) and KTP (PPKTP). The most widely used nowadays consists in the application of high external electric fields at room temperature to reverse the spontaneous polarization of the crystal, the so called electric field poling (EFP), as described in the next Section. This technique has produced PPLN [27-29] and PPKTP [30] for QPM SHG.

2.5 Periodic electric field poling

Starting from a single-domain crystal the production of periodic domain structures is achieved by application of electric fields at room temperature [27]. The challenge of fabricating high quality QPM structures by EFP lies in achieving few micrometers wide domains in crystals of several millimetres in thickness. This put high demands on the poling process. Most last years papers on PPLN structures obtained by EFP use commercial samples of 0.5 mm thickness, and interaction lengths of few centimetres are commonly reported. Thicker samples cannot be used because of the dielectric breakdown appearing before domain inversion. Recently it has been reported the decrease of the ferroelectric coercive field by one order of magnitude between congruent and stoichiometric crystals. This makes possible the electric field fabrication of periodic structures at room temperature in few millimetres thick samples [31].

The periodic EFP (PEFP) consists of using lithographic techniques to produce a photoresist grating of the desired period to be used as a mask for applying the electric field with a liquid electrolyte electrode [27]. A positive voltage pulse slightly exceeding the coercive field of the material (around 21 kV/mm in LN and 2 kV/mm in KTP) is applied on the patterned crystal face by using a liquid electrolyte. The liquid electrode configuration has two electrolyte containing chambers which squeeze the sample between two *O*-ring gaskets, as shown schematically in Fig. 2.5-1.

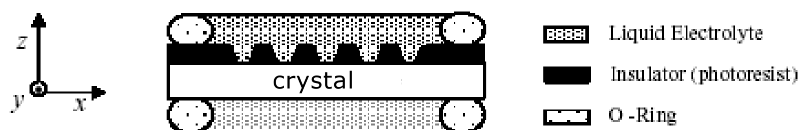

Fig. 2.5-1: Schematic view of the sample cross section after lithographic patterning.

Figure 2.5-2 illustrates the external electrical circuit. A conventional Signal Generator (SG) drives an High Voltage Amplifier (HVA - 2000x) with a series current limiting resistor R_s in order to get a 12*kV* positive voltage. A diode rectifier D is connected to the output of the HVA to prevent flowing of backswitch current in the circuit.

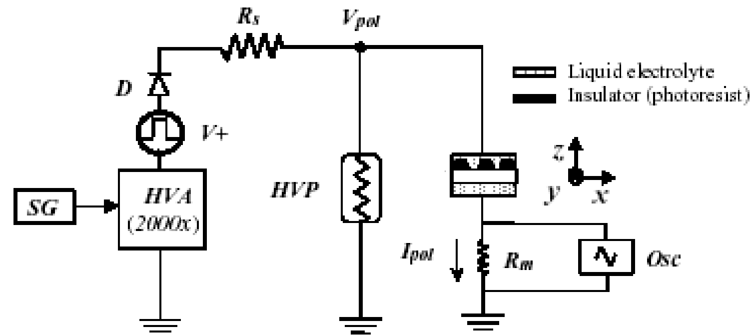

Fig. 2.5-2: Schematic view of the external circuit for EFP. *SG* signal generator; *HVA* high voltage amplifier; *D* diode rectifier; R_s series resistor; V_{pol} poling voltage; *HVP* high voltage probe; R_m monitoring resistor; *OSC* oscilloscope; I_{pol} poling current.

In case of LN the reversed domains typically grow beyond the width of the electrodes as result of the remaining fringing fields along the edges of the lithographic grating strips [27]. For example, in PPLN processed for infrared applications (periods >10 µm), the inverted domain width will typically be ~3-4 µm wider than that of the electrode. To obtain the desired domain size, insulating strips wider than the electrodes must be fabricated. The strategy for optimal domain patterning is to stop the voltage pulse before poling progresses under the photoresist layer. This is usually accomplished by delivering the *apriori* known amount of charge $Q=2P_sA$ required for polarization reversal in the electrode regions [32]. An *in-situ* stopping criterion consisting in watching for a drop in the poling current I_{pol} and a corresponding rise in the poling voltage V_{pol}, both effects indicating that the sample has completely poled under the electrodes and that the domains are now laterally spreading under the insulating layer, is used [27,32]. In fact, the conductivity of LN at room temperature is low enough that the poling current can be monitored readily by measuring the voltage drop across the R_m resistor (usually 10 kΩ) while a conventional High Voltage Probe (HVP) is used to measure the poling voltage V_{pol} across the sample. Both current and voltage waveforms are visualized on the oscilloscope *OSC* during the poling process.

In case of KTP crystals the high ionic conductivity is a key-factor that provides the main difficulty in achieving PEFP of materials from the KTP family. High ionic conductivity results in a large current flow through the crystal when the high voltage is applied. Such high ionic conductivity makes it difficult to control the domain reversal by monitoring the poling current through the crystal. An alternative method based on the transverse EO effect in the crystal has been developed, where the time-dependent changes in the polarisation-state of a He-Ne laser beam that propagates through the crystal during poling are monitored [33].

Reversed ferroelectric domain patterns are usually inspected unambiguously by a well established technique based on selective wet etching [34]. Different etching solutions are used for LN and KTP with the property to attack the *z*- polarity face while leaving *z*+ face untouched. In case of $LiNbO_3$ the etching solution consists of a $HF:HNO_3=1:2$ mixture, while in case of KTP the reversed domains are usually selectively etched by a $KOH:KNO_3=2:1$ mixture. Faster etching rates are obtained by acid bath at high temperature. Alternative approaches include the non-invasive domain visualization by crossed polarizers [35] and more recently the observation of domain structure by the EO effect [36].

2.6 Piezoelectric properties

$LiNbO_3$ and $KTiOPO_4$ are piezoelectric (PZ) crystals. The direct PZ effect consists in the formation of an electrical charge in proportion of an externally applied force. Conversely, according to the inverse PZ effect, an electric field E induces a deformation of the crystal, described by the strain S (shrinking or expanding). The mathematical relations are similar to those encountered in case of the EO effect (see section 2.4):

$$P_i = \sum_{jk} d_{ijk}\, \sigma_{jk} \quad \text{(for direct effect)} \qquad (2.6\text{-}1)$$

and

$$S_{jk} = \sum_{i} d_{ijk} E_i \quad \text{(for inverse effect)} \qquad (2.6\text{-}2)$$

where σ_{jk} are the components of the stress tensor, P_i are the components of the induced polarisation vector, d_{ijk} are the components of the PZ strain tensor, S_{jk} are the components of the induced strain tensor and E_i are the components of the applied electric field.

$LiNbO_3$	d_{15}= 69.2 10^{-12} C/N d_{22}= 20.8 10^{-12} C/N d_{31}= -0.85 10^{-12} C/N d_{33}= 6.0 10^{-12} C/N
$KTiOPO_4$	d_{31}= 1 pm/V d_{33}= 27 pm/V

Table 2.4-3: Piezoelectric strain tensor elements for LN [38] and KTP crystals [39].

PZ materials are mostly used for positioning applications in devices such as atomic force microscopes (AFMs) and translation stages, where they allow very precise positioning with a resolution of nanometers [37], surface acoustic wave devices, where they allow to transfer an electrical signal to a surface acoustic wave, and pressure sensors. The PZ strain tensor d_{ijk} of LN and KTP has the same symmetry as that of their nonlinear susceptibility tensor (see Eq.(2.4-5)) and their values are listed in Table 2.6-1.

References Chapter 2

[1] B.T. Matthias, J.P. Remeika, Phys. Rev. 76, 1886 (1949).

[2] A. Yariv, *Quantum electronics*, John Wiley& Sons (1989).

[3] L. Ouvrad, M. Troost, Compt. Rend. 121, 117 (1890).

[4] J.D. Bierlein, H. Vanherzeele, J. Opt. Soc. Am. B 6, 622 (1989).

[5] R.S. Weis, T.K. Gaylord, Appl. Phys. A 37, 191 (1985).

[6] K. Nassau, H.J. Levinstein, G.M. Loiacono, J. Phys. Chem. Solids 27, 983 (1966).

[7] H.M. O'Bryan, P.K. Gallagher, C.D. Brandle, J. Am. Ceram. Soc. 68, 493 (1985).

[8] S.C. Abrahams, P. Marsh, Acta Crystallogr. B 42, 61 (1986).

[9] M. Park, K.Kitamura, K. Terabe, Y. Furukawa, Y. Ji E. Suzuki, J. Crys. G. 180, 101 (1997).

[10] M.E. Lines, A.M. Glass, Clarendon Press Oxford (1977).

[11] K. Nassau, H.J. Levinstein, G.M. Loiacono, J. Phys. Chem. Solids 27, 989 (1966).

[12] I. Camlibel, J. Appl. Phys. 40, 1690 (1969).

[13] H. Karlsson, PhD thesis, Department of Laser Physics and Quantum Optics, The Royal Institute of Technology, Stockholm.

[14] V. Gopalan, M.C. Gupta, J. Appl. Phys. 80, 6099 (1996).

[15] D.S. Smith, H.D. Riccius, R.P. Edwin, Opt. Comm. 17, 332 (1976).

[16] W. Wiechmann, S. Kubota, T. Fukui, H. Masuda, Opt. Lett. 18, 1208 (1993).

[17] H.Y. Shen, Y.P. Zhou, W.X. Lin, Z.D. Zeng, R.R. Zeng, G.F. Yu, C.H. Huang, A.D. Jiang, S.Q. Jia, D.Z. Shen, IEEE J. 28, 48 (1992).

[18] G.D. Boyd, R.C. Miller, K. Nassau, W.L. Bond, A. Savage, Appl. Phys. Lett. 5, 234 (1964).

[19] K.K. Wong Ed., *Properties of lithium niobate* (2002).

[20] R. Nevado, C. Sada, F. Segato, F. Caccavale, A. Kling, J.C. Soares, E. Cantelar, F. Cussò, G. Lifante, Appl. Phys. B 73, 555 (2001).

[21] N. Hamelin, Y.T. Chow, J. Mod. Opt. 45, 2125 (1998).

[22] A. Yariv, P. Yeh, *Optical waves in crystals*, Wiley series in pure and applied optics (John Wiley and Sons, New York) (1984).

[23] R.C. Miller, W.A. Nordland, P.M. Bridenbaugh, J. Appl. Phys. 42, 4145 (1971).

[24] U. Ellenberger, R. Weber, J.E. Balmer, B. Zysset, D. Ellgehausen, G.D. Mizell, Appl. Opt. 31, 7563 (1992).

[25] B. Boulanger J.P. Feve, G. Marnier, B. Menaert, X. Cabirol, P Villeval, C. Bonnin, J. Opt. Soc. Am. B 11, 750 (1994).

[26] M.M. Fejer, G. A. Magel, D. H. Jundt, and R. L. Byer, IEEE J. Quantum Electron. 28, 2631 (1992).

[27] M. Yamada, N. Nada, M. Saitoh, K. Watanabe, Appl. Phys. Lett. 62, 435 (1993).

[28] W.K. Burns, W. McElhanon, L. Goldberg, IEEE Photon. Technol. Lett. 6, 252 (1994).

[29] J. Webjörn, V. Pruneri, P.St.J. Russell, J.R.M. Barr, D.C. Hanna, Electron. Lett. 30, 894 (1994).

[30] Q. Chen, W.P. Risk, Electron. Lett. 30, 1516 (1994).

[31] V. Bermùdez, L. Huang, D. Hui, S. Field, E. Dieguez, Appl. Phys. A 70, 591 (2000).

[32] L.E. Myers, R.C. Eckardt, M.M. Fejer, R.L. Byer, W.R. Bosenberg, J.W. Pierce, J. Opt. Soc. Am. B 12, 2102 (1995).

[33] H. Karlsson, F. Laurell, L.K. Cheng, Appl. Phys. Lett. 74, 1519 (1999).

[34] K. Nassau, H.J. Levinstein, Appl. Phys. Lett. 7, 69 (1965).

[35] V. Pruneri, J. Webjörn, P.St.J. Russell, J.R.M. Barrand, D.C. Hanna, Opt. Commun. 116, 159 (1995).

[36] V. Gopalan, Q.X. Jia, T.E. Mitchell, Appl. Phys. Lett. 75, 2482 (1999).

[37] J.P. Fillard, *Near field optics and nanoscopy*, World Scientific (1996).

[38] R.T. Smith, F.S. Welsh, J. Appl. Phys. 42, 2219 (1971).

[39] H. Graasfma, G.W.J.C. Heunen, S. Dahaoui, A. El Haouzi, N.K. Hansen, G. Marnier, Acta Crystallogr. B 53, 565 (1997).

Chapter 3

Holography

3.1 Introduction

Dennis Gabor's paper [1] from 1948 stated the birth of holography that was successively recognized by the Nobel Prize. In his text he presented a method for wavefront reconstruction originally intended for microscopy. The new technique really started to grow only after the 1960s, largely thanks to the development of the coherent light sources known as the "laser". Many applications started to emerge since then. "Digital" holography (DH) is a very interesting technique for optical metrology and gained much interest during the late 1990s. This interest seems to grow continuously. The Section 3.2 provides a brief introduction to holography, by establishing the concepts of optical recording and reconstruction. Deep treatments exist in books by Hariharan [2], Smith [3] and Abramson [4], just to cite a few. Section 3.3 describes DH and its two main reconstruction methods. The resolution criterion is introduced in Section 3.4.

3.2 Holography in general

Holography is basically a two-step process. An item or object is illuminated by monochromatic, coherent light with a wavelength λ. The object scatters the incoming light and emits a complex wavefield *O(x',y')* that consists of an amplitude $|O|$ and a phase $\phi(x',y')$. [5]:

$$O(x',y') = |O(x',y')| e^{i\phi(x',y')} \qquad (3.2\text{-}1)$$

The purpose of the technique is to (1): capture the complete wavefront, both amplitude and phase (unlike photography where only the intensity pattern is of interest), and (2): be able to reconstruct this wavefront at a later time. The couple *(x',y')* denotes the cartesian coordinates in the plane where the wavefield is recorded.

3.2.1 Recording

Since all recording materials respond to intensity only, the phase has to be encoded in the intensity pattern impinging on the recording device. The solution is to add another wave mutually coherent with the object wavefield *O(x',y')*. Both waves hit the recording device and create an interference pattern described mathematically by

$$\begin{aligned} I &= |O(x',y') + r(x',y')| = (O(x',y') + r(x',y'))(O(x',y') + r(x',y'))^* \\ &= |O(x',y')|^2 + |r(x',y')|^2 + 2|O(x',y')||r(x',y')| \\ &\cos[\phi(x',y') - \phi_r(x',y')] \end{aligned} \qquad (3.2.1\text{-}1)$$

where * denotes complex conjugation, I is the intensity of the pattern, and *r(x',y')* is the second wave, called the "reference":

$$r(x',y') = |r(x',y')| e^{-i\phi_r(x',y')} \qquad (3.2.1\text{-}2)$$

Equation (3.2.1-1) clearly shows that the intensity depends on ϕ, thus the phase is encoded in the recorded interference pattern which is called “hologram”. Figure 3.2.1-1 shows the schematic view of a typical hologram recording.

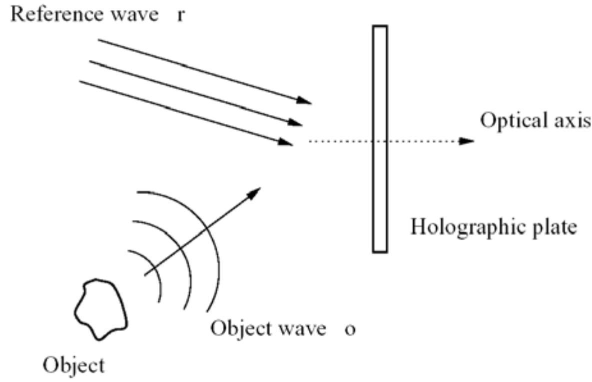

Fig. 3.2.1-1: Schematic view of a typical hologram recording. [3]

Many different set-ups and types of reference waves are feasible in this process, depending of what kind of hologram is required. The experiments which will be presented in this thesis basically use a set-up where the object beam is separated from the reference one by an angle θ as shown in Fig. 3.2.1-2. The configuration is called “off-axis” arrangement [6] when $\theta \neq 0$, whereas in case $\theta = 0$ the two wavefronts coincide and an “in-line” configuration is obtained. The reference is a normally impinging, uniform plane wave given by $r(x', y') = |r|$.

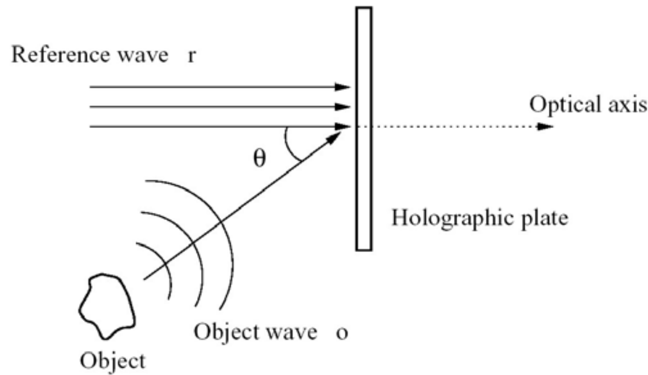

Fig. 3.2.1-2: Schematic view of the off-axis configuration and normally impinging, plane reference wave for hologram recording. [3]

The phase $\phi_r(x',y')$ in Eqs.(3.2.1-1) and (3.2.1-2) is then constant [2]. This kind of set-up is widely used in DH. The phase $\phi(x',y')$ can be split into a random term $\varphi(x',y')$ depending on the scattering surface, and a term $2\pi f_r x'$ caused by the offset angle:

$$\phi(x',y') = \varphi(x',y') + 2\pi f_r x' \qquad (3.2.1\text{-}3)$$

where $f_r = \sin\theta/\lambda$ can be considered a spatial carrier frequency and $\varphi(x',y')$ contains the information of interest. Equation (3.2.1-1) then becomes

$$I = |O(x',y')|^2 + |r|^2 + 2|O(x',y')||r|\cos[\varphi(x',y') + 2\pi f_r x'] \qquad (3.2.1\text{-}4)$$

An un-focused wavefront in the Fresnel region of diffraction [5] is recorded, thus the holograms are called "Fresnel" holograms [7]. Traditionally the recording medium has been a photographic film or plate with a silver halide emulsion, but other materials exist as well [5,8]. They have at least one feature in common: they are meant for optical reconstruction.

3.2.2 Optical reconstruction

The second step is the reconstruction of the object wavefront. The holographic plate is chemically developed and put in its original position while the object is removed. The plate can now be considered as a transparency with an amplitude transmittance $h(x',y')$ [5] given by

$$\begin{aligned} h(x',y') &= h_0 + \beta I = \\ & h_0 + \beta\left[|O(x',y')|^2 + |r|^2 + |r|O(x',y') + |r|O^*(x',y')\right] \end{aligned} \qquad (3.2.2\text{-}1)$$

The transmittance is usually referred to as t, but h is used here to emphasize that this is a holographic transmittance. The term h_0 is caused by the uniform reference wave while both h_0 and β are constant over the coordinates but depend on the exposure time and on the physical properties of the holographic plate. If the developed plate is illuminated only by the reference wave, the wavefield transmitted by the transparency is the following product

$$\begin{aligned} u(x',y') &= r(x',y')h(x',y') \\ &= |r|\left[h_0 + \beta|r|^2\right] + \beta|r||O|^2 + \beta|r|^2 O(x',y') + \beta|r|^2 O^*(x',y') \\ &= u_1(x',y') + u_2(x',y') + u_3(x',y') + u_4(x',y') \end{aligned} \qquad (3.2.2\text{-}2)$$

which consists of the four terms:

$$\begin{aligned} u_1(x',y') &= |r|\left[h_0 + \beta|r|^2\right] \\ u_2(x',y') &= \beta|r||O(x',y')|^2 \\ u_3(x',y') &= \beta|r|^2|O(x',y')|e^{i\varphi(x',y')}e^{i2\pi f_r x'} \\ u_4(x',y') &= \beta|r|^2|O(x',y')|e^{-i\varphi(x',y')}e^{-i2\pi f_r x'} \end{aligned} \qquad (3.2.2\text{-}3)$$

The schematic view of the optical reconstruction of the original wavefront is shown in Fig. 3.2.2-1. The first term, $u_1(x',y')$, is the attenuated reference wave transmitted directly through the hologram. The term $u_2(x',y')$ is a spatially varying "cloud" surrounding u_1 and with an angular spread given by the angular extent of the object. These two terms constitute the zeroth order of diffraction. The third term $u_3(x',y')$ is, except for a constant factor, an exact replica of the original wavefront. By looking

through the hologram, one can see a three dimensional image that is almost impossible to distinguish from the original object, with parallax and depth of focus. It is called a “virtual” image as opposed to the “real” or “conjugate” image produced by the fourth term $u_4(x',y')$.

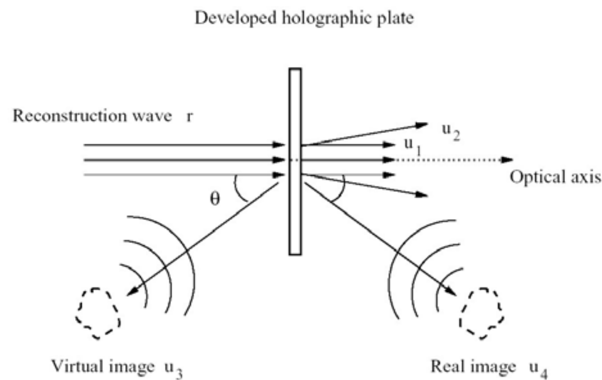

Fig. 3.2.2-1: Schematic view of the optical reconstruction of the original wavefront. [3]

The last mentioned image is another copy of the original object wave, but focused on the opposite side of the plate.

3.3 Digital Holography

In 1967 Goodman and Lawrence [9] demonstrated how a wavefront recorded by a vidicon detector could be numerically reconstructed by a computer. This was the first example of DH. The first step in the holographic process is performed optically, but the traditional recording medium is replaced by an electronical device such as a digital charge-coupled-device (CCD) [10] camera with the lens removed. The wavefront is digitized and stored as an array of zeros and ones in a computer. The second step (reconstruction) consists of a numerical simulation of wave propagation, thus obtaining holograms and reconstructing is fast and easy without any cumbersome chemical process. In addition, the method provides simple access to both amplitude and phase, as have been demonstrated for example in [11-13]. Recent advances in CCD and computer technology make recording by digital CCD cameras an alternative to “classical” holography in some cases. In 1967 a digital reconstruction took 5 minutes while today the same computation with a much larger array takes a couple of seconds. However, no electronic devices have been able to compete with the high resolution of the traditional holographic materials.

3.3.1 The CCD chip as a holographic recording device

The recording process is a sampling of an interference pattern consisting of spatial frequencies, the highest of which is given by the largest angle between object and reference wave. The limited resolution of the CCD chip and similar digital devices decides the maximum frequency allowed for sampling and severely restricts the experimental set-up configuration. According to the Whittaker-Shannon sampling theorem [5,14] each period must be recorded by at least two detector elements. If Λ is the fringe spacing and d_p the detector pitch (centre-to-centre spacing between neighbouring detector elements) in one transversal direction, then

$$2d_p \leq \Lambda \qquad (3.3.1\text{-}1)$$

A geometrical evaluation in which θ is the angle between the object and the reference wave gives

$$\Lambda = \frac{\lambda}{2\sin\left(\frac{\theta}{2}\right)} \qquad (3.3.1\text{-}2)$$

Combining Eqs.(3.3.1-1) and (3.3.1-2) gives

$$\theta \leq \arcsin\left(\frac{\lambda}{2d_p}\right) \qquad (3.3.1\text{-}3)$$

where $1/(2d_p)$ is the sampling frequency. This means that the angular extent of the object, θ_{max} in Fig. 3.3.1-1, must not exceed this limit. In order to use the entire available bandwidth of the recording device, the equal sign in Eq.(3.3.1-3) should be used. Another geometrical evaluation shows that if the distance d between the CCD and the object is

$$d \approx \frac{2d_p}{\lambda} D \qquad (3.3.1\text{-}4)$$

then the maximum bandwidth is obtained without violating the sampling theorem. D is the transversal size (height or width) of the object, and small angular values are assumed according to Eq.(3.3.1-3).

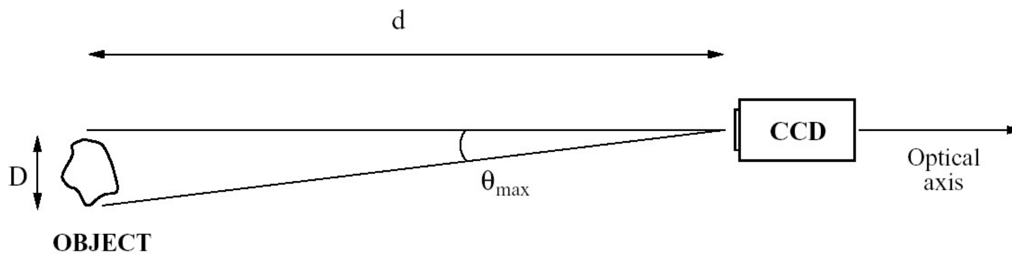

Fig. 3.3.1-1: Schematic view of the angular extent of the object: θ_{max} is the angular extent of the object and the maximum angle between object and reference wave; d is the distance along the optical axis between the CCD chip and the object; D is the transversal size of the object, normal to the optical axis. [3]

The distance d is in general quite large compared to the object size. For example, when the detector pitch is 6.7 µm and the illuminating light comes from a He-Ne laser (λ = 632.8 nm), the object must be less than 5 cm wide and placed 1 m in front of the CCD. Applications that have been demonstrated over the last years include microscopy [15,16], deformation studies [17], particle analysis [18], vibration analysis [19], characterization of micro-optics [20], shape measurements by multi-wavelength contouring [21] and light-in-flight observation [22]. Even larger objects have been used with the aid of lenses that demagnify the object wave [23], magnify the interference pattern [13] or image the object onto the CCD [24]. The latter produces image plane holograms, which is also utilized in electronic or digital speckle pattern

interferometry (ESPI/DSPI) [7]. In many cases the detector pitch d_p is equal to the size of each detector element, also called "unit cell size" or "pixel size". $\Delta x'$ and $\Delta y'$ denote the one-dimensional pixel sizes along the *x'* and *y'* directions, respectively.

3.3.2 Numerical reconstruction

While the recording step is basically an interference process, the reconstruction can be explained by diffraction theory. Figure 3.3.2-1 shows the geometry, in which the *z*-axis is the optical axis.

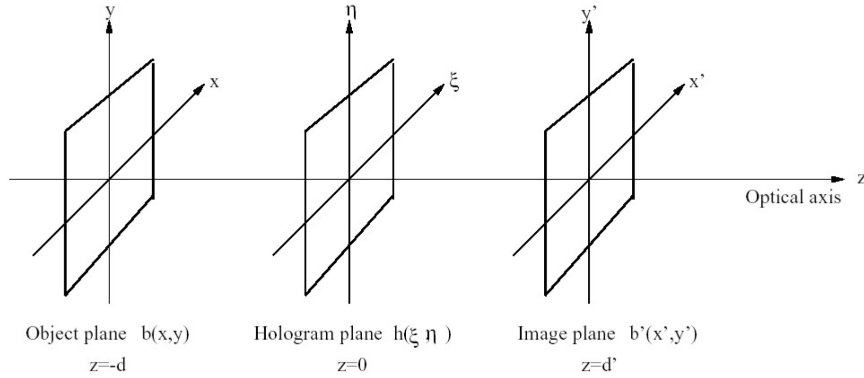

Fig. 3.3.2-1: Geometry for digital recording and numerical reconstruction.

The hologram is positioned in the (ξ,η) plane where z=0, while (x,y) is the object plane at $z=-d$ ($d > 0$) and (x',y') is an arbitrary plane of observation at $z = d'$. All these planes are normal to the optical axis. During reconstruction, the hologram is an amplitude transmittance or aperture that diffracts the reference wave and the propagation of the wavefield $u(\xi,\eta)=h(\xi,\eta)r(\xi,\eta)$ from the hologram plane to a plane of observation is numerically simulated. With Section 3.2.2 in mind, a focused image of the original object should be situated at $z=d$ and $z=-d$ provided the reference as a plane wave. A detailed derivation of the mathematical formulae of diffraction theory is given by Goodman [5]. If $b'(x',y')$ is the reconstructed wavefront in the plane of observation, then Rayleigh-Sommerfeld's diffraction integral found in [5] can be written as [25]:

$$b'(x',y') = \frac{1}{i\lambda}\iint h(\xi,\eta)r(\xi,\eta)\frac{e^{ik\rho}}{\rho}\cos\Omega d\xi d\eta \qquad (3.3.2\text{-}1)$$

where the integration is carried out over the hologram surface and

$$\rho = \sqrt{d'^2+(x'-\xi)^2+(y'-\eta)^2} \qquad (3.3.2\text{-}2)$$

is the distance from a given point in the hologram plane to a point of observation. The quantity $\cos\Omega$ is an *obliquity factor* [5] normally set to one because of small angles. If the reference is a collimated and normally impinging wavefront, as in this case, one can set $r(\xi,\eta)=|r|=1$, thus simplifying the numerical implementation. A disadvantage is that the plane reference does not exploit the maximum bandwidth of the CCD chip [26] as is the case with a spherical one. For the sake of generality, the notation

"$r(\xi,\eta)$" is kept throughout this chapter. Equation (3.3.2-1) represents a complex wavefield with intensity and phase distributions I and ψ given by

$$I(x',y') = b'(x',y')b'^*(x',y'); \quad \psi = \arctan\frac{\Im\{b'(x',y')\}}{\Re\{b'(x',y')\}} \qquad (3.3.2\text{-}3)$$

$\Im\{b'\}$ and $\Re\{b'\}$ denote the imaginary and real part of b', respectively. There are two ways [7] of implementing Eq.(3.3.2-1) in a computer: the Fresnel and convolution methods. Both approaches convert Rayleigh-Sommerfeld's diffraction integral into one or more *Fourier transforms* which make the numerical implementation easy. Several *Fast Fourier Transform* (FFT) algorithms are available for efficient computations.

3.3.3 Fresnel method

The Fresnel method is based on approximations of the expression in Eq.(3.3.2-2) by applying the binomial expansion [5] of the square root. When terms of higher order than the first two are excluded, ρ becomes:

$$\rho \approx d'\left[1 + \frac{1}{2}\frac{(x'-\xi)^2}{d'^2} + \frac{1}{2}\frac{(y'-\eta)^2}{d'^2}\right] \qquad (3.3.3\text{-}1)$$

For the ρ appearing in the exponent, neglecting higher order terms, represents very small phase errors. A sufficient condition [5] is that the distance d' is large enough:

$$d'^3 \gg \frac{\pi}{4\lambda}\left[(x'-\xi)^2 + (y'-\eta)^2\right]^2_{\max} \qquad (3.3.3\text{-}2)$$

Since this is an overly stringent condition, even shorter distances produce accurate results. The exponent being the most critical factor, dropping all terms but the first in the *denominator* produces acceptable errors only. Thus, the propagation integral in Eq.(3.3.2-1) becomes

$$b'(x',y') = \frac{1}{i\lambda d'}\iint h(\xi,\eta)r(\xi,\eta)e^{ikd'\left[1+\frac{1}{2}\frac{(x'-\xi)^2}{d'^2}+\frac{1}{2}\frac{(y'-\eta)^2}{d'^2}\right]}d\xi d\eta \qquad (3.3.3\text{-}3)$$

which represents a *parabolic* approximation to spherical waves. Rewriting this integral yields the reconstructed wavefield as a Fourier transform of the product of the hologram, the reference and a chirp function $\exp\left\{\frac{i\pi}{d'\lambda}\left(\xi^2+\eta^2\right)\right\}$:

$$b'(x',y') = \frac{1}{i\lambda d'}e^{ikd'}e^{i\pi d'\lambda\left(\nu^2+\mu^2\right)}\times$$
$$\times\iint h(\xi,\eta)r(\xi,\eta)e^{\frac{i\pi}{d'\lambda}\left[\xi^2+\eta^2\right]}e^{-2\pi i[\xi\nu+\eta\mu]}d\xi d\eta$$

$$= \frac{1}{i\lambda d'} e^{ikd'} e^{i\pi d'\lambda\left(\nu^2+\mu^2\right)} F\left\{ h(\xi,\eta) r(\xi,\eta) e^{\frac{i\pi}{d'\lambda}\left[\xi^2+\eta^2\right]} \right\} \tag{3.3.3-4}$$

where $\nu = \frac{x'}{d'\lambda}$, $\mu = \frac{y'}{d'\lambda}$ and F{….} denotes the Fourier transform. The transform is multiplied by a spatially constant intensity factor $1/(i\lambda d')$ and a phase factor $\exp(ikd')$ $\exp(i\pi d'\lambda(\nu^2 + \mu^2))$ not dependent on the hologram.

The acquired hologram is a discrete set of numbers $h(k\Delta\xi, l\Delta\eta)$ taken on a rectangular ($N\times M$) matrix with steps $\Delta\xi$ and $\Delta\eta$ along the coordinates. Therefore, a numerical implementation of Eq.(3.3.3-4) must be the equivalent two-dimensional discrete Fourier transform [7]:

$$\begin{aligned} b'(n,m) &= e^{-\frac{i\pi d'\lambda}{NM}\left(\frac{n^2}{\Delta\xi^2}+\frac{m^2}{\Delta\eta^2}\right)} \times \\ &\times \sum_{k=0}^{N-1}\sum_{l=0}^{M-1} h(k\Delta\xi, l\Delta\eta) r(k\Delta\xi, l\Delta\eta) e^{\frac{i\pi}{d'\lambda}\left(k^2\Delta\xi^2+l^2\Delta\eta^2\right)} e^{2i\pi\left[\frac{kn}{N}+\frac{lm}{N}\right]} \\ &= e^{-\frac{i\pi d'\lambda}{NM}\left(\frac{n^2}{\Delta\xi^2}+\frac{m^2}{\Delta\eta^2}\right)} DF\left\{ h(k,l) r(k,l) e^{\frac{i\pi}{d'\lambda}\left(k^2\Delta\xi^2+l^2\Delta\eta^2\right)} \right\} \end{aligned} \tag{3.3.3-5}$$

omitting the constant factor $\exp(ikd')/(i\lambda d')$ for clarity. *DF {...}* denotes a discrete Fourier transform. The reconstructed image is a ($N\times M$) matrix with elements (n,m) and steps

$$\Delta x'_F = \frac{d'\lambda}{N\Delta\xi}; \quad \Delta y'_F = \frac{d'\lambda}{M\Delta\eta} \tag{3.3.3-6}$$

along the transversal directions.

3.3.4 Convolution method

The second method regards Eq.(3.3.2-1) as a 'convolution' integral:

$$\begin{aligned} b'(x',y') &= \iint h(\xi,\eta) r(\xi,\eta) g(x'-\xi, y'-\eta) d\xi d\eta = \\ &= \left[h(x',y') r(x',y')\right] * g(x',y') \end{aligned} \tag{3.3.4-1}$$

where the product *hr* is convolved with the impulse response [7]

$$g(x'-\xi, y'-\eta) = \frac{1}{i\lambda}\frac{e^{ik\rho}}{\rho}\cos\Theta \approx \frac{1}{i\lambda}\frac{e^{ik\sqrt{d'^2+(x'-\xi)^2+(y'-\eta)^2}}}{\sqrt{d'^2+(x'-\xi)^2+(y'-\eta)^2}} \tag{3.3.4-2}$$

where $*$ denotes the convolution operation in Eq.(3.3.4-1), *b'* describes here a linear, space-invariant system of spherical waves propagating in free space from the hologram to the image plane. A point source at $z = 0$ is the origin of its image given by $g(x', y')$ at $z = d'$. The 'convolution theorem' [5] states that the convolution of *hr* with *g* is the product of the individual transforms $F\{h \cdot r\}$ and $F\{g\}$. Thus, the wavefield can be found as the inverse transform

$$b'(x', y') = F^{-1}\{F\{h(\xi,\eta)r(\xi,\eta)\}F\{g(\xi,\eta)\}\} \qquad (3.3.4\text{-}3)$$

Similar to the Fresnel method, the discrete version of the reconstruction formula must be implemented. An analytical version of $F\{g\}$ is readily available, saving one Fourier transform in Eq.(3.3.4-3). Its discrete version is given by [7]

$$G = F\{g\} = \exp\left\{\frac{2\pi i d'}{\lambda}\sqrt{1 - \frac{\lambda^2\left(n + \frac{N^2\Delta\xi^2}{2d'\lambda}\right)}{N^2\Delta\xi^2} - \frac{\lambda^2\left(m + \frac{M^2\Delta\eta^2}{2d'\lambda}\right)}{M^2\Delta\eta^2}}\right\} \qquad (3.3.4\text{-}4)$$

The final reconstruction formula is

$$b'(n,m) = DF^{-1}\{DF\{h(k,l)r(k,l)\}G\} \qquad (3.3.4\text{-}5)$$

and in the resulting image the pixel sizes are

$$\Delta x'_C = \Delta\xi\,; \quad \Delta y'_C = \Delta\eta \qquad (3.3.4\text{-}6)$$

3.3.5 Comparison between Fresnel and convolution method

When comparing the two reconstruction methods, different pixel sizes arise in the observation plane because of the different number of Fourier transforms involved. A comparison of Eqs.(3.3.3-6) and (3.3.4-6) shows that $\Delta x'_C$ is smaller than $\Delta x'_F$ if $d' > (N\Delta\xi^2)/\lambda$ (and similar for the *y'* direction). When inserting typical values (N=1024; $\Delta\xi$=6.7 µm; λ=632.8 nm; d'=1 m) in the equation

$$\Delta x'_C = \frac{N\Delta\xi^2}{\lambda d'}\Delta x'_F \qquad (3.3.4\text{-}7)$$

which relates the two pixel sizes, $\Delta x'_F$ is about 14 times larger than $\Delta x'_C$. Since the latter is the pixel size in the hologram plane, only a $(N\Delta\xi \times M\Delta\eta)$ fraction of the whole

image is displayed when using the convolution approach. More information than in case of one single reconstruction is available, as shown in Fig. 3.3.5-1.

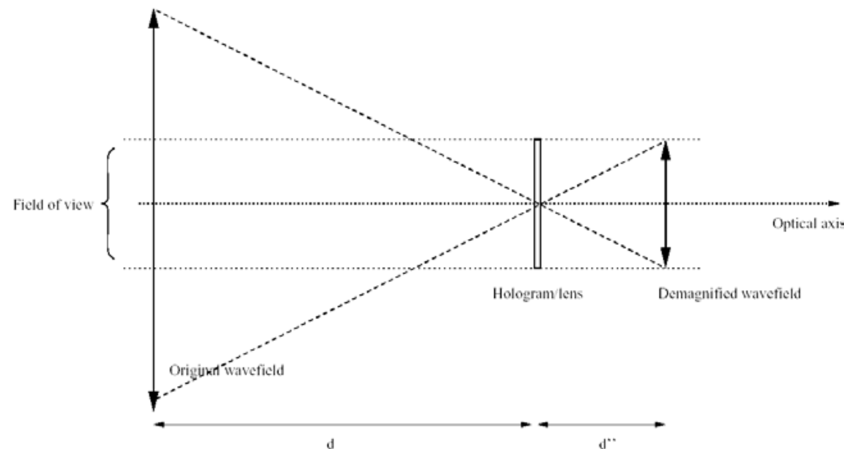

Fig. 3.3.5-1: The convolution method displays only a *(NΔξ×MΔη)* fraction of the whole wavefield. The numerical lens demagnifies the field to fit inside this rectangular window. [3]

Somehow the image has to fit the size of the hologram inside the small rectangle, either by expanding the hologram or by altering the reconstructed wavefield. The former method, namely increasing the rectangular window by padding the hologram with zeros (as described in [7,25]), is not an efficient method, at least not when the whole wavefield is of interest. If the matrix should contain 14 times more elements in each direction, a computation would take too long with today's technology. Demand for storage space would be very large. Another approach is to introduce a shift in the impulse response (2.23) and reconstruct different sections of the wavefield. This method is mentioned in [7].

3.4 Whole optical wavefield reconstruction by Digital Holography

In this section the numerical results obtained through the DH method for reconstructed amplitude distribution of the object wavefield using two recorded holograms digitised with two different set-up conditions is presented. The FFT digital reconstruction of the amplitude is carried out at different locations *z=d'* of the image plane along the *z*-axis propagation direction. A Mach-Zehnder (MZ) interferometer (see Fig. 3.4-1) is used for the observation of in-line hologram patterns.

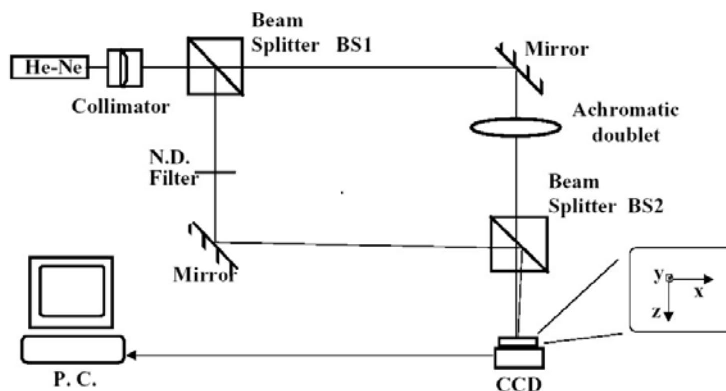

Fig. 3.4-1: Experimental set-up of the Mach-Zehnder interferometer for digital in-line holography.

A collimated He-Ne laser beam (wavelength λ=632.8 nm) is divided by the beam splitter *BS1* into two beams: one of these, the object beam, is a spherical wave produced by an achromatic doublet of focal length 300 mm; the other one is a reference plane wave, interfering with the object beam at the recombining beam splitter *BS2*. The hologram pattern is digitised by a CCD camera with pixel size $\Delta\xi=\Delta\eta$=11 μm and recorded under two different conditions corresponding to two frame buffer settings. The hologram pattern shown in Fig. 3.4-2(a) is recorded with the right setting of the frame buffer corresponding to 736 columns × 572 row. The image is a digitised array of (N×N)=(512×512) 8-bit encoded numbers. In Fig. 3.4-2(b) the frame buffer setting was intentionally modified to 768 columns × 572 row in order to introduce a slight anamorphism, which changes the aspect ratio of the image [27] from the value 1. In Fig. 3.4-2(b) the hologram is affected by an anamorphism which generates a deformation along the *x* horizontal direction, resulting in the formation of elliptically shaped interference fringes instead of the circular ones in Fig. 3.4-2(a). The DH reconstruction of the amplitude distribution is carried out in case of the first recording condition by using the discrete finite form of Eq.(3.3.3-4) with $r(\xi,\eta)=1$ and reconstruction distance *d’* ranging from 170 mm to 200 mm, at discrete steps of Δz=1 mm.

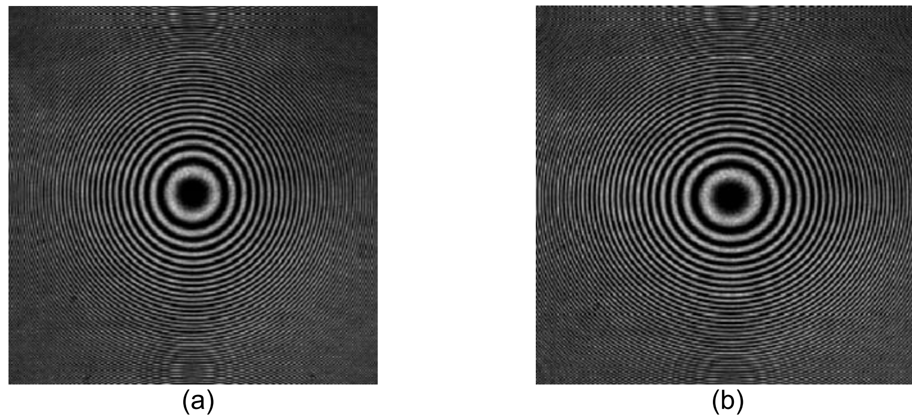

(a) (b)

Fig. 3.4-2: Hologram recorded under two different conditions corresponding to two settings of the CCD frame buffer: (a) (736 x 572); (b) (768 x 572).

In case of the aberrated hologram in Fig. 3.4-2(b) the amplitude distribution is determined for *d’* ranging from 181 mm to 218 mm at Δz=1 mm. The sequence of amplitude distributions are collected into movies (see Paper I). The reconstructed wavefield in the hologram plane contains three terms, which generate the zero order diffraction, the real and the virtual image of the object, here represented by the focal point of the object wavefield. The reconstructed intensities clearly show the patterns of these three terms appearing superimposed due to the in-line geometry of the set-up. The clip video corresponding to Fig. 3.4.1-2(c) (see Paper I) shows that a point shaped amplitude pattern is obtained at the reconstruction distance *d’=D*=180 mm from the hologram plane. According to simple geometrical considerations (see Fig. 3.4-3), this distance corresponds to the focusing distance of a converging spherical wavefield produced by the achromatic doublet.

The movie corresponding to Fig. 3.4.1-2(d) (see Paper I) shows the focusing of a wavefield affected by anamorphism. Two different focusing images are clearly visible: a line image at the horizontal focal line, occurring at *d’* 183 mm and corresponding to the tangential focus; a vertical line image at the sagittal focus reconstructed at a

distance *d'* 218 mm. This simple example shows that numerical reconstruction of holograms provides an efficient method for visualizing qualitatively the influence of wavefield aberrations and makes it possible, in principle, to compensate for phase distortions suffered by the wave front along its propagation.

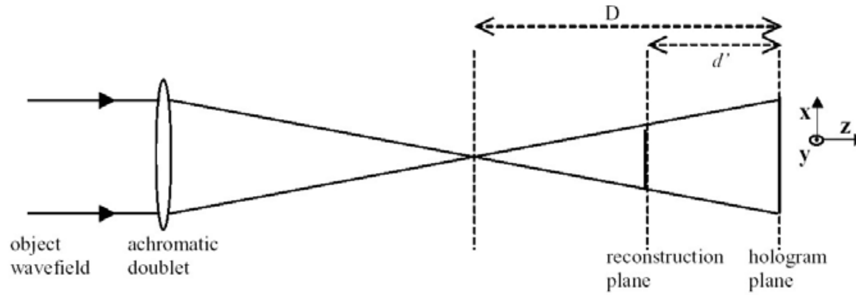

Fig.3.4-3: Recording geometry in digital holographic reconstruction of the object wavefield (the focal point of the spherical wave).

Quantitative analysis of optical aberrations of wavefields relies on the ability of DH to provide information not only about the amplitude but also on the phase distribution of the optical field at different planes from the recorded hologram.

3.4.1 Amplitude and phase distributions from simulated holograms

The intensity distribution of the acquired hologram can be represented by the following formula:

$$I(\xi,\eta) = 1 + \cos\left[\frac{\pi}{\lambda}\left(\frac{\xi^2}{z_x} + \frac{\eta^2}{z_y}\right)\right] \qquad (3.4.1\text{-}1)$$

which describes elliptical interference fringes like those shown in Fig. 3.4-2(b). The two distances z_x and z_y correspond to the vertical and horizontal focal lines, respectively. In case of the circular fringes in Fig. 3.4-2(a) z_x=z_y=z. The floating-point numbers computed by Eq.(3.4.1-1), provide a reasonable approximation of the integer-number distribution that occurs from the frame store. Figure 3.4.1-1(a),(b) show the intensity distributions in case of the circular and elliptical holograms, respectively, computed for z=250 mm in the circular case and z_x=300 mm; z_y=250 mm in the elliptical one.

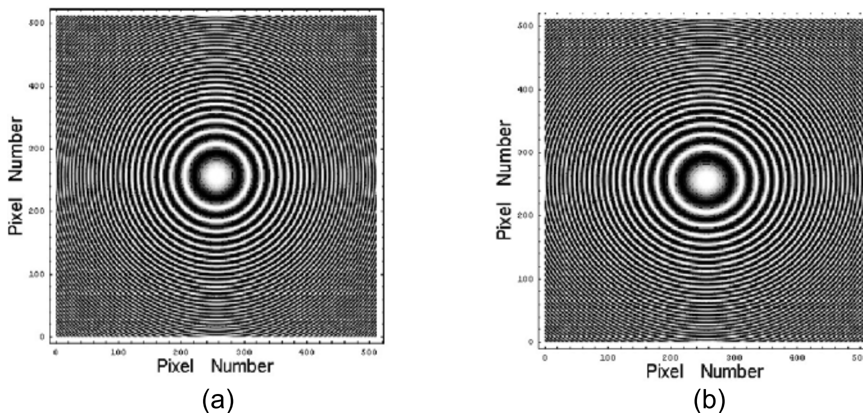

Fig. 3.4.1-1: Simulated intensity distribution in case of (a) the circular fringe pattern and (b) the elliptical one, computed by Eq.(3.4.1-1).

The test hologram patterns are digitised as an array (512×512)=($N\times N$); λ=632.8 nm and step size 11 μm along the x and y directions are assumed. Equation (3.4.1-1) can be written in the following form

$$I(\xi,\eta) = 1 + \frac{1}{2}\exp\left[\frac{i\pi}{\lambda}\left(\frac{\xi^2}{z_x} + \frac{\eta^2}{z_y}\right)\right] + \frac{1}{2}\exp\left[-\frac{i\pi}{\lambda}\left(\frac{\xi^2}{z_x} + \frac{\eta^2}{z_y}\right)\right] \qquad (3.4.1\text{-}2a)$$

The first term in Eq.(3.4.1-2a) produces the zero order of diffraction in the reconstructed image, while the other two terms generate the reconstruction of the object beam and that of the conjugate beam. This decomposition is more general than the specific example treated here. In fact, it is well known that in classical holography these two terms correspond to the reconstruction of the virtual and real image of the object (see Section 3.2.2). In order to reconstruct the complex amplitude of the object beam, one of these two terms has to be isolated, say

$$h(\xi,\eta) = \frac{1}{2}\exp[+i\psi(\xi,\eta)] \qquad (3.4.1\text{-}2b)$$

for which the phase distribution at the hologram plane is given by

$$\psi(\xi,\eta) = \frac{\pi}{\lambda}\left(\frac{\xi^2}{z_x} + \frac{\eta^2}{z_y}\right) \qquad (3.4.1\text{-}2c)$$

After extracting the object beam $h(\xi,\eta)$, a reconstruction procedure is used to determine the wavefield complex amplitude. The extraction of the above terms can be carried out by applying for example the four-quadrature-phase shifting reconstruction algorithm as described in case of in-line DH [28] and in [29] for the contrast enhancement of off-axis Fresnel holograms. Numerical simulations are presented here to investigate the reliability of DH for whole object wavefield reconstruction starting from the complex amplitude $h(\xi,\eta)$ recorded at the hologram plane. The digital reconstruction of the amplitude distributions for the two cases is shown in Fig. 3.4.1-2.

Note that in Fig. 3.4.1-2(b), the astigmatism of the wavefield results in a bright rectangular component, whereas in case of the spherical wavefield (Fig. 3.4.1-2(a)) a square image is obtained at the same distance d' = 180 mm. The images in Fig. 3.4.1-2(c),(d), obtained at d'=250 mm, clearly show that this distance corresponds to the focal plane of the spherical wave, which in fact appears focusing at a point image (Fig. 3.4.1-2(c)), and to the tangential focal plane in case of the astigmatic wavefield, which focuses at a line image (Fig. 3.4.1-2(d)). These simulation results reproduce quite well those obtained experimentally and shown into the movies corresponding to Fig. 3.4-2(a),(b). Figure 3.4.1-3 shows the phase distributions of the simulated spherical and astigmatic holograms reconstructed at d'=180 mm and wrapped in the interval $[\pi,\pi]$. Both phase distributions are computed in the restricted range of (140×140) pixel^2. Unwrapped phase values are calculated by using a well known unwrapping procedure [30] and Fig. 3.4.1-4 shows the three-dimensional image of the resulting unwrapped phase distributions.

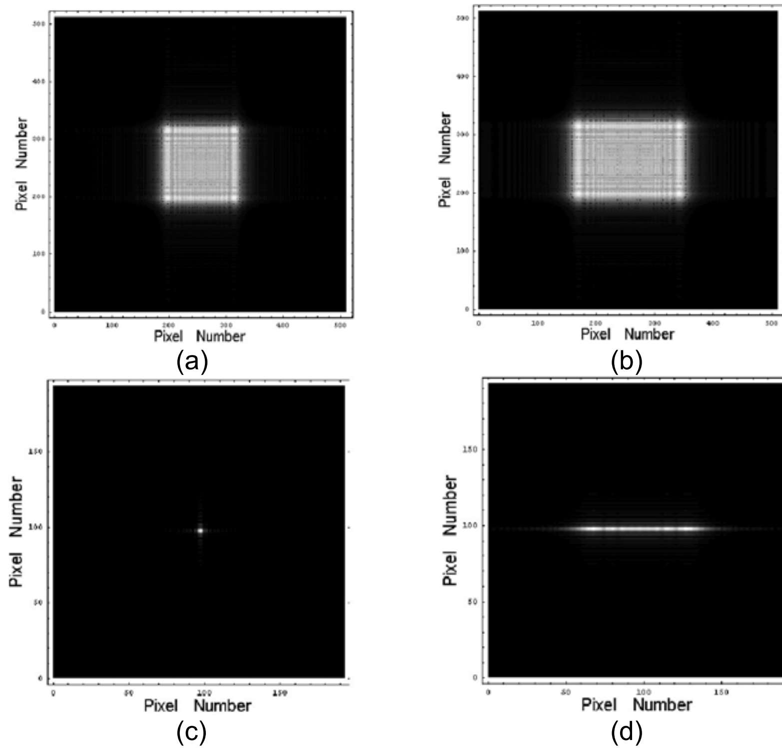

Fig. 3.4.1-2: Amplitude distribution reconstructed for the simulated holograms in Fig. 3.4.1-1 in case of (a) the spherical wave at *d'*=180 mm; (b) the astigmatic hologram at *d'*=180 mm; (c) the spherical wave at the focal plane *z*= 250 mm; (d) the astigmatic fringe pattern at the tangential focal plane at *z*= 250 mm.

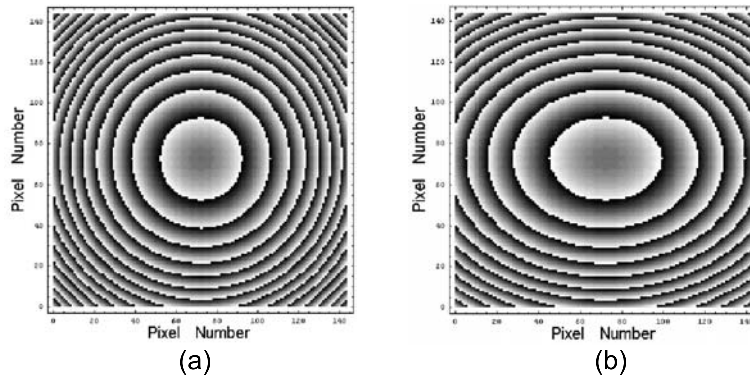

Fig. 3.4.1-3: Wrapped phase distributions computed by the convolution-based reconstruction method at distance *d'*=180 mm in case of (a) the simulated spherical wave front and (b) the simulated astigmatic wave front.

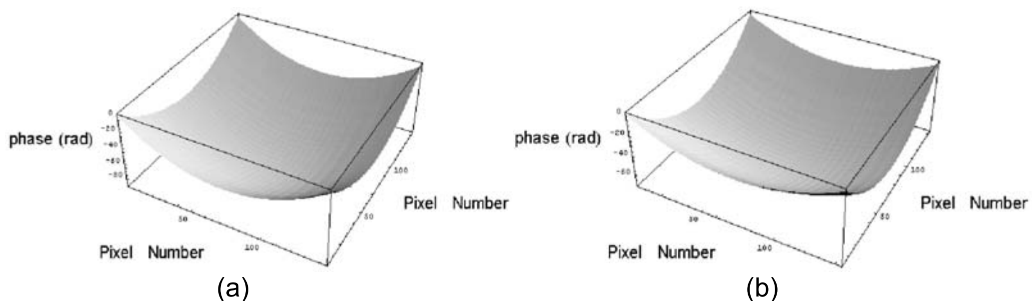

Fig. 3.4.1-4: Three-dimensional image of the unwrapped phase distributions reconstructed in case of (a) the simulated spherical wave and (b) the simulated astigmatic wave.

In order to compare the phase distributions reconstructed at different planes, Fig. 3.4.1-5 shows the unwrapped phase values along the *x*-horizontal (straight line) and *y*-vertical (dashed line) for the two waves and for different reconstruction distances. In Fig. 3.4.1-5(a) the two distributions are perfectly superimposed owing to the spherical symmetry of the wave front, whereas in Fig. 3.4.1-5(b) they are clearly different due to the astigmatism. The vertical axis in Fig. 3.4.1-5 represents the *z* propagation axis along which the various phase distributions are evaluated at distances ranging from *d'*=160 mm to *d'*=220 mm at step size of 10 mm. The scale of the horizontal axis in Fig. 3.4.1-5 is determined by the pixel size of the reconstructed image, which does not change in the convolution reconstruction method (see Ssection 3.3.4).

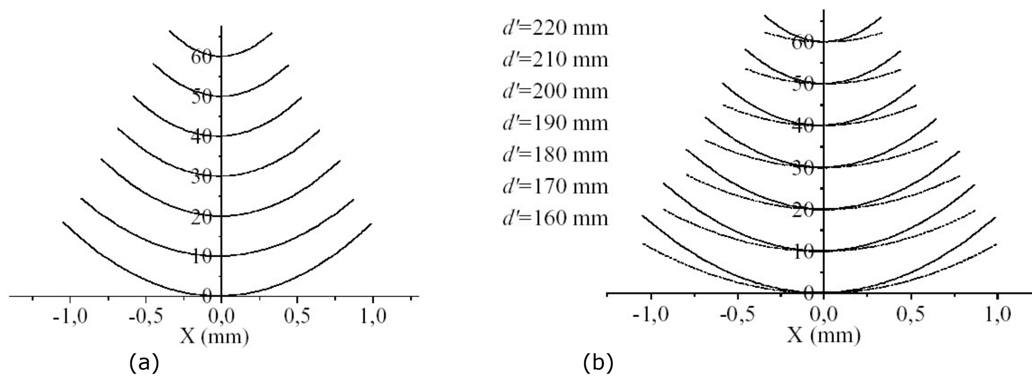

Fig. 3.4.1-5: One dimensional representation of the unwrapped phase values along the *x*-horizontal (straight line) and *y*-vertical (dashed line) directions for *d'* ranging from 160 mm to 220 mm, step size of 10 mm in case of (a) the simulated spherical wave front; (b) the simulated astigmatic wave front. The scale of the horizontal axis is determined by the pixel size *x*'=ξ of the reconstructed image which does not change in the convolution method. The vertical axis corresponds to the *z* propagation direction.

These plots give information about the wave front phase values at distances closer to the focus plane in the case of the spherical wave front as well as in case of the astigmatic one. Determination of the amplitude and phase at different planes along the propagation direction of the wave front demonstrates the capability of the DH for whole optical wavefield reconstruction allowing both qualitative and quantitative analysis of possible wavefield aberrations.

References Chapter 3

[1] D. Gabor, Nature 161, 77 (1948).

[2] P. Hariharan, *Optical Metrology: Principles, Techniques and Applications,* Cambridge Studies in Modern Optics vol.2, Cambridge University Press (1984).

[3] H.M. Smith, *Principles of Holography*, John Wiley & Sons, 2nd Ed. (1975).

[4] N. Abramson, *The making and Evaluation of Holograms*, Academic Press (1981).

[5] J.W. Goodman, *Introduction to Fourier Optics*, McGraw-Hill Companies Inc., 2nd Ed. (1996).

[6] E.N. Leith, J. Upatnieks, J. Opt. Soc. Am. 52, 1123 (1962).

[7] T.M. Kreis, M. Adams, W. Jüptner, Proc. SPIE 3098, 224 (1997).

[8] H.M. Smith Ed. *Holographic Recording Materials*, Top. in Appl. Phys. 20, Springer Verlag (1977).

[9] J.W. Goodman, R.W. Lawrence, Appl. Phys. Lett. 11, 77 (1967).

[10] A.J.P. Theuwissen, *Solid-State Imaging with Charge-Coupled Devices*, Kluwer Academic Publishers (1999).

[11] U. Schnars, J. Opt. Soc. Am. A 11, 2011 (1994).

[12] U. Schnars, W. Jüptner, Appl. Opt. 33, 179 (1994).

[13] G. Pedrini, Y.L. Zou, H.J. Tiziani, J. Mod. Opt. Soc. 42, 367 (1995).

[14] E.W. Kamen, B.S. Heck, *Fundamentals of Signals and Systems*, Prentice Hall, 2nd Ed. (2000).

[15] T. Zhang, I. Yamaguchi, Opt. Lett. 23, 1221 (1998).

[16] E. Cuche, P. Marquet, C. Depeursinge, Appl. Opt. 38, 6994 (1999).

[17] S. Seebacher, W. Osten, W. Jüptner, Proc. SPIE 3098, 382 (1997).

[18] R. Owen, A. Zozulya, Opt. Eng. 39, 2187 (2000).

[19] G. Pedrini, P. Fröning, H. Fessler, H.J. Tiziani, Appl. Opt. 37, 6262 (1998).

[20] V. Kebbel, H.J. Hartmann, W. Jüptner, Proc. SPIE 4101, (2000).

[21] C. Wagner, W. Osten, S. Seebacher, Opt. Eng. 30, 79 (2000).

[22] B. Nilsson, T. Carlsson, Opt. Eng. 39, 244 (2000).

[23] U. Schnars, T. Kreis, W. Jüptner, Opt. Eng. 35, 977 (1996).

[24] H.J. Tiziani, G. Pedrini, P. Fröning, Proc. SPIE 3407, 210 (1998).

[25] T. Kreis, W. Jüptner, *Principles of Digital Holography*, Proc. Fringe ’97, Akademie Verlag Series in Optical Metrology 3, 353 (1997).

[26] C. Wagner, S. Seebacher, W. Osten, W. Jüptner, Appl. Opt. 38, 4812 (1999).

[27] S. Inoué, K.R. Spring, *Video Microscopy*, 2nd Ed., Chapter 7.

[28] S.Lai, B. King, M.A. Neifeld, Opt. Comm. 173, 155 (2000).

[29] S. De Nicola, P. Ferraro, A. Finizio, G. Pierattini, Opt. Lett. 26, 974 (2001).

[30] Takeda, Ina, Kobayashys, J. Opt. Soc. Am. 72, 156 (1982).

Chapter 4

Characterization of optical properties of lithium niobate crystals

4.1 Introduction

Specific optical properties of LN crystal samples have been measured by using two different interferometric set-ups and DH based numerical procedures. Section 4.2 shows an interferometric method for accurate measurement of the ordinary and extraordinary refractive indices of LN crystals while Section 4.3 presents another interferometric approach for measuring the 2D distribution of the EO coefficient of LN crystals. Both measurements are innovative and provide accurate knowledge of specific LN features which are of fundamental importance for proper design and implementation of particular devices which use those crystal characteristics for applications in the field of nonlinear frequency conversion [1] and EO modulation [2]. Several methods have been presented in literature to characterize birefringent crystals such as moiré deflectometry with circular gratings [3] or Talbot interferometry [4]. Heterodyne interferometric technique has also been used for measuring the temperature dependence of refractive indices of birefringent quartz plates [5]. The method presented here allows to measure the ordinary and extraordinary refractive indices of uniaxial crystals. In case of the characterization of the 2D EO coefficient distribution many techniques, such as polarimetric Senarmont type1 and interferometric methods [6], have been presented for this purpose. Even though these methods allow to perform highly sensitive measurements, the resulting information is pointwise, useful for proper implementation of modulators used for telecom applications, where the local EO response is most important and the measured EO coefficient is obtained as integration along the probe beam direction or as average in the millimetre scale transverse section size. On the contrary, the 2D distribution presented here and consequently the information about the spatial uniformity of the EO response are desirable in case of LN based photonic applications.

4.2 Accurate measurement of the refractive indices

The technique relies on the measurement of the rotation-dependent phase changes of the optical path length (OPL) in crystal plates. An automated fast-Fourier-transform (FFT) fringe analysis method is used to retrieve the optical phase shift as a function of the sample rotation. The method is applied here to a 500 μm thick crystal wafer of *z*-cut congruent LN, polished on both faces. The method uses a MZ type interferometer set-up shown in Fig. 4.2-1. The linearly polarized expanded and collimated beam from a He–Ne laser emitting at 632 nm is divided by the beam splitter into two beams. One of these, the object beam, is incident on a Glan–Thompson polarizer (GT) and successively onto a $\lambda/2$ plate in order to rotate the linearly polarized state prior to traverse the crystal wafer. The second beam is the reference beam which passes through another combination of GT polarizer and $\lambda/2$ plate in order to rotate the linearly polarized state. The reference and object beams

are recombined at the output beam-splitter in order to get a fringe pattern resulting from the interference of the two beams, consisting of a family of equally spaced parallel straight fringes whose spatial frequency can be easily varied by tilting one of the two mirrors of the interferometer. The optical axis of the crystal is normal to its surfaces. The wafer is mounted on a high resolution motorized precision rotation stage and both object and reference beams are polarized either *s* or *p*. The object wave experiences different refractive indices depending on its polarization state, namely the ordinary index n_o when polarized *s* and the extraordinary index n_e when polarized *p*. Figure 4.2-2 shows the geometry of the refraction of the wave *SA* incident at an angle h with respect to the optic axis O.A. normal to the surface of the LN plate.

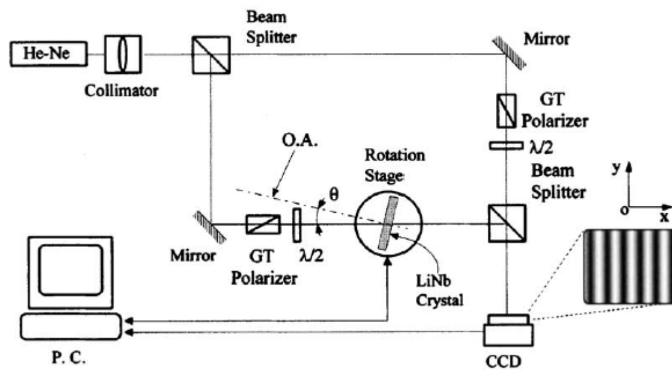

Fig. 4.2-1: Mach-Zehnder interferometer set-up for accurate measurement of $LiNbO_3$ refractive indices.

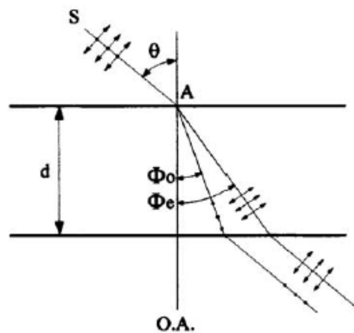

Fig. 4.2-2: Schematic view of the refraction geometry experienced by the incident wave *SA* when polarized *s* or *p*.

The plane containing the *k* vector of the incident beam and the optical axis *z* of the crystal, namely the incidence plane, coincides with the drawing plane. The polarization state of the incident wave is selected by rotating the $\lambda/2$ plate and, for each selected polarization state, independent measurements of the recorded interference fringe pattern have been performed. When the object beam is *s* polarized, namely when the polarization is normal to the drawing plane, (indicated by dot in Fig. 4.2-2) the ordinary *o*-ray exiting the object is refracted at an angle Φ_o. In order to obtain *o*-fringes, the reference beam is also *s* polarized. In this condition, a rotation of the LN crystal wafer by an angle θ respect to the direction of the *s* polarized incident beam induces a variation of the OPL of the *o*-beam exiting the object resulting in a phase change ϕ_o given by [7]

$$\phi_o = kd\left[\left(n_o^2 - \sin^2\theta\right)^{1/2} - \cos\theta - n_o + 1\right] \tag{4.2-1}$$

where $k = 2\pi/\lambda$ is the wavenumber. In order to produce *e*-fringes both the reference and the object beams are *p* polarized. The extraordinary *e*-ray exiting the object is refracted at an angle Φ_e which depends on the incidence angle θ [8] according to the relation

$$\tan\Phi_e = \frac{n_o}{n_e}\frac{\sin\theta}{\left(n_e^2 - \sin^2\theta\right)^{1/2}} \tag{4.2-2}$$

The corresponding phase change experienced by the *e*-ray exiting the object is given [7] by the following expression as a function of the incidence angle θ

$$\phi_e = kd\left[\left(n_o^2 - \left(\frac{n_o\sin\theta}{n_e}\right)^2\right)^{1/2} - \cos\theta - n_o + 1\right] \tag{4.2-3}$$

Equations (4.2-1)–(4.2-3) allow to evaluate the refractive indices n_o and n_e by independent measurements of the phase changes ϕ_o and ϕ_e through Fourier transform calculations performed on the *e*- and *o*-fringe patterns acquired by the CCD camera.

In principle, different approaches can be used, depending on the homogeneity of the sample under test. The digitised *e*- and *o*-fringe patterns could be numerically processed as a whole or in selected regions to obtain a spatially resolved information of the refractive indices or of the thickness. A simple method is described here to obtain a pointwise signal information from the recorded fringe patterns.

Figure 4.2-3 shows a typical fringe pattern recorded by the CCD camera and digitised by the frame grabber and a magnified view of the region highlighted by the white frame. The white filled area (WFA) is 2(H)×10(V) pixels large and corresponds to the pixel array portion where the numerical calculations have been performed. This area is held fixed while the interference fringe pattern crosses the field of view of the CCD array (Sony XC-77RR-CE with an array of [768×581] pixel^2 and a square pixel size of 11 μm). The intensity distribution of the interference pattern is recorded for each rotation angle θ and the corresponding intensity values recorded by the WFA are averaged to get a pointwise signal information as a function of the rotation angle θ. The values of such recorded pointwise signals are presented in Fig. 4.2-4(a)-(b) as function of the rotation angle θ for *s* and *p* polarization states, respectively.

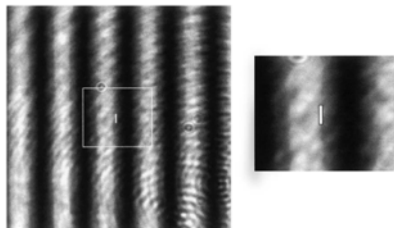

Fig. 4.2-3: (left) Typical interference pattern recorded by the CCD camera; (right) magnified view of the region highlighted by the white frame. The filled white area corresponds to pixel array where the calculations have been performed.

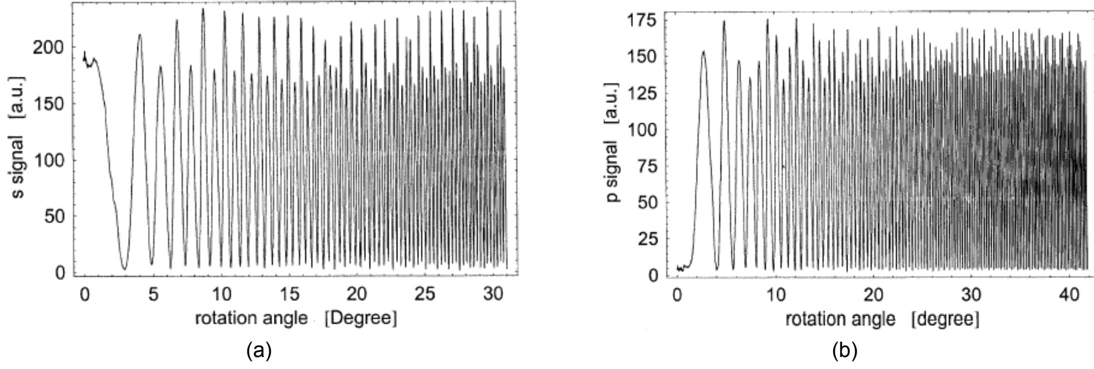

Fig. 4.2-4: Pointwise intensity signal recorded as a function of the wafer rotation angle θ. The object beam is (a) *s* polarized and (b) *p* polarized.

A data reduction method is applied here to evaluate the rotation-dependent phase changes ϕ_o and ϕ_e from the recorded *s* and *p* signals as a function of the rotation angle θ. The intensity distribution of the interference fringe pattern can be written in the following form [9] as a function of the angle θ and of the pixel location (x, y) for both *s* and *p* polarization states

$$I(\theta, x, y) = a(x, y) + b(x, y)\cos[2\pi\nu x + \phi(\theta)] \tag{4.2-4}$$

where $a(x, y)$ and $b(x, y)$ are the background of the intensity distribution and the amplitude of the interference fringes in the $(x - y)$ CCD recording plane, respectively. They are considered independent from the rotation angle θ as well as slowly varying compared to the spatial frequency ν along the x-axis. The spectrum $\hat{I}$ of the signal recorded at point (x, y) is obtained by Fourier transforming the Eq.(4.2-4) respect to θ

$$\hat{I}(f_\theta; x, y) = \delta(f_\theta; x, y) + \hat{c}(f_\theta; x, y) + \hat{c}^*(f_\theta; x, y) \tag{4.2-5}$$

where $\delta(f_\theta; x, y)$ represents a central peak of the spectrum located at the origin in the frequency domain f_θ and $\hat{c}(f_\theta; x, y)$ is the Fourier transform with respect to θ of the following function

$$c(\theta; x, y) = \frac{1}{2} b(x, y)\exp[i(2\pi\nu x + \phi(\theta))] \tag{4.2-6}$$

In Eq. (4.2-5) $\hat{c}$ and $\hat{c}^*$ correspond to the positive and negative frequencies f_θ, respectively, whereas the * represents the complex conjugate. The complex function $c(\theta; x, y)$ is obtained from (4.2-5) by windowing off the positive component $\hat{c}$ and by successive inverse Fourier transform. The rotation-dependent phase change wrapped in the range $(-\pi, +\pi)$ is then calculated by

$$\phi(\theta) = -2\pi\nu x + \arctan\left[\frac{\mathrm{Im}(c(\theta; x, y))}{\mathrm{Re}(c(\theta; x, y))}\right] \tag{4.2-7}$$

A very accurate evaluation of the phase change $\phi(\theta)$ can be obtained by taking the average of the phase change values computed from the signals recorded at different pixels of the interference fringe pattern. It is important to note that this method, compared to that previously presented in [10], does not require to determine the incremental phase change $\phi(\theta)$ from two recorded interferograms, corresponding to the incremental rotation angle $\Delta\theta$ and by consequent FFT applied to the two separate fringe patterns. Therefore, the computational procedure proposed here is easier to accomplish and requires the only limitation on the phase change $\phi(\theta) < \pi$, related to the fulfilment of the Nyquist sampling theorem.

The phase changes ϕ_o and ϕ_e of the ordinary and extraordinary waves are monotonically increasing functions of the rotation angle θ. For example, when θ=20°, for λ=632.8 nm and d=0.5 mm, ϕ_o(20°)=171.32 rad and an angle increment from 20° to 20.1° results in a phase change ϕ_o(20.1°)=173.05 rad, corresponding to a variation of the fringe number (ϕ_o(20.1°)-ϕ_o(20°))/2π=0.275 that crosses the field of view. A rotation angle θ=30° gives ϕ_o(30°)=389.59 rad and the corresponding variation of the fringe number is (ϕ_o(30.1°)-ϕ_o(30°))/2π=0.421. The effects of the error in the phase measurement is evaluated by considering a change $\Delta n_0=10^{-3}$ of the ordinary refractive index n_0=2.28, which results in a variation of the fringe number of $\Delta\phi_o/2\pi$=0.422 when θ=30°. Similarly, a change by $\Delta n_e=10^{-3}$ in the extraordinary refractive index n_e=2.20 results in a variation of the fringe number of $\Delta\phi_e/2\pi$=0.401 when θ=30° and of $\Delta\phi_e/2\pi$=0.552 when θ=40°.

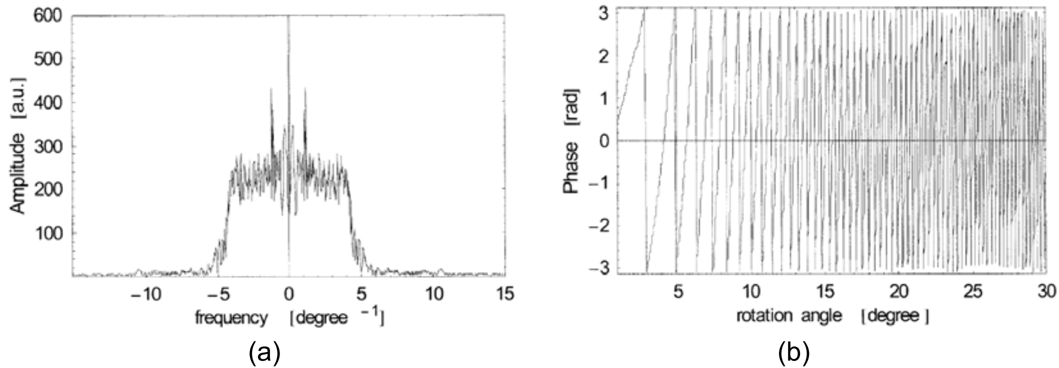

(a) (b)

Fig. 4.2-5: (a) Fourier transform of the *s* polarization signal; (b) wrapped phase ϕ_o versus the rotation angle of the crystal wafer.

The interference fringe patterns are recorded and digitised into a (512×512) pixel^2 array in the horizontal (x) and vertical (y) directions, respectively. The fringe pattern contains approximately 20 fringes, corresponding to a spatial frequency of ν ~0.039 fringe/pixel. As described before, the variation of the interference signal versus the rotation angle is obtained by averaging the values of the intensity recorded inside the WFA of the digitised fringe pattern. The *s* and *p* polarization interference signals are acquired at a rotation angle increment $\Delta\theta$ of 0.01° ranging from 0° (normal incidence) up to 30° for the *s* signal and to about 40° for the *p* signal. The angular resolution of the motorized rotation stage is 0.001° and the measured thickness of the LN wafer is d=498±1 μm. At normal incidence, the optical axis of the crystal wafer is along the direction of the incidence beam. An alignment procedure is performed to set the zero angle of incidence by superimposing the spot of the beam reflected by the crystal surface on that of the incident beam. The Fourier transform of the two signals is shown in Figs. 4.2-5(a) and 4.2-6(a).

As described before, a Fourier-based transform method is applied to these spectra to obtain the wrapped phase vs. the rotation angle, as shown in Figs. 4.2-5(b) and 4.2-6(b) for the *s* and *p* polarization signals, respectively. The rotation-dependent phase changes ϕ_o and ϕ_e of the ordinary and extraordinary waves are presented in Fig. 4.2-7(a)-(b), respectively.

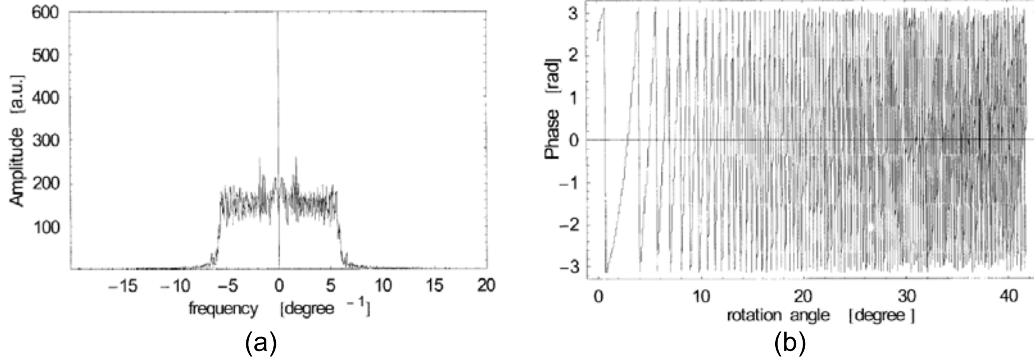

Fig. 4.2-6: (a) Fourier transform of the *p* polarization signal; (b) wrapped phase ϕ_e versus the rotation angle of the crystal wafer.

The phase changes are determined by applying the unwrapping procedure [11] to the wrapped phase data of Figs. 4.2-5(b) and 4.2-6(b). Data analysis is performed by writing Eqs. 4.2-1,2,3 in the following form:

$$\phi_o = off + kd\left[\left(n_o^2 - \sin^2(\theta - \theta_o)\right)^{1/2} - \cos(\theta - \theta_o) - n_o + 1\right] \quad (4.2\text{-}8)$$

$$\phi_e = off + kd\left[\left(n_o^2 - \left(\frac{n_o \sin(\theta - \theta_o)}{n_e}\right)^2\right)^{1/2} - \cos(\theta - \theta_o) - n_o + 1\right] \quad (4.2\text{-}9)$$

where two additional parameters have been added to improve the quality of the numerical fit of the experimental data: the parameter *off* to account for the arbitrary initial value of the phase and the quantity θ_o to account for a possible slight misalignment of the crystal optical axis to set when setting the zero angle of the wafer as described before.

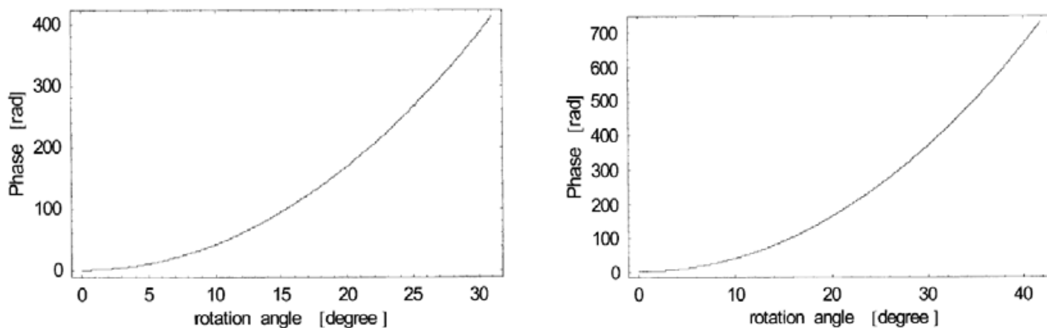

Fig. 4.2-7: (a) Phase shift ϕ_o and (b) ϕ_e measured as function of the rotation angle of the crystal wafer.

A nonlinear least squares fitting procedure on the unwrapped phase data shown in Fig. 4.2-6 is performed by using the Eqs. 4.2-8,9 to determine the ordinary and extraordinary refractive indices of the LN crystal: n_o= 2.2772±0.0009 and

n_e=2.2035±0.0002. Several measurements have been performed on the crystal sample showing the reproducibility of the experimental results.

4.3 Two-dimensional mapping of the electro-optic coefficient

An interferometric method based on DH is presented here for the quantitative determination of the 2D spatially resolved mapping of the EO phase retardation in *z*-cut congruent LN crystals. A quantitative 2D measurement of the OPD caused by an external voltage is performed to obtain a spatially resolved map of the EO phase retardation. An interferometric set-up based on two components, a reflective grating (RG) (44×44) mm^2 large with 1200 lines/mm and a mirror, is used to record digital holograms as shown in Fig. 4.3-1.

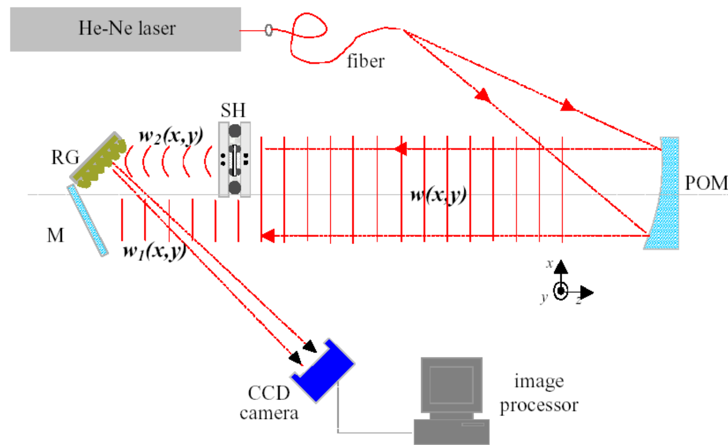

Fig. 4.3-1: Schematic view of the reflective grating interferometer (RGI) used for the measurement of the phase retardation map related to the EO effect in LN crystals.

A He-Ne laser emitting at 632.8 nm is launched into a single mode optical fibre and expanded to a spherical wave which impinges onto the off-axis parabolic mirror *POM* to obtain a plane wave-front beam. The collimated wave-front $w(x,y)$ is spatially divided in two half wave-fronts, the reference $w_1(x,y)$ and the object $w_2(x,y)$, by the mirror and the RG respectively. The wave-front $w_1(x,y)$ is reflected onto the RG by the mirror and the angle of incidence of the two half wave-fronts on the RG is such that both of them are diffracted along the normal to the RG. The wave-front $w_1(x,y)$ is folded onto $w2(x,y)$ to get an interference pattern in front of the RG at a distance d from the sample along the beam path. The fringe pattern is digitised by a CCD camera with (512×512) square pixels 11.7 µm sized. The field of view captured by the CCD array is around (5×5) mm^2 sized. The object beam is a plane wave front traversing the crystal sample along its *z* axis by using a special plexiglas mount which allows simultaneously the application of the external voltage and the laser light access (see Fig. 4.3-2).

Electrical contact on the sample surfaces is obtained by a liquid electrode configuration consisting of two electrolyte containing chambers which squeeze the sample between two *O*-ring gaskets. Tap water is used as liquid electrolyte. This configuration insures both the homogeneity of the external electric field within the sample, due to the uniform adhesion of the electrolyte to the crystal surface, and transparency along the *z* direction, which allows illumination of the sample through

the quartz windows with minimal wave-front distortion. A conventional Signal Generator (*SG*) drives an High Voltage Amplifier (*HVA* - 2000×) to deliver the high voltage external signal.

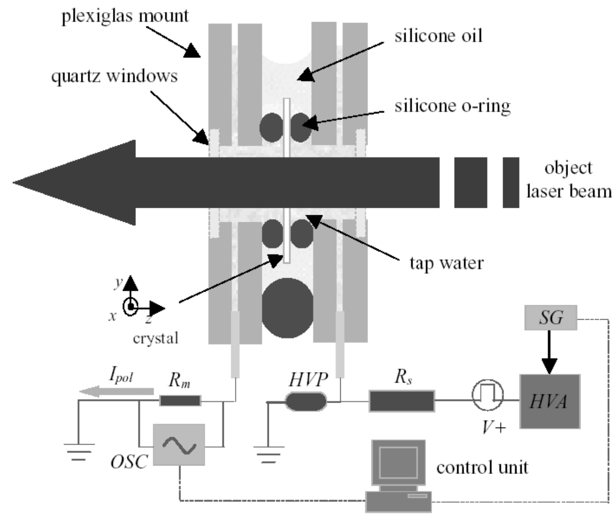

Fig. 4.3-2: Schematic view of the plexiglas mount used for simultaneous external voltage application and laser light access along the *z* crystal axis. *SG* signal generator; *HVA* high voltage amplifier; R_s series resistor; *HVP* high voltage probe; R_m monitoring resistor; *OSC* oscilloscope; I_{pol} poling current.

Two *z*-cut LN crystal wafers have been investigated with congruent (500 μm thick) and off-congruent composition (1 mm thick). The numerical reconstruction of the complex amplitude of the object wavefield, propagated back to the object plane at distance *d* along the beam path, has been performed by a DH procedure based on Fresnel transformation applied to the acquired holograms. Both amplitude and phase of the wave front can be readily extracted from the reconstructed complex wave field. The complex object wavefield $O(x,y)$ at the reconstruction plane (x,y) is numerically calculated from the Fresnel diffraction integral

$$O(x,y) \propto \iint h(x',y')r(x',y')\exp\left[\frac{i\pi}{d\lambda}\left(x'^2+y'^2\right)\right]\times\exp\left[-\frac{2i\pi}{\lambda d}\left(x'x+y'y\right)\right]dx'dy' \qquad (4.3\text{-}1)$$

where $h(x',y')$ is the digitised fringe pattern and (x',y') are the recording plane coordinates. The complex field of the object at distance *d* can be reconstructed by use of a discrete finite form of expression (4.3-1). The method used here consists in a double-exposure DH interferometry. A linear voltage ramp is applied across the sample while the CCD array records a set of 50 digital holograms at a rate of 10 frame/s. The first hologram $h_0(x',y')$ at zero voltage serves as first exposure and each of the successive holograms $h_i(x',y')\; i=1,....,50$ is one of the 50 holograms acquired during the application of the voltage ramp. The recorded holograms $h_0(x',y')$ and $h_i(x',y')$ are numerically reconstructed at distance *d*=300 mm by means of (4.3-1) to obtain the complex wavefields $O_0(x,y)$ and $O_i(x,y)$. Thus the phase difference at the reconstructed image plane is calculated as

$\Delta\phi_i(x,y) = Arg[O_i(x,y)/O_0(x,y)]$. The correct focusing distance is found by a calibrated target at the sample position. The sensitivity of the technique in resolving crystal anomalies is calculated by use of the rms of the phase map of a recorded hologram and a 0.07 rad rms value has been found. The spatial resolution in the (x,y) reconstructed plane is $\Delta x = \Delta y = 34$ μm, according to the reconstruction pixel formula in (3.3.3-6).

The external voltage V induces a phase retardation $\Delta\phi$ due to the combination of the linear EO and PZ effects. The direction of the external electric field and of the object beam are collinear with the *z* axis of the crystal. In this configuration the phase retardation is

$$\Delta\phi(x,y) = \frac{2\pi}{\lambda}(l\Delta n + n_0\Delta l) = \frac{2\pi}{\lambda}\left\{\frac{1}{2}\left[-r_{13}(x,y)n_0^3 + 2(n_0 - n_w)k_{33}(x,y)\right]V\right\} \quad (4.3\text{-}2)$$

where n_w is the refractive index of water, n_o the LN ordinary refractive index, and r_{13} is the EO coefficient. The PZ thickness change Δl is dependent on k_{33}=7.57×10^{-12} m/V, the ratio between the linear PZ and the stiffness tensor [12]. The phase change is related to the OPD between the object and the reference beam related to the presence of the sample in the holographic set-up. The reconstructed phase difference map between the reference hologram and the holograms recorded during the 0–5 kV linear voltage ramp provides the EO related phase retardation map of the sample based on the measurement of the incremental phase difference for each digitised hologram.

Figure 4.3-2(a) shows the 2D map of the EO coefficient $r_{13}(x,y)$ measured for a congruent LN wafer, uniformly 500 μm thick, where the scale bar indicates the distribution of r_{13} values. Assuming negligible the errors of k_{33}, V and refractive indices values and taking into account an *rms* value of 0.07 rad for the hologram phase map, the sensitivity of the technique in measuring the EO coefficient is calculated to be 0.2 pm/V. An average value of r_{13} is evaluated by considering a electro-optically uniform area of the sample. The data of the phase maps reconstructed for each hologram and corresponding to the selected area have been averaged and linear best fit procedure for incremental values of the external voltage have been performed as shown in Fig. 4.3-2(b). A value of r_{13}=10.0±0.1 pm/V has been obtained form the linear fit, in agreement with the specifications of the LN crystal supplier (Crystal Technology).

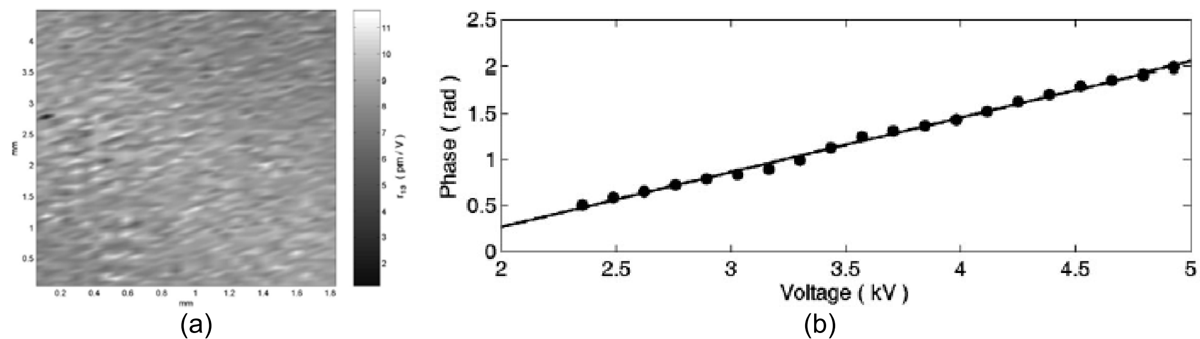

Fig. 4.3-2: (a) Reconstructed 2D map of the EO coefficient $r_{13}(x,y)$ of a 500 μm thick congruent LN wafer where the scale bar represents the distribution of the $r_{13}(x,y)$ values; (b) experimental point data and corresponding fitting line from which the r_{13} coefficient was evaluated by averaging the data inside a selected area of the reconstructed phase maps of the digitised holograms.

Figure 4.3-2(a) clearly shows that the EO phase retardation is not uniform over the sample. In fact, the calculated value of r_{13} on a (4.5×1.8) mm^2 area shows an *rms* value of 2 pm/V, corresponding to a spatial variation of as much as 20% with respect to the average value. This spatial distribution of the EO coefficient is due to a lack of uniformity in the crystal structure that is well known anecdotally but has not been quantitatively investigated by 2D mapping.

The technique has been applied also to an engineered congruent LN crystal sample where a ferroelectric reversed domain has been fabricated by electric field poling. The reconstructed phase map is shown in Fig. 4.3-3, where an equal modulus but opposite sign of r_{13} is obtained in the two adjacent areas with opposite orientation of the ferroelectric polarization.

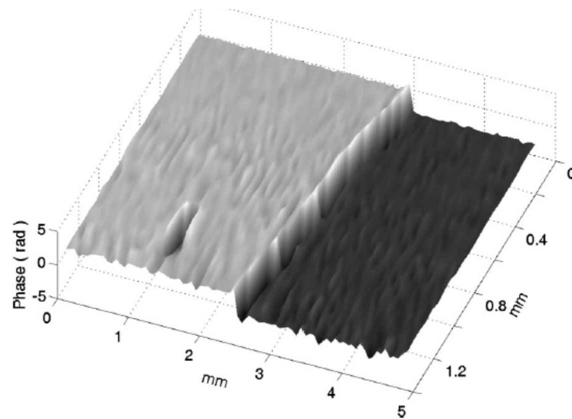

Fig. 4.3-3: Surface representation of the 2D phase map distribution reconstructed at 5 kV for a congruent 500 μm thick LN sample with two oppositely oriented ferroelectric domains. A small polarization reversed area is visible in the left un-reversed region of the crystal.

A small reversed area is visible in the un-reversed left region, probably due to an unwanted non-uniform ferroelectric domain nucleation during the electric field poling, which usually affects the quality of the domain engineered crystals. The same measurements have been performed on an OCLN crystal wafer where two oppositely oriented ferroelectric domains have been obtained by EFP. Figure 4.3-4 shows the corresponding 2D phase map of the crystal. An inverted domain grown around non-stoichiometric defect of the crystal is visible.

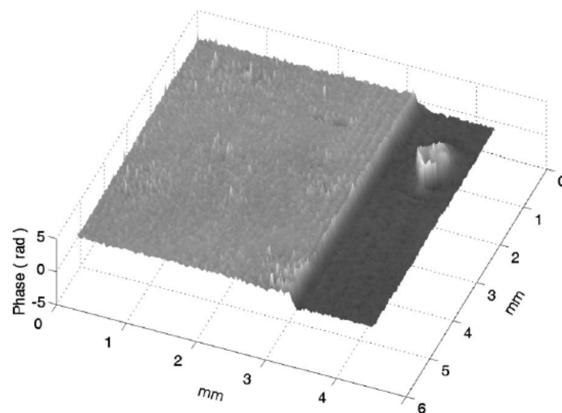

Fig. 4.3-4: Surface representation of the 2D phase map distribution reconstructed at 2.7 kV for an off-congruent 1 mm thick LN sample with two oppositely oriented ferroelectric domains. An inverted area grown around a non-stoichiometric defect of the crystal is clearly visible.

References Chapter 4

[1] M.M. Fejer, G.A. Magel, D.H. Jundt, R.L. Byer, JQE28-2631(1992).

[2] L. Arizmendi, Phys. Stat. Sol. A 201, 253 (2004).

[3] D.F. Heller, O. Kafri, J. Krasinski, Appl. Opt. 24, 3037 (1985).

[4] J.C. Bhattacharya, Appl. Opt. 40, 1658 (2001).

[5] S. De Nicola, G. Carbonara, A. Finizio, G. Pierattini, Appl. Phys. B 58, 133 (1994).

[6] P. Ney, A. Maillard, M.D. Fontana, K. Polgar, J. Opt. Soc. Am. B 17, 1158 (2000).

[7] R.M.A. Azzam, N.M. Bashara, *Ellipsometry and polarized light*, Elsevier North-Holland Personal Library (1997).

[8] F.D. Bloss, *Introduction to the methods of optical crystallography*, Harcourt School.

[9] M. Takeda, H. Ina, S. Kobayashi, J. Opt. Soc. Am. 72, 156 (1982).

[10] S. De Nicola, P. Ferraro, A. Finizio, G. Pierattini, S. Pelli, J. Opt. A 1, 702 (1999).

[11] T. Kreis in P.K. Rastogi (Ed.), *Holographic Interferometry*, Springer, Berlin, 184 (1994).

[12] M. Jazbinsek, Appl. Phys. B 74, 407 (2002).

Chapter 5

Properties related to the electric field poling

5.1 Introduction

Different properties of LN and KTP ferroelectric crystals related to the EFP are investigated and characterized here by DH based procedures. In Section 5.2 in-situ characterization of both morphological and dynamic evolution of reversed domains during EFP is performed by using the PZ and the EO effects occurring during the application of the external voltage. The results are novel in this field and provide interesting information about the behaviour of reversing domains in LN and KTP crystals during EFP, which are of great importance in the field of PPLN and PPKTP manufacturing. Section 5.3 deals with the characterization of the so called IF exhibited by LN crystals in reversed domains and related to the presence of non-stoichiometric crystal defects. Novel direct measurements of the static and elastic component of such IF are presented. In fact, nowadays the IF in LN crystals has been studied only empirically by the measurement of the difference between forward and backward poling fields [1,2]. Section 5.4 shows the topographic characterization of surface structures fabricated in LN by EFP and subsequent selective wet etching. The advantages of non-contact and wide field visualization provided by DH procedure are discussed.

5.2 *In-situ* characterization of domain switching in ferroelectric crystals

A DH (see Chapter 3) based technique has been used here for *in-situ* characterization of ferroelectric domain switching in congruent LN and flux grown KTP crystal samples, by using the electro-optically induced phase difference across domain walls. In fact, it is well known (see Chapter 2) that ferroelectric materials, such as LN and KTP, exhibit EO and PZ effects. In case of the linear EO effect along the *z* crystal axis, a refractive index change Δn occurs when the material is subjected to a uniform external electric field. The sign of this refractive index change depends on the domain orientation according to $\Delta n \propto r_{13}E_3$, where E_3 is the external electric field parallel to the *z* crystal axis and r_{13} is the appropriate EO tensor element. Therefore the refractive index n increases from n to $n+\Delta n$ in one domain and decreases from n to $n-\Delta n$ in the oppositely oriented one. This provides a refractive index step $2\Delta n$ across the domain wall which consequently becomes optically visible through the diffraction effect, largely used for *in-situ* EO imaging of electric field domain reversal in ferroelectric materials [3,4]. The refractive index step $2\Delta n$ induces a phase shift to a laser beam traversing the crystal sample along its *z* axis direction. In case of the linear PZ effect, along the *z* crystal axis, the external voltage induces a negative or positive sample thickness variation Δd depending on the domain orientation according to $\Delta d = d_{33}E_3$, where d_{33} is the ratio between the appropriate piezoelectric and stiffness tensor element. Therefore, during EFP, the phase retardation $\Delta\phi$ experienced by a plane wave incident along the *z* crystal axis,

is mainly affected by the refractive index change due to the linear EO effect and by the thickness variation due to the linear PZ effect, according to

$$\Delta\phi = 2\left[\frac{2\pi}{\lambda}\Delta n d + \frac{2\pi}{\lambda}(n_0 - n_w)\Delta d\right] = \frac{2\pi}{\lambda}\left[-r_{13}n_0^{\ 3} + 2(n_0 - n_w)d_{33}\right]U \quad (5.2\text{-}1)$$

where n_w=1.33 is the water refractive index, U =1.25 kV is the external applied voltage and the values of the other parameters are indicated in Tab.5.2-1 for LN and KTP.

	d (mm)	n_o	r_{13} (pm/V)	d_{33} (m/V)
$LiNbO_3$	0.5	2.29	10	7.57×10^{-12}
$KTiOPO_4$	0.5	1.78	9.5	20×10^{-12}

Tab. 5.2-1. Values of the parameters in equation (5.2-1) for LN and KTP crystals.

Crystal samples (20×20×0.5) mm^3 sized are obtained by dicing single domain crystal wafers polished on both sides. The room temperature EFP is carried out by using the sample holder shown schematically in Fig. 4.3-2. Domain inversion is achieved by applying positive high voltage to the *z+* crystal face, slightly exceeding the coercive field of the material (around 21 kV/mm for LN and 2 kV/mm for KTP). In case of LN an appropriate resistor is used to limit the current flowing in the circuit and related to the displacement current I_{pol} due to the charge redistribution within the crystal structure. This current is measured by acquiring the voltage drop across the resistor R_m through the oscilloscope *OSC* (see Fig. 4.3-2).

The sample holder is positioned into one arm of a specific interferometer set-up for each kind of experiment performed here. Section 5.2.1 shows the results concerning the *in-situ* visualization of reversing ferroelectric domains in congruent LN by using the RG interferometer (RGI) set-up described in Section 4.3. This configuration provides relatively poor spatial resolution. Section 5.2.2 presents the in-situ imaging of slow and fast domain reversal process in congruent LN by using the MZ set-up shown in Fig. 5.2-1 equipped with a Nd:YAG doubled laser source emitting at 532 nm and a fast CCD or CMOS camera, respectively. The two different poling regimes are obtained by using an appropriate series resistor in the external circuit, the higher the resistor is the slower is the poling process. This configuration allowed to improve the spatial resolution compared to the RGI set-up, thanks mainly to the shorter reconstruction distance. The MZ set-up shown in Fig. 5.2-1 is used also for the *in-situ* characterization of domain reversal in KTP samples by using a CMOS camera with an acquisition rate of about 900 *f/s*, thus able to record the domain switching evolution of reversing domains in KTP samples with a reasonable temporal resolution. The corresponding results obtained for different voltage waveforms are shown in Section 5.2.3 while Section 5.2.4 presents a comparison of the domain reversal dynamic characteristics obtained for each kind of experiment and material.

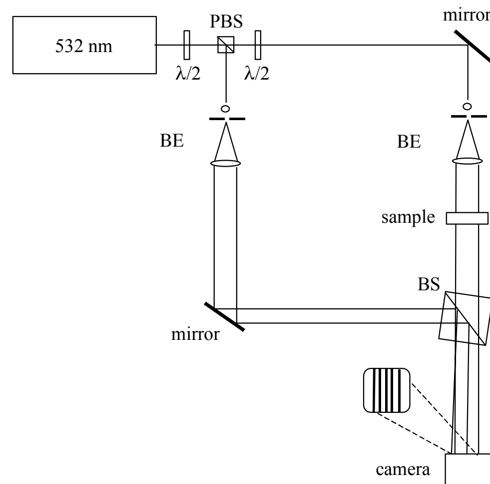

Fig. 5.2-1: Schematic view of the MZ set-up used for the *in-situ* visualization of slow and fast domain reversal process in congruent LN. A fast CCD or a CMOS camera is used for slow and fast poling regimes, respectively. *PBS* polarizing beam-splitter; *BE* beam-expander; *BS* beam-splitter.

5.2.1 In-situ domain reversal imaging in $LiNbO_3$ by the RGI

Figure 5.2.1-1 shows one representative frame of the movie showing the evolving interferogram acquired by the CCD camera during the EFP of a virgin LN sample (see movie in Paper IV). The video frames have a temporal resolution of 10 frame/s. The sample has been coated with a thin film of insulating material (photoresist) with a square opening window (5×5) mm^2 sized, corresponding to the electrode area. The stationary diffraction effect of the opening window edge is clearly visible and superimposed to the linear interferogram (straight lines). The polarization axis is normal to the image and the field of view is slightly larger than the electrode area. The domain switching of the crystal polarization under the electrode area took about 5 s. The out of focus diffraction image of the domain walls growing from the resist edges is clearly superimposed onto the interference fringe pattern. They move towards the centre until the spontaneous polarization of the crystal under the electrode area is completely reversed.

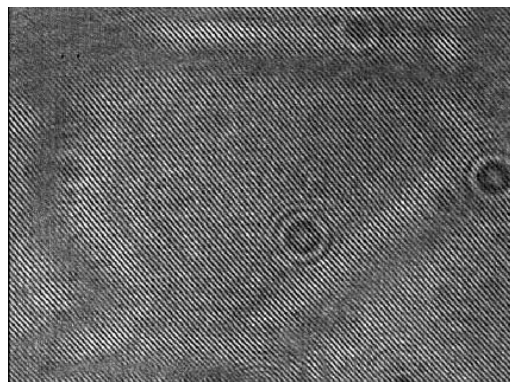

Fig. 5.2.1-1: Representative frame of the interferogram movie recorded during EFP. The temporal resolution is around 10 frame/s. The polarization axis is normal to the image plane.(movie in Paper IV)

The visibility of the domain wall under transmitted light is determined by the opposite phase shift induced on the reversed domains by the linear EO and PZ effects along the *z* crystal axis, as mentioned before. The DH technique is applied to all of the recorded interferograms to reconstruct the corresponding 2D amplitude maps of the object wavefield which are then collected into an amplitude movie, whose representative frame is shown in Fig. 5.2.1-2 (see movie in Paper IV). The reconstruction distance is *d*=540 mm. The amplitude movie provides a full-field visualization of the evolving domain walls, thus allowing to have *in-situ* information about the spatial evolution of the reversed domain pattern. It is clearly visible that domain nucleation preferentially starts at the edges of the electrode area. Then, domains merge to form a few dominant domain wall fronts. The lateral resolution achieved in these images is around 55 μm, according to Eq.(3.3.3-6).

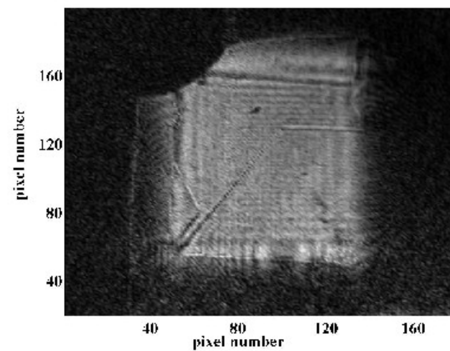

Fig. 5.2.1-2: Representative frame of the amplitude movie showing the evolution of the domain walls. The polarization axis is normal to the image plane. (see movie in Paper IV)

A reference interferogram of the sample at its initial virgin state is acquired when the external voltage is not applied. With respect to this, the phase shift experienced by the object wavefield during the EFP is calculated. The DH reconstruction is performed for both the reference hologram and the *n*th hologram recorded during the domain switching, to obtain the corresponding object wavefield phase distributions $\phi_0(x',y')$ and $\phi_n(x',y')$. The 2D map of the phase shift $\Delta\phi(x',y')=\phi_n(x',y')-\phi_0(x',y')$ is calculated for each hologram and the corresponding images are collected into a phase movie, whose representative frame is presented in Fig. 5.2.1-3 (see movie in Paper IV).

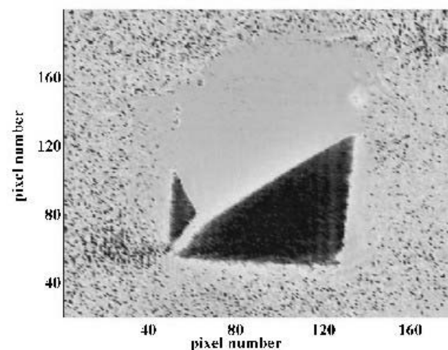

Fig. 5.2.1-3: Representative frame of the phase movie showing the evolution of the reversed domain regions. The *z* axis is normal to the image plane. (see movie in Paper IV)

The out of focus real image and the zeroth order diffraction term, generated by the DH numerical procedure (see Chapter 3), are filtered out for clarity. Moreover, the anamorphism effect visible in Fig. 5.2.1-1 as deformed shape of the square resist window, is corrected numerically by inserting the $\cos\alpha$ factor in the diffraction formula (see Eq.3.3.3-4) [Ref 30 in Chapter 3]. The amplitude and the phase movies provide different and complementary information. The phase movie, with its quantitative phase mapping, provides information on the local orientation of the ferroelectric polarization thus allowing to discriminate between reversed and un-reversed regions. Moreover, it gives in-situ evaluation of the amount of optical path difference occurring across adjacent reversed domains allowing a quantitative study of domain wall behaviour related to crystal defects. Furthermore, the quantitative 2D phase mapping during EFP provides the opportunity to investigate *in-situ* the eventual relationship between the poling behaviour and the non-uniform EO response. On the other hand, the phase movie lacks of information about the resist pattern since its contribution to the phase retardation, constant during the EFP, is eliminated by the phase difference calculation. On the contrary, the amplitude movie gives qualitative information about the domain wall evolution ignoring the polarization orientation, but on the other hand it preserves the information about the resist pattern whose amplitude image is reconstructed together with that of the domain walls.

Surface plot images of the unwrapped phase maps are obtained and collected into a surface movie, to reveal the evolving profile of the phase shift occurring at domain boundaries. Figure 5.2.1-4 presents the representative frame of such surface movie (see the movie in Paper IV). The mean value of the phase shift occurring across the domain boundaries is calculated to be around 3.6 rad. Such value is in good agreement with the theoretical one calculated by Eq.5.2-1 in case of LN, apart from a modulo 2π shift. Mean value and variance of the 2D distribution of both the amplitude $A_{ref}(x',y')$ and the phase $\Delta\phi_{ref}(x',y')$ reconstructed for the reference hologram are calculated to estimate the accuracy of the method. The mean value of the reference amplitude is (4.7×10^{-4}) a.u. with a variance of 0.09 a.u., while the mean value of the reference phase is 0.82 rad with a variance of 0.11 rad corresponding to about $\lambda/60$.

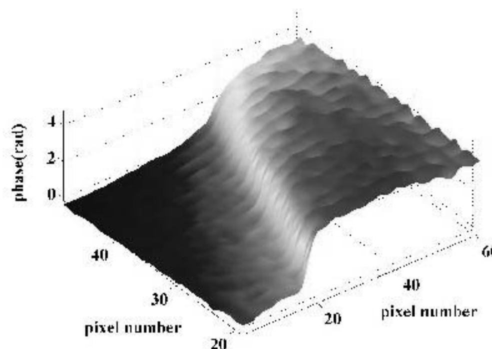

Fig. 5.2.1-4: Representative frame of the surface movie. (see the movie in Paper IV)

The technique has been applied to another LN sample, previously processed by EFP to obtain two adjacent antiparallel domains, in order to investigate the method in presence of a domain wall. Figure 5.2.1-5 and Fig. 5.2.1-6 show the representative frames of the corresponding amplitude and phase shift movies (movies are in Paper IV). The reconstruction distance is d=570 mm.

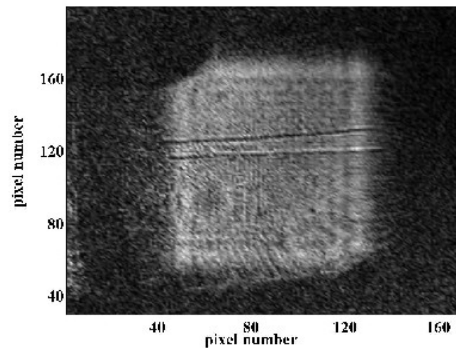

Fig. 5.2.1-5: Representative frame of the amplitude movie in case of pre-existing domain wall. The *z* axis is normal to the image plane. (see the movie in Paper IV)

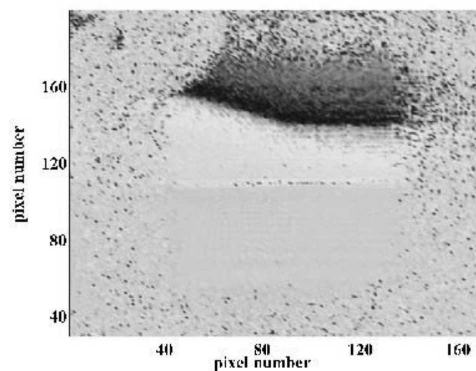

Fig. 5.2.1-6: Representative frame of the phase movie in case of pre-existing domain wall. The *z* axis is normal to the image plane. (movie in Paper IV)

The standing horizontal line visible in both amplitude and phase movie corresponds to the pre-existing domain wall. It is interesting to note that the phase images show the phase changing in the region across the two merging domains. Such localized phase shift distribution could be due to refractive index stresses occurring across reversing domain walls and still present as residuals on domain boundaries after EFP [5].

5.2.2 In-situ domain reversal imaging in $LiNbO_3$ by the MZ

Two different configurations have been used here. In case *A* the LN sample is subject to slow poling process [6] by using high resistor the external circuit (100 MΩ). The whole area under investigation (diameter 5 mm) is reversed in about 10 s and the interferograms are acquired by a CCD camera with a temporal resolution of about 12 f/s. In case *B* another virgin LN crystal sample is reversed by fast poling (5 MΩ series resistor) in order to reverse the whole electrode area in less than 1 s and a CMOS camera is used to record the interferograms with a temporal resolution of about 900 f/s. Amplitude and phase maps of the object wavefield are numerically reconstructed by the DH method. The reconstruction distance is 125 mm in case *A* and 180 mm in case *B*, while the lateral resolution obtained in the reconstructed amplitude and phase images is 9.7 μm in case *A* and 16 μm in case *B*, according to Eq.(3.3.3-6). Therefore, basically the smaller camera pixel size of the CCD camera

(7.6 μm against 12 μm pixel size in CMOS camera) provides better spatial resolved images while the CMOS camera provides higher temporally resolved images.

Similarly to the experiments illustrated in section 5.2.1, a reference interferogram of the sample at its initial virgin state is acquired before applying the external voltage and it is used to calculate the phase shift experienced by the object wavefield during the EFP. The DH reconstruction is performed for both the reference hologram and the *n*th hologram, recorded during the domain switching, to obtain the corresponding phase distributions $\phi_0(x',y')$ and $\phi_n(x',y')$. The 2D phase shift map $\Delta\phi(x',y') = \phi_n(x',y') - \phi_0(x',y')$ is calculated for each hologram and the corresponding images are collected into a phase shift movie. Figure 5.2.2-1 and Fig. 5.2.2-2 show the representative frame of the phase movie in case *A* and *B*, respectively. As described previously the out of focus real image term, generated by the DH numerical procedure, is filtered out for clarity. The in focus image of the domain wall propagating during the application of the external voltage is clearly visible. Switching process always starts with nucleation at the electrode edges. It is interesting to note that a residual phase shift gradient is left behind by the evolving domain walls, as clearly shown by the better resolved images in Fig. 5.2.2-1. This is probably due to the decay effect of the IF related to the polarization hysteresis in ferroelectric crystals (see Chapter 2). It is important to note that crystal defects are also clearly visible and readily detectable (see Fig. 5.2.2-1) due to their different EO behaviour. Moreover the high temporal resolution of the movie in Fig. 5.2.2-2 allows to notice that the evolution of the domain walls is clearly affected by the crystal defects which appear to behave as pinning points for the domain wall propagation. Further studies concerning the gradient phase shift behind domain walls and the application of the method with different external voltage waveforms, for characterization of domain reversal evolution, are currently under investigation.

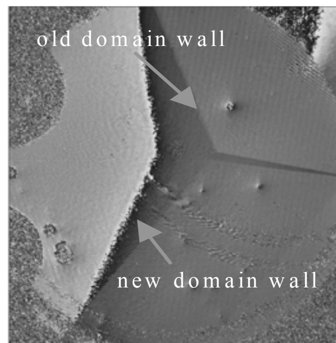

Fig. 5.2.2-1: Representative frame of the phase movie reconstructed in case *A*. The frame area is (5x5) mm^2. The polarization axis is normal to the image plane.

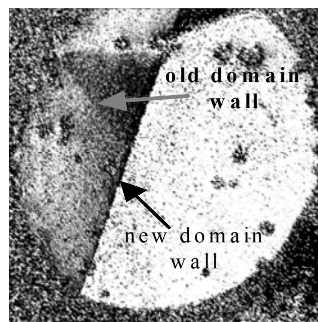

Fig. 5.2.2-2: Representative frame of the phase movie reconstructed in case *B*. The frame area is (5x5) mm^2. The polarization axis is normal to the image plane.

5.2.3 *In-situ* domain reversal imaging in KTP by the MZ

The dynamic behaviour of KTP samples during EFP is investigated here in case of three different voltage waveforms: square pulse (SP); train of square pulses (TSP); triangular pulse (TP). The SP is 100 ms long, the TSP consists of a sequence of 20 ms long square pulses with 50% duty cycle and the TP is 100 ms long with a rate of 68.8 V/ms up to 3.4 kV/mm. Several electric field magnitudes have been tested for SP and TSP waveforms but the characterization presented here refers to a fixed voltage of 2.5 kV/mm since no substantial differences have been observed. If necessary, more than one pulse has been applied in order to complete the polarization switching in the whole electrode area. The MZ set-up shown in Fig. 5.2-1 is used to acquire the holograms during the application of the external voltage by using a CMOS camera whose frame rate acquisition (around 900 f/s) allows to record the high-speed domain wall evolution in KTP samples with a reasonable temporal resolution. In fact, ex-situ investigations report that domain wall velocity is relatively high in KTP material (about few μm/ms) [7].

As usual a reference interferogram of the sample at its initial virgin state is acquired before the application of the external voltage. The 2D phase shift distribution, experienced by the object wavefield during EFP, is calculated for each hologram respect to the reference one. Figure 5.2.3-1 show the representative frame of the reconstructed phase movie in case of SP, TSP and TP. The reconstruction distance is d=188 mm in each case, so that the lateral resolution achieved in the phase images is about 16 μm, according to Eq.(3.3.3-6). As usual, both the out of focus real image and the zeroth order diffraction term are filtered out.

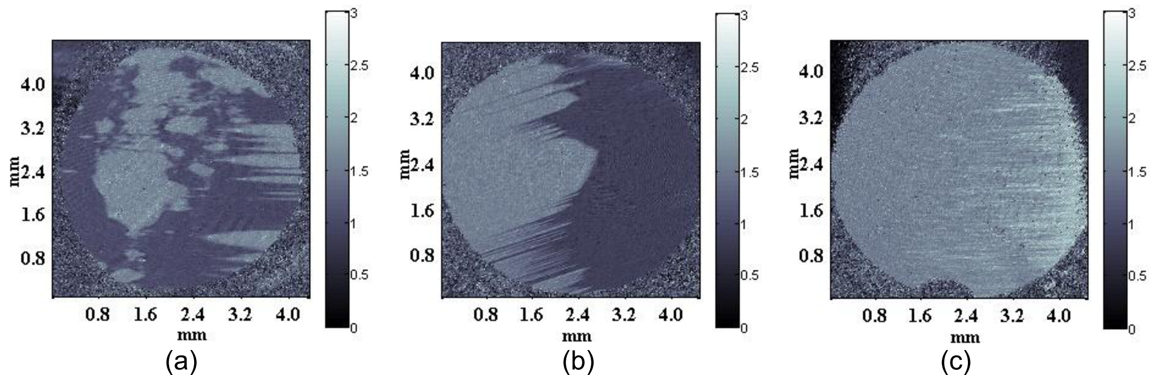

Fig. 5.2.3-1: Representative frame of the phase movie reconstructed in case of (a) SP; (b) TSP; (c) TP. The frame area is (5x5) mm^2. The polarization axis is normal to the image plane while the *y* crystal axis is in the image plane oriented along the horizontal direction in case of SP and TP and along about 45° direction in case of TSP.

In order to reverse the whole electrode area, four pulses has been required in case of SP, two in case of TSP and only one in case of TP. The wide field imaging and the relatively high spatial and temporal resolution of the phase shift movies allow to characterize both the morphology and the dynamic properties of electric field domain switching in flux-grown KTP for the three different voltage waveforms.

In case of SP the EFP exhibits an incubation time, meaning that a time delay is observed from the beginning of the external voltage to the significant growth of reversed domains. In order to show that non significant domain evolution occurs during the incubation state, the phase shift distribution between the two holograms corresponding to the beginning and the end of the incubation state is evaluated and presented in Fig. 5.2.3-2(a).

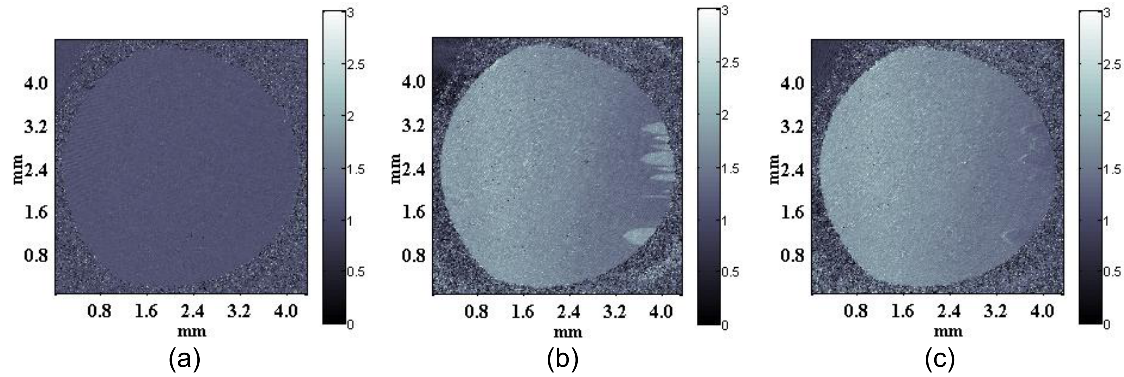

Fig. 5.2.3-2: Phase shift distribution calculated between the two holograms corresponding to the beginning and the end of (a) the incubation state; (b) the motion state; (c) the stationary state, during the first SP.

It is clear that, within the resolution limit of the method, no significant phase shift is revealed, meaning that no significant domain growth occurs during the incubation state. The existence of an incubation time has been observed by other methods in other materials [1,8] and is probably due to the capacitive charge layers present on the surface of the crystals for neutralizing the electric field related to the spontaneous polarization. A parabolic variation of the ionic conductivity, along the *y* crystal axis direction, has been reported for flux grown KTP wafers [7] and the phase shift movie in Fig. 5.2.3-1(a) shows that, after the incubation time, the reversed domains start growing from the electrode edge, where the electric field is enhanced by fringing field effects, corresponding to the lower conductive region of the KTP wafer. The reversed domains clearly start growing with a pencil-like shape elongated along the y crystal axis and move anisotropically towards the central region of the crystal. In fact, the domain wall velocity along the *y* crystal axis is clearly higher than that along the *x* crystal axis. The pencil-like domains evolve with an almost constant arial velocity for a specific time range (motion time) and then exhibit a stationary state until the end of the pulse, where the domain wall velocity is dramatically reduced (stationary time). The movie in Fig. 5.2.3-1(a) does not include the phase shift images corresponding to the stationary state. In order to show the significantly different spatial evolution occurring during the motion and the stationary states, the phase shift distributions between the two holograms corresponding to the beginning and the end of the motion and stationary states are evaluated and presented in Fig. 5.2.3-2(b)-(c). The bright regions correspond to the total area spanned by the reversed domains and the stationary state clearly exhibits a non significant spatial evolution of the domain walls compared to that observed for the motion state. The stationary state has been observed by other methods [4] and is probably due to lattice defects and/or composition impurities close to the domain walls. These defects generate space-charge regions behaving as pinning points for the propagation of the domain walls on a time scale related to the dielectric relaxation time constant of the material. The domain switching evolution continues in the second, third and fourth SP for which no incubation time is observed while a stationary state occurs for the second and third SP. Moreover the domain switching dynamics in the successive SPs is dominated by the growth and propagation of random shaped reversed domains. The complete domain reversal is obtained before the end of the fourth pulse. Tab.5.2.3-1 presents the time ranges corresponding to the incubation, motion and stationary states evaluated for the four SPs.

	SP1	SP2	SP3	SP4
incubation time (ms)	12	-	-	-
motion time (ms)	33	30	44	25
stationary time (ms)	55	70	55	-
total (ms)	100	100	99	25

Tab. 5.2.3-1: Time ranges evaluated for the domain switching states observed in case of SP poling.

In case of TSP the EFP exhibits an incubation time for the first TSP as in the case of SP. Figure 5.2.3-3 presents the phase shift distribution calculated between the two holograms corresponding to the beginning and the end of the incubation state, showing that non significant domain growth is observed within the resolution limit of the method. Figure 5.2.3-1(b) clearly shows that the reversed domains start growing with a pencil-like shape from the electrode edge corresponding to the lower conductive region of the crystal, as in case of SP. In contrast to SP the dynamics of the reversed domains in case of TSP does not exhibit a stationary state but only a motion state until the end of the voltage waveform for both of the two applied TSPs. This is probably due to the voltage switch on and off on a time scale shorter than the dielectric relaxation time constant. The number of nucleation sites hence increases and the charge redistribution in the crystal occurs before the start of the successive pulse.

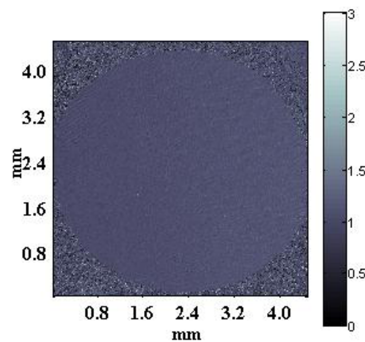

Fig. 5.2.3-3: Phase shift distribution calculated between the two holograms corresponding to the beginning and the end of the incubation state, during the first TSP.

The domain switching evolution continues in the second TSP until the complete polarization reversal in the whole electrode area is achieved. Table 5.2.3-2 presents the time ranges corresponding to the incubation and motion states evaluated for the two TSPs.

	TSP1	TSP2
incubation time (ms)	40	-
stationary time (ms)	-	-
motion time (ms)	80	89
total (ms)	120	89

Tab. 5.2.3-2: Time ranges evaluated for the domain switching states observed during EFP by TSP waveform.

In case of TP the EFP exhibits no incubation or stationary states. The reversed domains start growing at relatively low voltage (around 1.3 kV/mm) with a pencil-like shape in the electrode edge corresponding to the lower conductive regions of the crystal. In correspondence of the peak voltage the pencil-like domains rapidly

propagate towards the opposite edge until the whole electrode area is reversed by exhibiting a spatial evolution more uniform compared to that observed for SP and TSP. The voltage ramping decreases the potential drop in the capacitive surface and space-charge regions thus providing a more uniform electric field distribution in the bulk crystal. This leads to more homogeneous domain nucleation and growth over the electrode area. Table 5.2.3-3 shows the time ranges of the domain switching dynamics corresponding to the low and peak voltage of the TP.

	TP
incubation time (ms)	-
stationary time (ms)	-
motion time – low voltage (ms)	18
motion time – peak voltage (ms)	5
total (ms)	23

Tab. 5.2.3-3: Time ranges evaluated for the domain switching states observed during EFP by TP waveform.

5.2.4 Comparison of domain switching dynamics

Table 5.2.4-1 reports the incubation, stationary and total switching time together with the mean value of the areal domain wall velocity measured for the three different voltage waveforms. The total switching time, when applicable, includes the incubation and stationary times. In case of SP and TSP the contribution of all the applied waveforms is considered.

	SP	TSP	TP
incubation time (ms)	12	40	-
total stationary time (ms)	180	-	-
total switching time (ms)	324	209	23
mean areal velocity (cm^2/s)	0.6	0.9	8.5

Tab. 5.2.4-1: Domain switching parameters measured for the three voltage waveforms for KTP.

The domain switching characterization performed by DH technique demonstrates that more uniform domain switching is obtained by using TP where a redistribution of surface and space charge is observed through the lack of both a stationary and an incubation state. Consequently a more homogenous distribution of the electric field and therefore of the reversed domain nucleation and growth is provided by the TP voltage waveform. On the basis of these results a more uniform periodic poling of KTP crystal samples is expected by using TP voltage waveform.

The *in-situ* method presented here shows that the morphology of the switching domains is clearly different for LN and KTP crystals. A few straight domain walls spanning the electrode area, with isotropic domain wall velocity along the *x* and *y* crystal axis, characterize the EFP of LN. Conversely, the EFP of KTP crystals exhibits the formation and evolution of reversed regions with a typical pencil-like shape and with a strongly anisotropic domain wall velocity along the *x* and *y* crystal axis, the last one being faster. This is probably due to the relatively high and non-uniform ionic conductivity observed in flux-grown KTP crystals. Moreover the domain walls always start growing from the electrode edges in case of LN, while in KTP they start growing basically in the less conductive regions and nucleation can occur also in central regions, far from the electrode edges (see for example Fig. 5.2.3-1(a)). In

case of LN the method reveals the presence of intrinsic localized defects (see for example Fig. 5.2.2-1) which clearly appear to behave as pinning points for the domain wall propagation. Therefore the method is very useful for *in-situ* and non-invasive detection of regions with non-uniform EO behaviour and thus affecting the homogeneity of the EFP in case, for example, of periodic domain patterning. Moreover it is important to note that, even though the phase shift occurring across domain walls in KTP is much lower (~ 0.53 rad) than that occurring in LN, basically due to the one of order of magnitude different coercive field, the technique presented here is able to detect it with acceptable resolution for domain switching characterization.

The *in-situ* technique presented here could be used as a novel tool for real time monitoring of periodic and a-periodic EFP of insulating patterned ferroelectric crystals. The amplitude movies give information about the evolution of the domain walls but are not useful for distinguishing unambiguously the refractive index contrast due to domain wall from that induced by the photoresist edges. DH provides the advantage to reconstruct the phase-map of the object wavefield evolving during the EFP and the phase shift contribution due to the photoresist layer can be numerically eliminated. In this way the domain regions with reversed ferroelectric polarization are unequivocally visualized. Therefore, once the area to be poled is measured, a computer-controlled monitoring technique could be set in order to switch off the input poling voltage when the real-time measured phase shift pattern matches, within acceptable tolerances, the desired *a-priori* known distribution in the frame. As a consequence, the lateral spreading of reversed domains under the insulating layer, which affects the quality of the periodic EFP of LN, could be controlled with high accuracy. Moreover the correspondence between the intensity variations of the flowing current and the spatial evolution of the domain walls could be studied. This monitoring technique could be an alternative to the usual method based on the measurement of the poling current which gives only a good indication of how much area has been poled, without any information about the actual spatial evolution of the reversed domain pattern. Compared to other *in-situ* approaches where the diffraction effect occurring across domain walls is used for direct video observation of the evolving domains [3,4], the technique proposed here provides in focus images of the amplitude and phase distribution of the object wavefield. This allows to improve the lateral resolution, thus providing high fidelity *in-situ* visualization of evolving domain patterns.

5.3 Characterization of internal field in $LiNbO_3$

In this work the IF of congruent LN crystals is investigated by using a DH based method in different measurement conditions. Section 5.3.1 reports the results concerning the evaluation of the static component of the IF, while Section 5.3.2 deals with the measurement of a component of the IF never observed before, the “elastic” component. Section 5.3.3 shows the results of the same kind of measurements performed in off-congruent LN samples, demonstrating the defect dependence of both the static and the elastic component of the IF in LN material.

5.3.1 Evaluation of the static internal field

The method is based on the measurement of the optical path difference (OPD) experienced by a plane wave traversing the sample, along the *z* crystal axis. The

OPD is related to refractive index and/or thickness variations. The measurements are performed on a *z*-cut 0.5 mm thick LN sample with two oppositely oriented ferroelectric domains. This type of structure is widely used for EO beam switching devices [9]. In this kind of application the boundary between the two domain regions should be flat, straight, and free from any residual poling-induced strain. Eventual residual refractive index differences across the domain wall would produce significant Fresnel reflection from this interface thus affecting the switching contrast ratio of the device. This means that any residual refractive index change can be detrimental for the performances of EO and nonlinear optical devices in general.

The sample is positioned into one arm of the MZ set-up shown in Fig. 5.2-1. The laser beam traverses the sample along its *z* crystal axis. The plane reference wave and the object wave, passing through the sample, interfere each other and the corresponding fringe pattern is captured by a CCD camera with (1024×1024) pixel^2 and 6.7 μm pixel size. The digitised hologram is subject to DH numerical procedure in order to reconstruct the object wave front in amplitude and phase. Figure 5.3.1-1 shows the resulting 2D phase shift distribution across the domain wall, where both the in focus reconstructed phase image (lower right) and the defocused twin phase image (upper left) are visible.

The boundary between the two antiparallel ferroelectric domains is clearly visible. The phase distribution is uniform over the areas corresponding to a single domain. The mean value of the phase shift map over the rows of the data array delimited by the white frame in Fig. 5.3.1-1 is calculated. The resulting averaged phase shift profile is shown by the (a) curve in Fig. 5.3.1-2(a) where a phase difference of 1.34 rad across the domain wall is evaluated.

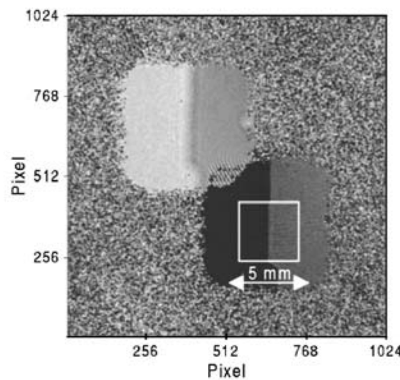

Fig. 5.3.1-1: Phase shift image of the sample with two antiparallel domains.

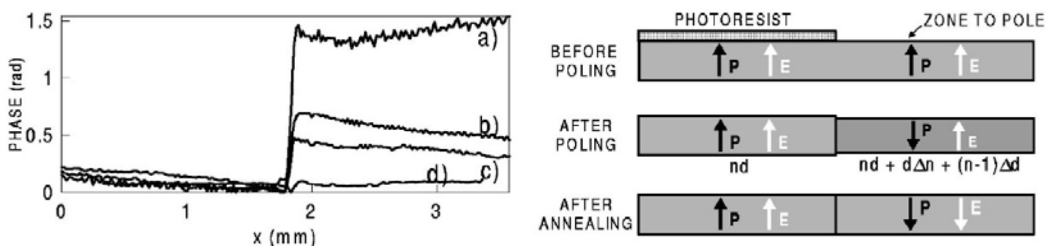

Fig. 5.3.1-2: (left) Averaged phase shift profile (a) before annealing, (b) after 4 h annealing at 240 °C, (c) after second annealing at 240 °C and (d) after 16 months (d); (right) schematic view of the sample cross section in the three different conditions.

The phase step profile is clearly sharp without any diffraction effect from the domain wall because DH allows to reconstruct the image at the plane of the crystal wafer (see Chapter 3). This phase step is attributable to the combination of the EO and PZ effects induced by the IF. In fact, when a reversed domain is generated by EFP and the realignment of the IF E_{int} is not accomplished, an electric field difference $2E_{int}$ appears across the domain boundary. This induces a phase shift $\Delta\phi$ to a plane wave incident along the domain boundary by the EO and PZ effects (see chapter 2):

$$\Delta\phi = (2\pi/\lambda)(d\Delta n_o + (n_o - 1)\Delta d) = (2\pi/\lambda)\left[-dr_{13}n_o^3 + 2d(n_o - 1)d_{33}\right]E_{\text{int}} \qquad (5.3.1\text{-}1)$$

where d is the crystal thickness and Δd the PZ thickness change. According to the Eq.(5.3.1-1) an IF value of E_i=-2.15 kV/mm is obtained by using the measured phase shift value $\Delta\phi$=1.34 rad. The negative sign means that in the reversed region the IF orientation is opposite to that of P_s. A thickness variation of 6 nm across domain boundaries is reported in [10] by using AFM inspection. According to Eq.(5.3.1-1) an electric field of 2.15 kV/mm, applied to a 0.5 mm thick crystal, gives a surface profile of about 8 nm. At room temperature, the realignment process of the IF to P_s orientation is incomplete even after months. In case of the isomorph $LiTaO_3$, when heated above 200 °C, a 95% realignment in less than 30 s is reported [11]. The LN sample is annealed for 4 h at 240 °C and then cooled down at room temperature. The (b) curve in Fig. 5.3.1-2(left) represents the phase shift across the domain wall measured after such annealing treatment. It is clearly reduced respect to the previous one measured just after the EFP, but a residual OPD is still visible. A second annealing treatment has been performed at 240 °C for 5.5 h and curve (c) in Fig. 5.3.1-2(left) shows that a residual phase difference is still visible across the domain boundary. In particular, a 70% realignment of the IF is evaluated. Complete realignment of the IF has been monitored after 16 months and the corresponding phase step appears to be zero, as shown in curve (d). A residual phase peak is still present and probably due to induced birefringence across the boundary.

5.3.2 Evaluation of the elastic component of the internal field

The IF of congruent LN is investigated here in a dynamic regime by studying the EO behaviour in presence of antiparallel ferroelectric domains. The measurements demonstrate the presence of elastic dipole moments related to a component of the IF never observed before. This component is called here elastic, according to the interpretation of the IF reported in [2]. A congruent 0.5 mm thick LN *z*-cut congruent crystal sample is mounted in the plexiglas holder shown in Fig. 4.3-2 and inserted into the RGI set-up as shown in Fig. 4.3-1. An external voltage ramp ranging from 0 kV up to 5 kV, not exceeding the coercive field, is applied across the sample and a measurement of the ratio $\Delta\varphi/\Delta V$, between the phase shift induced by the sample and the external voltage, is performed in five different configurations: (i) virgin; (ii) two antiparallel domains, just after poling; (iii) completely reversed; (iv) back to its original domain orientation; (v) two antiparallel domains after thermal annealing. For each set of measurements, a reference digital hologram h_r is recorded when the sample is inserted in the interferometer and at zero voltage. Afterwards, a sequence of digital holograms h_i (i from 1 to 30) is recorded by the CCD camera (acquisition rate 10 f/s) during the application of the linear voltage ramp. The phase shift experienced by the

object beam with respect to the reference beam, for a uniform virgin sample, is given by

$$\varphi_r = \frac{2\pi}{\lambda}(n_o - 1)d + \Psi_0 \qquad (5.3.2\text{-}1)$$

where λ is the laser wavelength, d is the sample thickness, n_0 is the LN ordinary refractive index, and Ψ is a constant phase induced by the sample holder, the liquid electrolyte, and the interferometer. During the application of the external voltage, the 2D phase shift distribution $\Delta\varphi_i$ occurring for each hologram h_i is due to the EO and PZ effects as described in section 5.2:

$$\begin{aligned}\Delta\varphi_i(x,y) = \varphi_i(x,y) - \varphi_r &= \frac{2\pi}{\lambda}\left[\Delta n_i(x,y)d + (n_o - n_w)\Delta d_i(x,y)\right] = \\ &= \frac{2\pi}{\lambda}\left[-\frac{1}{2}n_o^3 r_{13}(x,y) + (n_o - n_w)d_{33}(x,y)\right]\Delta V_i\end{aligned} \qquad (5.3.2\text{-}2)$$

where $\Delta n_i(x,y)$ is the refractive index change and $\Delta d_i(x,y)$ is the PZ thickness change corresponding to the voltage ΔV_i applied during each hologram h_i. In case of the sample with two adjacent reversed domains, the Eq.(5.3.2-2) has to be changed to describe the different behaviour of the two opposite domain areas, as follows

$$\begin{aligned}\Delta\varphi_{iA,B}(x,y) = \varphi_{iA,B}(x,y) - \varphi_{rA,B} &= \\ &= \pm\frac{2\pi}{\lambda}\left[-\frac{1}{2}n_o^3 r_{13}(x,y) + (n_o - n_w)d_{33}(x,y)\right]_{A,B}\Delta V_i\end{aligned} \qquad (5.3.2\text{-}3)$$

where A is the un-reversed region and B is the reversed one. It is important to note that, as shown in section 5.3.1, the reference phases φ_{rA} and φ_{rB} differ each other after poling because of the presence of the IF and this asymmetry disappears after thermal annealing. The results concerning the measurement of the ratio $\Delta\varphi/\Delta V$ obtained for each configuration are described in the following.

Configuration (i): The 2D phase shift distribution of the virgin sample is retrieved. The resulting EO behaviour is uniform, as expected. The mean values of the phase shift values in two different regions of the virgin sample, named *A* and *B*, are calculated and result to differ each other less than 1%, as shown in Fig. 5.3.2-1.

Configuration (ii): The area *B* is reversed in order to obtain two antiparallel domain areas. The mean value of the phase shift values in the two regions *A* and *B*, versus the applied voltage, is shown in Fig. 5.3.2-2, where the asymmetric behaviour exhibited by the two regions is clearly visible. The presence of this phase difference means that the virgin and the reversed area reply in a different way to the external voltage. A value of $\Delta\varphi/\Delta V=(4.63\pm0.01)\times10^{-4}$ rad/V is measured in the virgin region and a value of $\Delta\varphi/\Delta V=(5.50\pm0.01)\times10^{-4}$ rad/V is evaluated in the reversed area. Hence a relative phase difference of 16% has been measured. Measurements performed using a negative voltage ramp ranging from 0 kV up to 25 kV give comparable results.

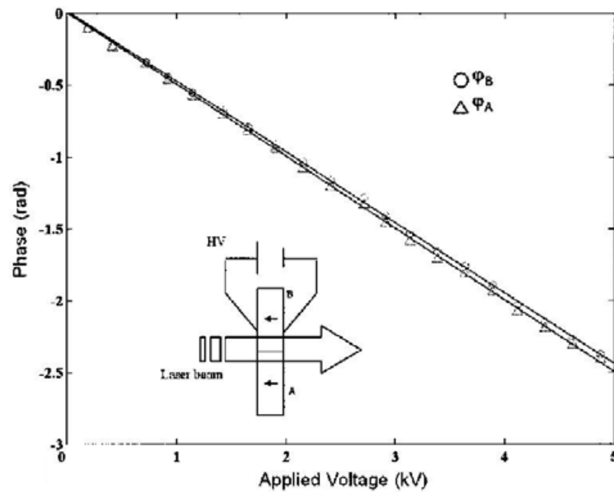

Fig. 5.3.2-1: Phase shift measurement in *A*(Δ) and *B*(O) areas as function of the applied voltage in case of virgin sample. The inset shows a schematic view of the sample with its polarization configuration.

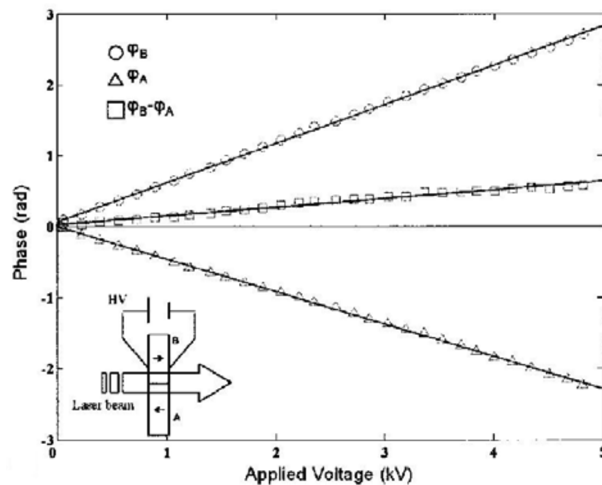

Fig. 5.3.2-2: Phase shift measurement in *A*(Δ) and *B*(O) areas as function of the applied voltage in case of two antiparallel domains, just after poling. The algebraic sum (□) of the two phase shifts is also presented. The inset shows a schematic view of the sample with its polarization configuration.

Configuration (iii): The average phase shift in *A* and *B*, as a function of the external voltage, shows that the EO behaviour of the sample completely reversed is uniform, as expected.
Configuration (iv): Measurements of the phase shift show a uniform behaviour of the sample under the applied field.
Configuration (v): Fig. 5.3.2-3 shows the phase shift measurements in the two antiparallel domain areas *A* and *B*, after thermal annealing, as a function of the applied voltage. The virgin region *A* and the back reversed region *B* clearly exhibit approximately the same EO behaviour. In fact, measurements give $\Delta\varphi/\Delta V=(5.15\pm0.01)\times10^{-4}$ rad/V in region *A* and $\Delta\varphi/\Delta V=(5.23\pm0.01)\times10^{-4}$ rad/V in region *B*, with a relative difference of less than 2%.

In summary, the EO response is uniform over the crystal sample in case of virgin, completely forward reversed and completely back reversed state. Asymmetric EO behaviour is revealed in case of two opposite ferroelectric domains just after the EFP

process, by the measurement of a phase shift with opposite sign and different magnitude in the two reversed regions $\Delta\varphi_{iA} \neq \Delta\varphi_{iB}$. This asymmetry disappears when the sample is thermally annealed (4 h at 500 °C) and thus, according to the results in Section 5.3.1, it is clearly related to the presence of the IF. Since the 2D phase shift distributions $\Delta\varphi_{iA,B}$, corresponding to the voltage ΔV_i, are measured as difference respect to the reference phases $\varphi_{rA,B}$ at zero voltage, which include the contribution of the static component of the IF, the asymmetric EO behaviour is clearly due to a component of the IF never observed before. In fact, according to [2] the IF is not to be considered as a real electric field present in the material but as a formal equivalent of the energetic difference between the two poling states. This energy difference can include not only electrostatic energy differences but also elastic ones, as well due to lattice distortions. Therefore the electrical dipoles associated with defect complexes that give rise to the conventionally known IF in LN $E_{\text{int}}=(E_f - E_r)/2$ have elastic dipole components, too. Consequently, the asymmetric EO behaviour, revealed in this work for two antiparallel domains without annealing, is strictly related to the elastic dipole components that give rise to a previously unknown component of the IF, here called “elastic”.

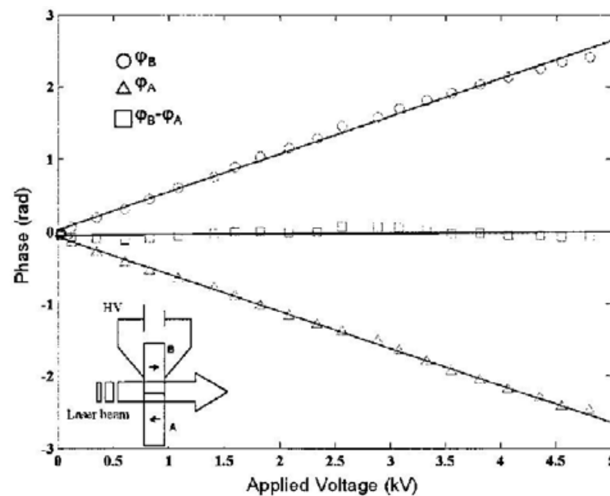

Fig. 5.3.2-3: Phase shift measurement in $A(\Delta)$ and $B(\text{O})$ areas as function of the applied voltage in case of two antiparallel domains, after thermal annealing. The algebraic sum (□) of the two phase shifts is also presented. The inset shows a schematic view of the sample with its polarization configuration.

5.3.3 Evidence of the internal field dependence on crystal defects

A DH based technique is used here to investigate the IF in case of *z*-cut OCLN crystal samples. These samples, (25×25×1) mm^3 sized, are obtained from a boule of OCLN material produced by a Czochralski growth technique (see Chapter 2). As shown by the in-situ technique in section 5.2 the dynamics of the EFP of LN crystals basically consists in the formation of few domain walls in correspondence of the electrode edges and in their propagation over the whole electrode area. Therefore, in order to obtain two antiparallel ferroelectric domains, the OCLN sample is subject to an EFP process by applying the external voltage to the whole virgin crystal sample till the main domain wall reaches the central region of the sample. Figure 5.3.3-1 shows the optical microscope image of a selected part in the un-reversed region under crossed polarizers.

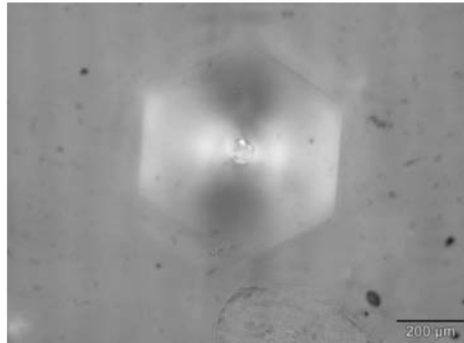

Fig. 5.3.3-1: Optical microscope image, under crossed polarizers, of a selected region in the un-reversed area where a defect surrounded by an hexagonally shaped reversed region is present.

An hexagonally shaped reversed region is clearly formed around a crystal defect about 40 μm large and corresponding to micro-regions with a lattice structure different from the surrounding stoichiometric one. The OCLN crystal sample with two antiparallel domains is inserted in one arm of the MZ interferometer presented in Fig. 5.2-1. The same double-exposure DH technique described in Section 5.3.1 is used here to reconstruct the 2D distribution of the phase shift induced by the sample just after the EFP and without any external voltage. The resulting the phase shift is presented in Fig. 5.3.3-2 while Fig. 5.3.3-3 shows the corresponding surface plot representation. The black line in Fig. 5.3.3-3 indicates the main domain wall across the two adjacent reversed (*B*) and un-reversed (*A*) regions. Figure 5.3.3-2(down) shows the phase shift profile along the dashed line in Fig. 5.3.3-2(up) crossing both the main and the defect surrounding domain wall. In this way a quantitative comparison of the phase shift across the two domain walls is possible. A residual phase shift of about 0.9 rad is clearly localized across the domain boundaries close to the crystal defects, while a null phase shift is detected across the main domain wall (black line), far from the defects. The static IF of the OCLN sample is evaluated by the usual empirical method, based on EFP, as a difference between the voltages required for forward and reverse poling, giving $(E_f - E_r)/2$=675 V/mm.

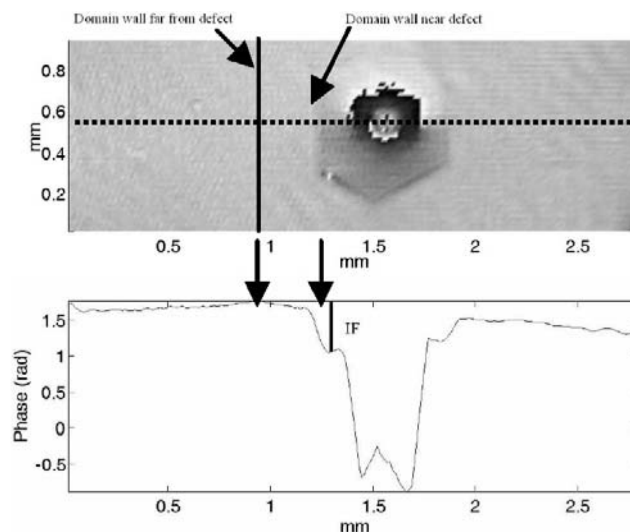

Fig. 5.3.3-2: (Up) Phase shift distribution reconstructed for the virgin region, where an hexagonally shaped reversed area is clearly visible around a defect; (Down) phase shift profile along the dashed line.

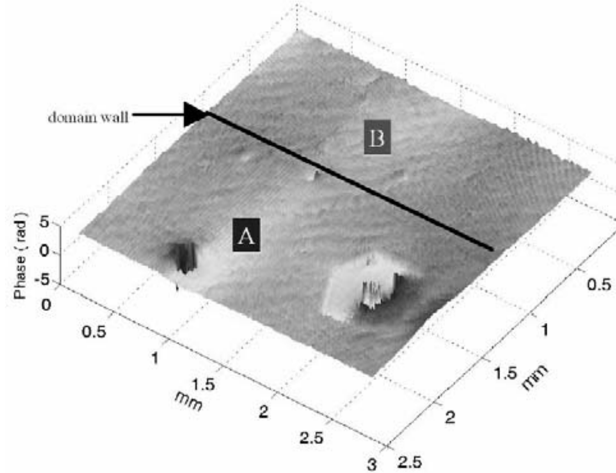

Fig. 5.3.3-3: Surface representation of the reconstructed phase shift distribution of the sample after half poling. The phase shift is clearly homogeneous across the main domain wall (black line), whereas a phase step is visible around the defects.

According to Eq.(5.3.1-1) the measured phase step across the domain wall surrounding the crystal defect is used here to evaluate the magnitude of the corresponding static IF, E_{int}=735 V/mm. This value is in good agreement with that obtained by the EFP method (675 V/mm). The slight discrepancy between the two values can be attributed to the different nature of the measurements. The interferometric technique is more accurate because it provides a spatially resolved map of the IF value over the sample, while the EFP method gives information about the average value of the IF over the whole sample, including both stoichiometric and non-stoichiometric areas. These measurements, performed in OCLN crystals with isolated crystal defects, clearly demonstrate that the static IF is strictly related to the presence of crystal lattice defects. Moreover the phase shift profile in Fig. 5.3.3-2(down) clearly shows a relevant phase difference discontinuity across the defect itself, probably due to the different lattice structure of the defect with respect to the stoichiometric one in which is embedded.

Measurements concerning the EO behaviour are also performed here to investigate the eventual elastic component of the IF across the two kinds of domain wall, by using the method described in Section 5.3.2. A reference digital hologram h_r is recorded with the sample mounted in the plexiglas holder, inserted in the MZ interferometer arm and at zero voltage. Afterwards, a sequence of digital holograms h_i is recorded during the application of a linear voltage ramp ranging from 0 kV up to 2.7 kV (below the coercive field) by using a CCD camera with an acquisition frame rate of about 10 f/s. As in Section 5.3.2 the optical phase shift variation $\Delta\varphi_I$ experienced by the object beam through the sample for each hologram h_i is obtained as difference φ_I-φ_r between the phase map φ_i of the current hologram and that φ_r of the reference hologram h_r, both retrieved by DH. Figure 5.3.3-4(a) shows the surface representation of the 2D phase shift map calculated for one of the h_i holograms recorded during the application of the external ramp voltage.

In this case, both kinds of domain wall (the main one far from the defect and the hexagonal one close to the defect) are clearly visible due to the opposite sign of the EO and PZ coefficients in the oppositely oriented domains (see Section 5.2). The mean values of the phase map, calculated in the two framed regions *A* and *B*, are shown in Fig. 5.3.3-4(b) as a function of the applied voltage. A symmetric response to the applied voltage is revealed for the virgin and reversed regions *A* and *B*

because they are far from defects, similarly to the behaviour of the static IF evaluated previously. Indeed, the optical phase shift values have opposite sign but equal magnitude in the two anti-parallel domain areas. This means that the OCLN sample does not exhibit static nor elastic IF. The EO behaviour across the reversed regions close to the defect is evaluated by improving the spatial resolution in order to spatially resolve the hexagonal region and the results are shown in Fig. 5.3.3-5(a).

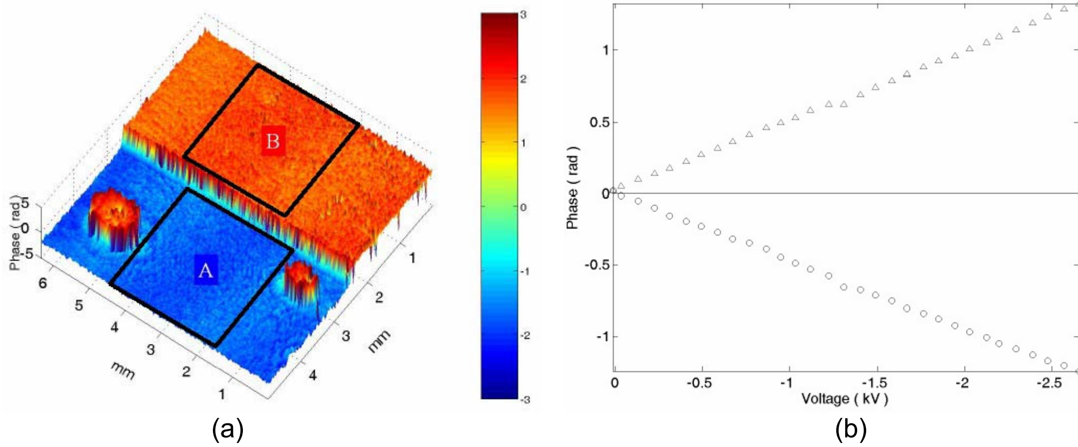

Fig. 5.3.3-4: (a) Surface representation of the phase shift distribution measured when applying an external voltage of 2.7 kV. A phase step is clearly visible across both the main domain wall and the domain boundaries surrounding the defects; (b) averaged phase shift values measured in the virgin *A*(O) and reversed *B*(Δ) areas as function of the applied voltage. The EO behaviour is clearly symmetric.

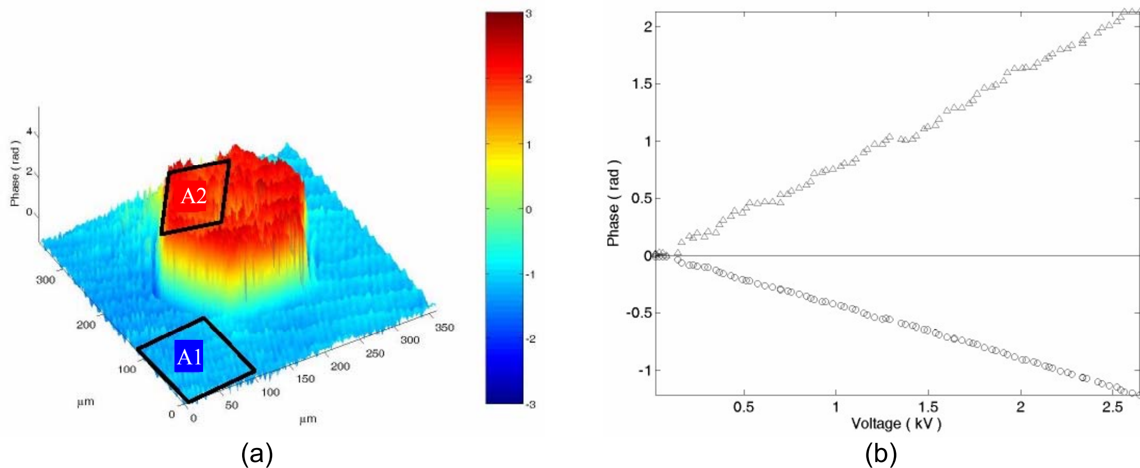

Fig. 5.3.3-5: (a) Magnified surface representation of the phase shift distribution corresponding to the reversed region around the defect; (b) averaged phase shift values measured in *A1*(O) and *A2*(Δ) areas as function of the applied voltage. The asymmetric EO behaviour exhibited by the two regions is clearly visible.

The mean value of the phase maps in the virgin (*A1*) and reversed (*A2*) areas around the defect is reported as a function of the applied voltage in Fig. 5.3.3-5(b), where the asymmetric behaviour exhibited by the two regions is clearly visible. This means that an elastic component of the IF is revealed across the domain wall surrounding the crystal defect.

The results obtained in this section for the OCLN sample, with isolated crystal defects, clearly demonstrate that both the static and the elastic component of the IF are strictly related to the presence of crystal defects.

5.4 Topography characterization of relief structures in $LiNbO_3$

Different relief microstructures are fabricated in LN by EFP and subsequent wet etching (see Chapter 2). The topographic characteristics of these microstructures are investigated here by a DH based method and the advantages of this technique, compared to other conventional approaches, are discussed. The principle of the method relies on the possibility provided by DH to reconstruct the 2D phase shift distribution of the wavefield traversing the object. In case of relief microstructures this phase shift is induced by the OPD experienced by the wavefield when traversing regions with different thickness. Therefore, the topographic features are reconstructed by retrieving the OPD information from the phase shift measurements provided by DH.

The optical set-up, schematically shown in Fig. 5.4-1, is a modified MZ interferometer with a frequency doubled Nd:YAG laser source emitting at λ=532 nm. The light reflected by the sample *S* interferes with a reference plane wave and hologram patterns are recorded by a CCD camera having $(1024\times1280)\text{pixel}^2$ with 6.7 µm pixel size. The reference beam is a plane wave obtained by a beam expander *BE*. The dividing beam-splitter *PBS* is a cube polarizing beam splitter and $\lambda/2$ wave plates are used to control the polarization state and the intensity of the reference and the object beams *R* and *O*. Both the interfering waves are linearly polarized. The polarization state of the object beam is accurately controlled to be close to that of the reference wave in order to optimise the interference between these two beams. The digitally reconstructed phase data are numerically corrected for removing the defocusing phase curvature introduced by the microscope objective *MO* as described in the following section.

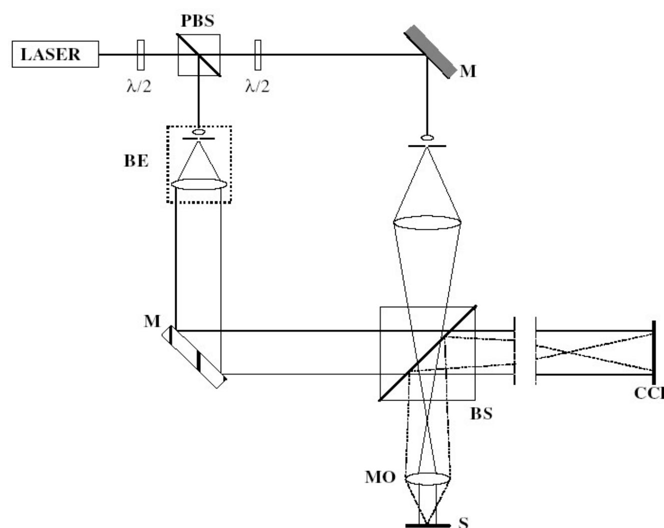

Fig. 5.4-1: Mach–Zehnder interferometer set-up used for recording digital holograms of the micro-structured sample. The laser source emits at λ = 532 nm. *PBS* polarizing beam splitter; *M* mirror; *BE* beam-expander; *BS* beam splitter; *MO* microscope objective; *S* sample.

5.4.1 Principle of the method

The phase distribution of the interference pattern acquired by the CCD camera consists of a parabolic phase factor superimposed to the characteristic phase distribution of the object wave front. The parabolic phase factor accounts for the wave front curvature induced by the imaging lens, the microscope objective. The phase could be numerically corrected by means of a phase factor introduced into the holographic numerical reconstruction process [12, 13]. The method consists basically of three steps: 1) from the acquired hologram the phase correction wave front is calculated; 2) the DH reconstruction of the phase shift at distance *d* is performed for both the hologram and the correction wave front; 3) the two reconstructed phase fields are subtracted at the reconstruction plane at distance *d* for obtaining the contrast phase image of the object with compensation of the inherent curvature. The first step is accomplished by exploiting the mirror-like surface of the LN sample. In fact, it is possible to recognize an area in the recorded hologram which contains only circular fringes because the surface of the LN substrate acts as a plane mirror surface and the fringe pattern is due only to the curvature induced by the microscope objective lens. The remaining area in the hologram contains information about the object under investigation superimposed onto the circular fringes due to the imaging lens. Assuming that the phase calculated for the first area is only due to the wave front curvature introduced by the microscope objective, its distribution can be recovered by performing a non-linear fit of the unwrapped values. The correction wave front phase $\Phi_{corr}(x', y')$ in the CCD plane (x', y') can be written as

$$\Phi_{corr}(x', y') = \frac{2\pi}{\lambda}\left(\frac{x'^2 + y'^2}{2R}\right) \qquad (5.4.1\text{-}1)$$

where *R* is the curvature radius of the correction wave front, i.e. its defocus radius. As described in Chapter 3, DH allows to reconstruct the image of an object by the numerical calculation of the complex wavefield *O(x,y)* transmitted and/or diffused by the object itself. By the same procedure the correction wave front phase $\Phi_{corr}(x', y')$ is propagated at distance *d* so that the correction phase $\phi_{corr}(x, y)$ at the reconstructed image plane can be obtained by the Fresnel propagation of the phase $\Phi_{corr}(x', y')$ at the hologram-recording plane:

$$\begin{aligned} &\exp[i\phi_{corr}(x,y)] \propto \\ &\propto \iint \exp[i\,\Phi_{corr}(x',y')] \exp\left\{\frac{i\pi}{\lambda d}\left(x'^2 + y'^2\right)\right\} \\ &\exp\left\{-\frac{2i\pi}{\lambda d}(x'x + y'y)\right\} dx'dy' \end{aligned} \qquad (5.4.1\text{-}2)$$

where $r(x', y') = 1$. The phase contrast image $\Phi_o(x, y)$ of the object, compensated for the unwanted curvature, can be obtained easily by subtracting the phases of the two reconstructed fields:

$$\Phi_o(x, y) = Arg[o(x, y)] - \phi_{corr}(x, y) \qquad (5.4.1\text{-}3)$$

In the next section the experimental results obtained by this technique are presented for topography reconstruction of LN surface microstructures.

5.4.2 Experimental results

Single domain 0.5 mm thick congruent *z*-cut LN samples are processed in this work. Conventional mask lithography and subsequent EFP (see Chapter 2) is applied here to fabricate PPLN samples with a period of about 30 μm. Subsequent wet etching of 1 hour in a mixture of $HF:HNO_3$=1:2 at room temperature is used to transfer the reversed domain linear grating onto the sample as a surface structure, as shown by the optical microscope image in Fig. 5.4.2-1(a).

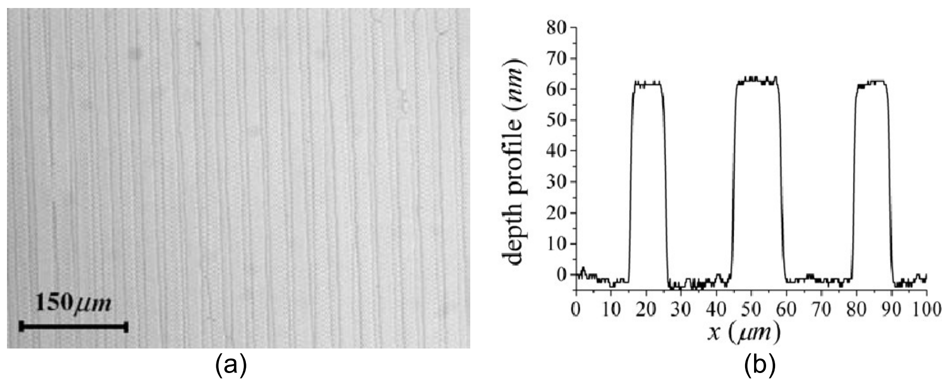

Fig. 5.4.2-1: (a) Optical microscope image of the PPLN sample revealed by an etching process of 1 h in a $HF:HNO_3$ = 1:2 acid mixture at room temperature; (b) the corresponding depth profile measured by a conventional profilometer along the *x* crystal axis.

Figure 5.4.2-1(b) shows the corresponding depth profile measured by a conventional profilometer along the *x* crystal axis. It is important to take into account that the profilometer provides information about the depth profile along a single scanning line without giving full field information about the 3D topography of the structure. However, deep knowledge of the topographic characteristics of the fabricated structures is required before their implementation in a device system. The topographic reconstructions obtained by DH for different LN microstructures are presented in the following. Figure 5.4.2-2(a) shows one digital hologram acquired for the etched PPLN sample described before, as example. Figure 5.4.2-2(b) presents the 2D distribution of the corresponding phase map reconstructed at distance d=100 mm through DH and using the numerical correction procedure described in section 5.4.1. The dimensions of the array data are reduced to include only the data corresponding to the central area of the reconstructed phase map. The linear profile along the white line of the reconstructed phase map is shown in Fig. 5.4.2-2(b) as example. Figure 5.4.2-3 shows the surface representation of the numerically reconstructed phase map and provides a full field topographic image of the fabricated PPLN microstructure. The phase data in Fig. 5.4.2-3 are converted in unit of length by the formula $z = \lambda\phi/4\pi$ on the z axis and by the formula $x = \Delta x/M$ and $y = \Delta y/M$ on the (x,y) axes, where $\Delta x = \Delta y$ is the size of the reconstruction pixel calculated at d=100 mm and M is the magnification of the microscope objective lens.

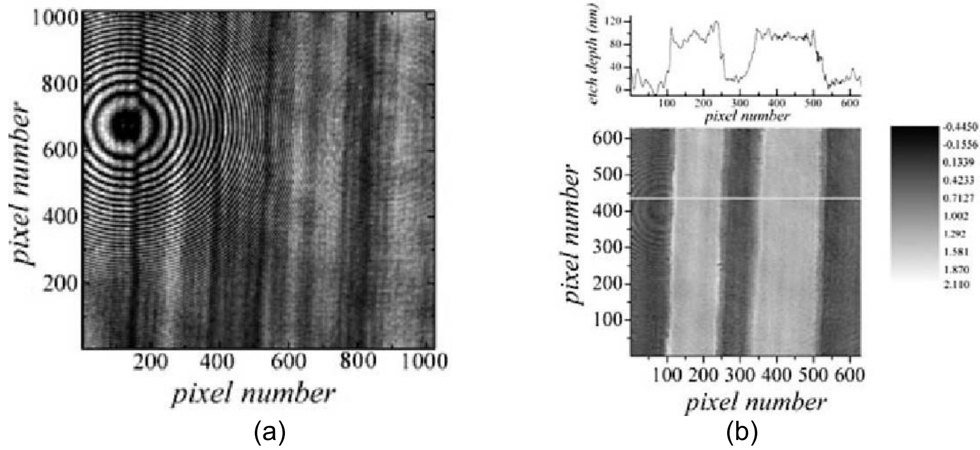

(a) (b)

Fig. 5.4.2-2: (a) Digital hologram acquired for the etched PPLN sample; (b) the corresponding phase shift distribution reconstructed at *d* = 100 mm and phase shift profile along the white line.

The size of the reconstruction pixel is calculated according to Eq.(3.3.3-6). From Fig. 5.4.2-3 a resolution of about 10 nm can be estimated for the surface profile measurement. The reconstructed depth profile shown in Fig. 5.4.2-2(b) can be compared to the profilometer measurement presented in Fig. 5.4.2-1(b), showing that the two techniques are in agreement within 10 nm. The *x* size of the periodic microstructure appears different between the two graphs because the measurements refer to two regions on the sample surface which were etched at the same rate, giving rise to approximately the same etch depth, but exhibiting different lateral size due to a non-uniform duty-cycle of the periodic reversed domain pattern. As a consequence the comparison between Fig. 5.4.2-1(b) and Fig. 5.4.2.-2(b) refers to the measurement of the depth profile and not to that of the lateral dimension.

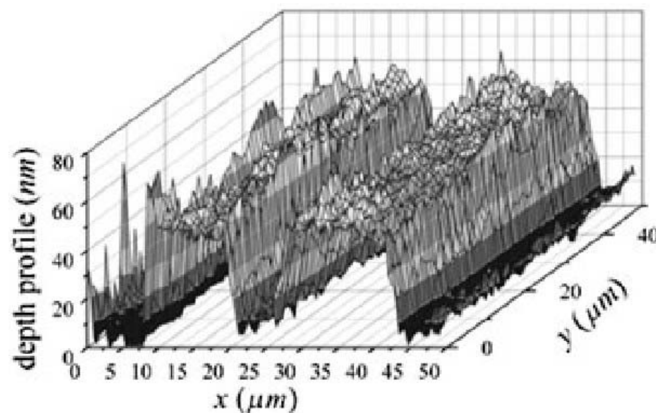

Fig. 5.4.2-3: Topographic reconstruction of the etched PPLN sample obtained from the measured phase shift distribution by converting the data into units of length, as described in the text.

The method was applied to three other types of LN microstructures in order to test the reliability of the technique. Figure 5.4.2-4 presents the SEM and optical microscope images of the LN microstructures investigated in the following.

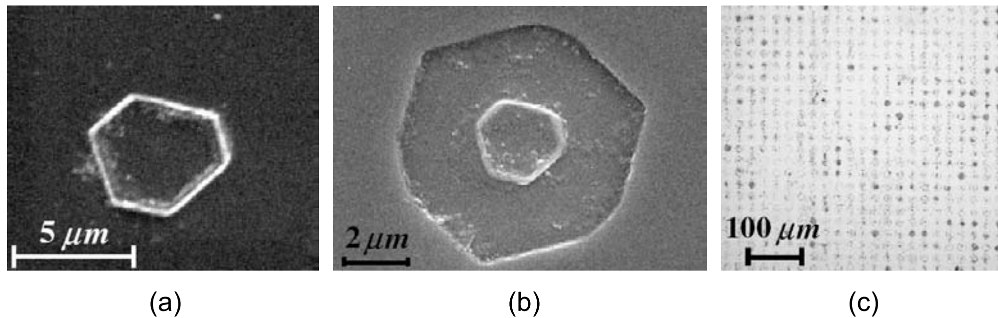

(a) (b) (c)

Fig. 5.4.2-4: (a) SEM image of a typical hexagonally shaped LN microstructure; (b) SEM image of a LN concentric double-hexagon microstructure obtained by spontaneous backswitch poling; (c) optical microscope image of a 2D structure obtained by overpoling (see Chapter 6). All of these microstructures are revealed by a conventional 1 h wet etching in acid mixture at room temperature.

Figure 5.4.2-4(a) shows the SEM image of a typical hexagonally shaped LN microstructure resulting from a spontaneous reverse poling without insulating pattern on the crystal surface, Fig. 5.4.2-4(b) shows the SEM image of a hexagonal concentric microstructure obtained by spontaneous backswitch poling [14] and Fig. 5.4.2-4(c) illustrates the optical microscope image of a 2D structure obtained by overpoling (see Chapter 6). All of these microstructures are revealed by standard wet etching as in case of the previously described PPLN sample. Figure 5.4.2-5(a) shows the reconstructed phase map for the first structure with the corresponding linear phase profiles along the *x* and *y* crystal axes (white crossed lines), showing that the values of the depth profile detected along the two directions are reasonably in agreement. Figure 5.4.2-5(b) depicts the corresponding surface representation of the depth profile where the phase data are converted in unit of length as described before.

It is important to note that the hexagonal microstructure considered here is located in a peripheral region of the LN sample where the structure in Fig. 5.4.2-1(a) was fabricated and that the etching process was applied to the entire sample in order to reveal the domains. This means that, in principle, both structures should have approximately the same etch depth. The holographic measurements are in agreement with this expectation as demonstrated by comparing Fig. 5.4.2-2(b) to Fig. 5.4.2-5(a). Actually the linear profile measured in the case of the hexagonal microstructure appears to be about 40 nm deeper than that measured for the PPLN structure. This is reasonably attributed to a different etching effect occurring on the microstructure edges in case of adjacent reversed domains, as it is for the PPLN structure, compared to that occurring for an isolated reversed domain as in case of the hexagon. This result demonstrates the accuracy of the method in detecting differences of depth profiles in the range of tens of nanometres. Figure 5.4.2-6 and Fig. 5.4.2-7 show the results obtained for the other two microstructures, the concentric double-hexagon and the dot array, respectively.

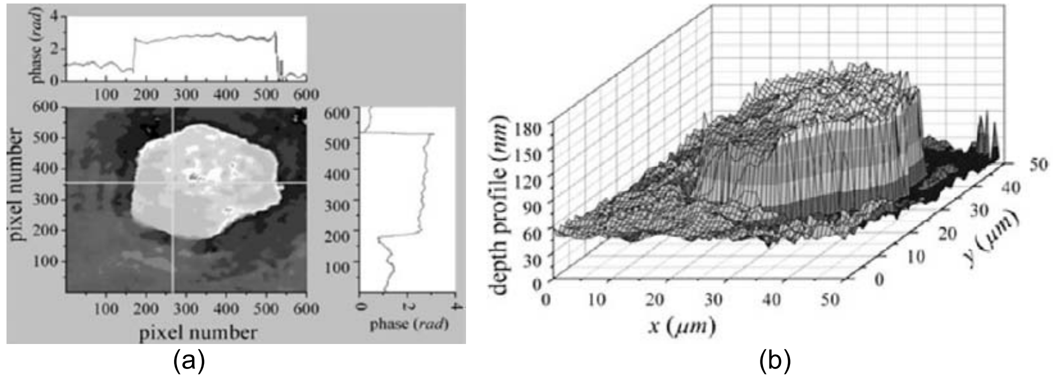

(a) (b)

Fig. 5.4.2-5: (a) Phase shift distribution reconstructed for the hexagonal microstructure and phase shift profiles along the *x* and *y* crystal axes; (b) corresponding topographic reconstruction obtained from the phase map by converting the data into units of length.

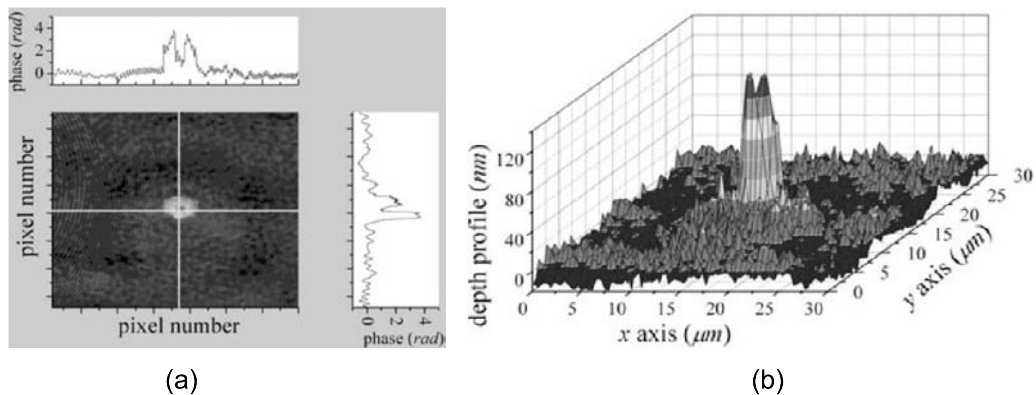

(a) (b)

Fig. 5.4.2-6: (a) Phase shift distribution reconstructed for the double-hexagon microstructure and corresponding phase shift profiles along the *x* and *y* crystal axes; (b) corresponding topographic reconstruction obtained from the phase map by converting the data into units of length.

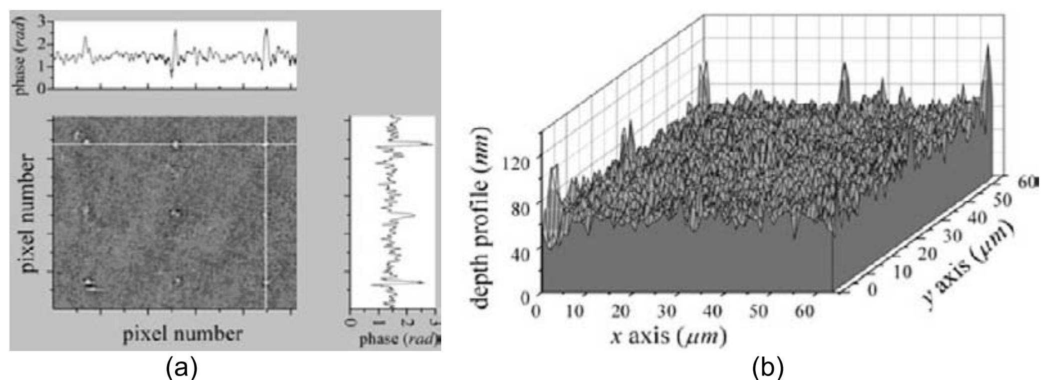

(a) (b)

Fig. 5.4.2-7: (a) Phase shift distribution reconstructed for the dot-array microstructure and corresponding phase shift profiles along the *x* and *y* crystal axes; (b) corresponding topographic reconstruction obtained from the phase map by converting the data into units of length.

It is interesting to note that the technique is able to reconstruct the profile of relatively complicated structures such as the concentric double-hexagon where the depression corresponding to the inner hexagon is clearly visible in Fig. 5.4.2-6(a). It is clear from Fig. 5.4.2-6(a) and Fig. 5.4.2-7(a) that the method allows accurate topographic reconstruction of relatively small structures with a lateral resolution less than 1 μm. This result agrees with the theoretical resolution limit of the microscope objective as calculated according to the Abbe criterion: $0.61\lambda/N.A. \cong 0.6\mu m$.

References Chapter 5

[1] L.H. Peng, Y.C. Fang, Y.C. Lin, Appl. Phys. Lett. 74, 2070(1999).

[2] S. Kim, V. Gopalan, K. Kitamura, Y. Furukawa, J. Appl. Phys. 90, 2949 (2001).

[3] V. Gopalan, T.E. Mitchell, J. Appl. Phys. 85, 2304 (1999).

[4] V. Gopalan, O.X. Jia, T.E. Mitchell, Appl. Phys. Lett. 75, 2482 (1999).

[5] V. Gopalan, M.C. Gupta, Appl. Phys. Lett. 68, 888 (1996).

[6] L.E. Myers, R.C. Eckardt, M.M. Fejer, R.L. Byer, W.R. Bosenberg, J.W. Pierce, J. Opt. Soc. Am. B 12, 2102 (1995).

[7] C. Canalias, J. Hirohashi, V. Pasiskevicius, and F. Laurell, J. Appl. Phys. 97, 124105 (2005).

[8] K. Nakamura, J. Kurz, K. Parameswaran, M. M. Fejer, J. Appl. Phys. 91, 4528 (2002).

[9] G. Coppola, P. Ferraro, M. Iodice, S. De Nicola, S. Grilli, D. Mazzotti, P. De Natale, Opt. Expr. 11, 1212 (2003).

[10] J. Wittborn, C. Canalias, K.V. Rao, R. Clemens, H. Karlsson, F. Laurell, Appl. Phys. Lett. 80, 1622 (2002).

[11] V. Gopalan, T.E. Mitchell, Y. Furukawa, K. Kitamura, Appl. Phys. Lett. 72, 1981 (1998).

[12] E. Cuche, P. Marquet, C. Depeursinge, Appl. Opt. 38, 6994 (1999).

[13] P. Ferraro, S. De Nicola, A. Finizio, G. Coppola, S. Grilli, C. Magro, G. Pierattini, Appl. Opt. 42, 1938 (2003).

[14] R.G. Batchko, V.Y. Shur, M.M. Fejer, R.L. Byer, Appl. Phys. Lett. 75, 1673 (1999).

Chapter 6

Ferroelectric domain engineering for photonic applications

6.1 Introduction

Periodic reversed domain patterns are fabricated in LN by using two novel techniques based on the electric field overpoling (EFO) and on proton exchange (PE) assisted patterning. The EFO allows to fabricate surface domain gratings which, after conventional wet etching in acid mixtures, provide periodic surface structures with lateral size down to a few hundreds of nanometres. The PE exhibits the capability to inhibit the well known (see Section 2) lateral spreading of reversing domains usually occurring in LN during conventional EFP, thus providing relatively homogeneous bulk reversed domain patterns without any constraint about the poling current control. The content of this chapter is described in the following. Section 6.2 describes the holographic lithography (HL) process used to fabricate the short pitch insulating patterns for selective electric field application. Details about the EFO procedure are provided in Section 6.3 while Section 6.4 shows the results obtained in case of periodic nanoscale structuring of LN samples. Moiré effect used in the HL process allows to obtain more complex periodic structures as described in Section 6.5. Section 6.6 illustrates the technique for double-face domain patterning of LN samples and Section 6.7 gives information about the possible applications of the fabricated structures in the field of photonics. Section 6.8 reports the results demonstrating the possibility to use the proton exchange process in order to inhibit the lateral spreading of reversing domains in periodic EFP of LN.

6.2 Holographic lithography

HL is carried out by combining two coherent wavefields to form a sinusoidal intensity light pattern in space. The interferogram is generated within the volume of space defined by the overlapping beams. Since HL does not need any photolithographic mask, the field size depends only on that of the two beams, whereas in conventional lithography the imaging system generally limits the workable field size. A simple 1D grating can be obtained by exposing a layer of photoresist to the interference pattern. Furthermore, more complex 2D patterns, including square or hexagonal arrays of dots or holes, can be obtained by overlaying multiple exposures or combining more than two beams. HL has some unique advantages over conventional optical lithography. In particular, the spatial resolution of HL can easily exceed the resolution limits of today's optical steppers when comparable wavelengths are used. For example, structures as small as 100 nm are readily patterned by HL using a source at 351 nm [1,2] with the additional advantage of a faster process, if compared to Electron Beam Lithography, especially when large exposed areas are required. Compared to mask optical lithography, HL is not diffraction limited and the depth of focus is effectively infinite on the scale of planar devices. This makes HL well suited for applications where substrate flatness and topography are critical issues. One more attractive feature of HL is its implementation with relatively simple optical

components so that effects due to lens aberrations are dramatically reduced compared to the case of conventional lithography.

Three different set-ups have been used here to generate the interference pattern: Michelson (*M*); two-beams (*TB*); Loyd's mirror (*LM*). Figure 6.2-1 shows the schematic views of these interferometric configurations. The period of the fringe pattern depends on the overlapping angle 2θ between the two interfering beams according to the formula $p=\lambda/2\sin\theta$. The source used for these interferometers is a coherent He-Cd laser delivering a power of about 65 mW at 441.6 nm. Different fringe periods and exposed areas are provided by these interferometers, depending on the overlapping geometry of the two interfering wavefields. The *M* set-up provides an interferogram covering a circular region of about 25 mm in diameter with a fringe period ranging from the zero fringe condition down to about 15 μm. Shorter periods are not obtainable because in this configuration the two beams are almost parallel and large interference angles are not possible.

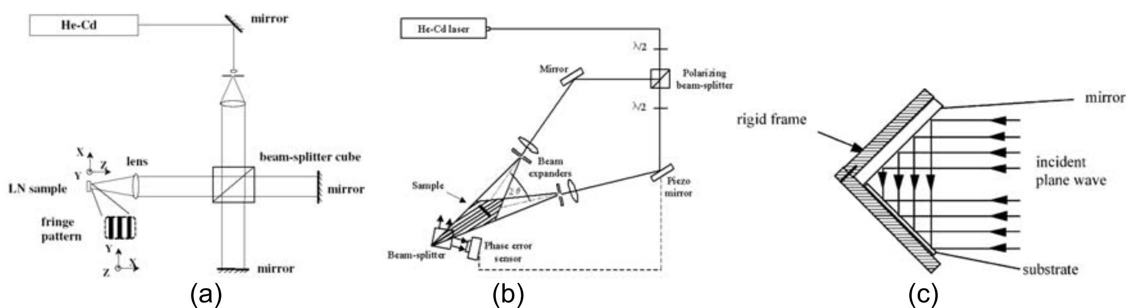

Fig. 6.2-1: Interferometric set-ups used for HL process: (a) Michelson type used for periods down to about 15 μm; (b) two-beams type used for periods down to the diffraction limit (about 220 nm) over relatively large areas (about 2 cm diameter); (c) Lloyd's mirror type used for periods down to about 220 nm over relatively small areas (about 5 mm large).

The *TB* set-up used in this work is suitable for shorter periods ranging from about 2 μm down to about 220 nm (λ/2 diffraction limit). Larger periods would be possible at narrower angles and thus at longer distances from the dividing beam-splitter. The *LM* set-up allows to produce relatively short fringe periods like in case of the *TB* interferometer. In this case the coherence of the fringe gratings depends dramatically on the quality of the mirror. Dust particles on the mirror and any sharp edges give rise to scattered radiation which contributes to a coherent noise. The *LM* configuration is hence simple and low cost, but does not produce the highest quality gratings and grids.

6.3 Sub-micron reversed domains by electric field overpoling

EFPO is applied here to LN samples patterned on *z+* face with 1D and 2D resist gratings obtained by the *M* set-up. The technique allows to generate sub-micron reversed domains otherwise difficult to achieve by conventional EFP (see Chapter 2). The overpoling regime is achieved by applying the external voltage till the poling current drops to zero, thus ignoring both the total amount of charge delivered to the sample and the usual crucial stopping criterion (see Chapter 2). Therefore, the technique is easier to accomplish in respect to the conventional EFP but also in

respect to other overpoling approaches [4] where particular amounts of empirical overcharge have to be considered. The external voltage is applied at room temperature by using the plexiglas holder and the external electrical circuit shown in Fig. 4.3-2. The samples are insulating patterned on *z*+ face by the *M* set-up with 1D and 2D gratings and a positive high voltage pulse, slightly exceeding the coercive field of LN (21 kV/mm), is applied to the *z*+ face. The series resistor is R_s=50 MΩ. The following sections show the results obtained for both 1D and 2D resist gratings.

6.3.1 Overpoling regime applied to 1D gratings

EFO is applied to LN crystal samples patterned with a 1D resist grating at 30 μm period obtained by the *M* set-up. The process is about 3 s long and the resulting ferroelectric domain pattern, revealed by a wet etching process of 60 minutes in $HF:HNO_3$=1:2 acid mixture, is shown in Fig. 6.3.1-1(a).

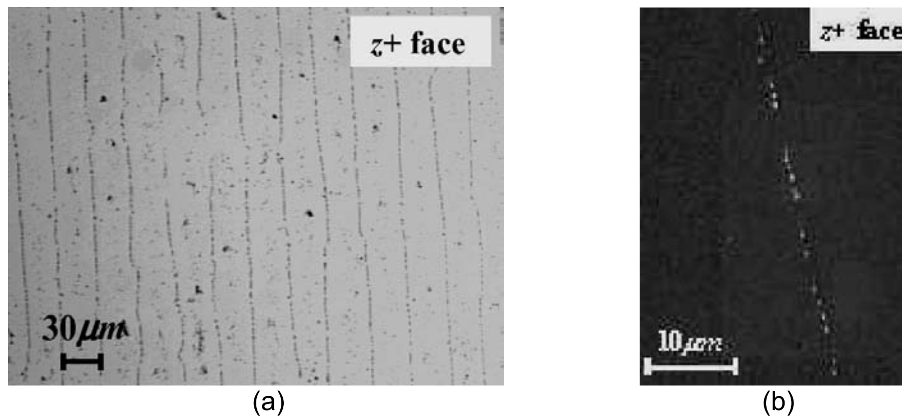

(a) (b)

Fig. 6.3.1-1: (a) Optical microscope image of the aligned dot domains revealed by wet etching; (b) SEM image of the dot structures.

Aligned dot-like structures with sub-micron size are visible, corresponding to unreversed regions under the photoresist strips. This effect is due to an incomplete merging of the adjacent reversed domains under the photoresist. The isolated dots aligned along the photoresist fringes correspond to the regions excluded by the merging of the hexagonal-type counter propagating domain walls, originating from two adjacent electrodes during poling and joining under the resist strips. The propagating domain walls are probably not straight because the sidewalls of the resist strips are affected by relatively high corrugation and low steepness. In fact, interference fringes with pitch values over the micron scale present quite large speckles such that the propagating domain walls find ways along which the velocity of motion varies. Consequently, the merging is not successful everywhere. The optical microscope image taken in a peripheral region of the pattern and presented in Fig. 6.3.1-2 clearly supports this interpretation. It illustrates the domain merging occurring in different regions of the pattern such that the merging process is frozen in the various stages of its evolution. Figure 6.3.1-3 shows a representative frame of the schematic movie presenting the evolution of reversing domains during the EFO.

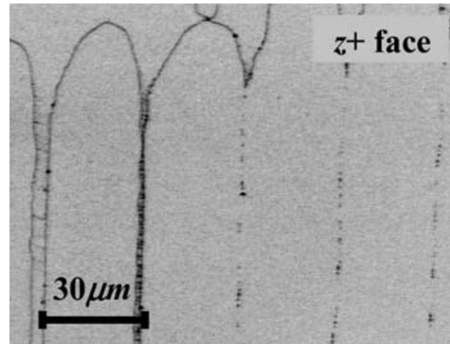

Fig. 6.3.1-2: Optical microscope image of the dot-like domains in a peripheral region of the pattern.

These images show how the mechanism of merging of adjacent domains leads to the formation of the aligned dot-like domains under the resist strips.

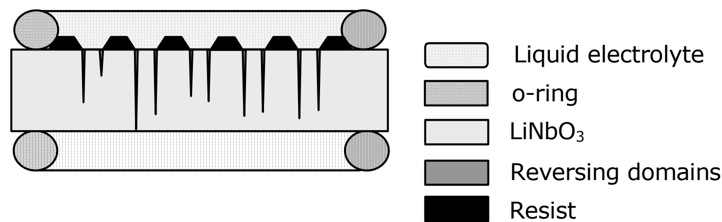

Fig. 6.3.1-3: Representative frame of the schematic movie showing the evolution of reversing domains under EFO. (see Paper XI)

Microscope inspection of the etched sample reveals that opposite crystal faces exhibit different structure morphologies, as shown by the magnified optical microscope images in Fig. 6.3.1-4. A line-shape structure on *z*- face corresponds to a dot-shape on the *z*+. One of the interesting features of these dot-like domains is the sub-micron size, as shown by the SEM image in Fig. 6.3.1-1(b). In fact, despite the advantages achieved nowadays by the conventional EFP, such as repeatability, scalability and applicability over a wide range of materials, fabrication of periodically poled materials with arbitrarily small values of period, particularly at sub-micron scales, remains an elusive goal.

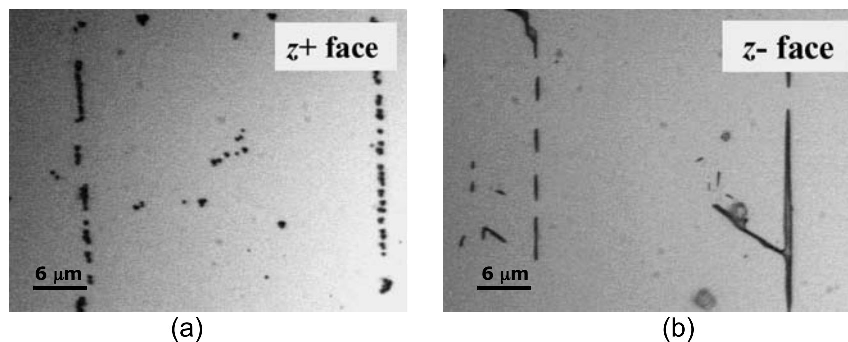

Fig. 6.3.1-4: (a) Magnified optical microscope image of the dot-like domains on *z*+ and (b) the corresponding line-like structure on *z*-.

The EFO technique presented here can be considered as an effective and relatively simple solution for achieving high density and sub-micron ferroelectric reversed domain structures. However, the ferroelectric domain pattern presented in this

section clearly needs higher homogeneity and repeatability in order to be used for photonic applications. In fact, the lines along which the dot-like domains are aligned are equally spaced at about 30 μm, as expected (see Fig. 6.3.1-1(a)), but the dot-like regions are not equally spaced along the single line (see Fig. 6.3.1-1(b)). This is basically due to the lack of control of the domain merging according to a regular geometry. One method which allows to overcome such problem consists in patterning the sample with a 2D array of insulating dots so that during the EFO the reversed domains are constrained to merge under the isolated photoresist structures equally spaced along both *x* and *y* direction. The results obtained by this technique are presented and discussed in the next section.

6.3.2 Overpoling regime applied to 2D gratings

The EFO technique is applied here to a LN crystal sample patterned with a 2D resist grating obtained by two 90° crossed exposures by the *M* set-up. The resulting grating on *z*+ face consists in a square array of photoresist dots with a period of about 23 μm along both the *x* and *y* crystal axis direction, as shown by the optical microscope image in Fig. 6.3.2-1(a). Figure 6.3.2-2 shows the typical current and voltage waveforms acquired during the EFO process. The poling process was about 3.5 s long. Figure 6.3.2-1(b) shows the optical microscope image of the resulting square array of dot-like domains revealed by 30 minutes wet etching at room temperature. The 2D geometry of the resist grating has clearly improved the period regularity of the dot-like domains along the *y* crystal axis direction. In fact, these dot-like domains are equally spaced by about 20 μm along both the *x* and *y* direction, in agreement with the pitch size of the resist grating.

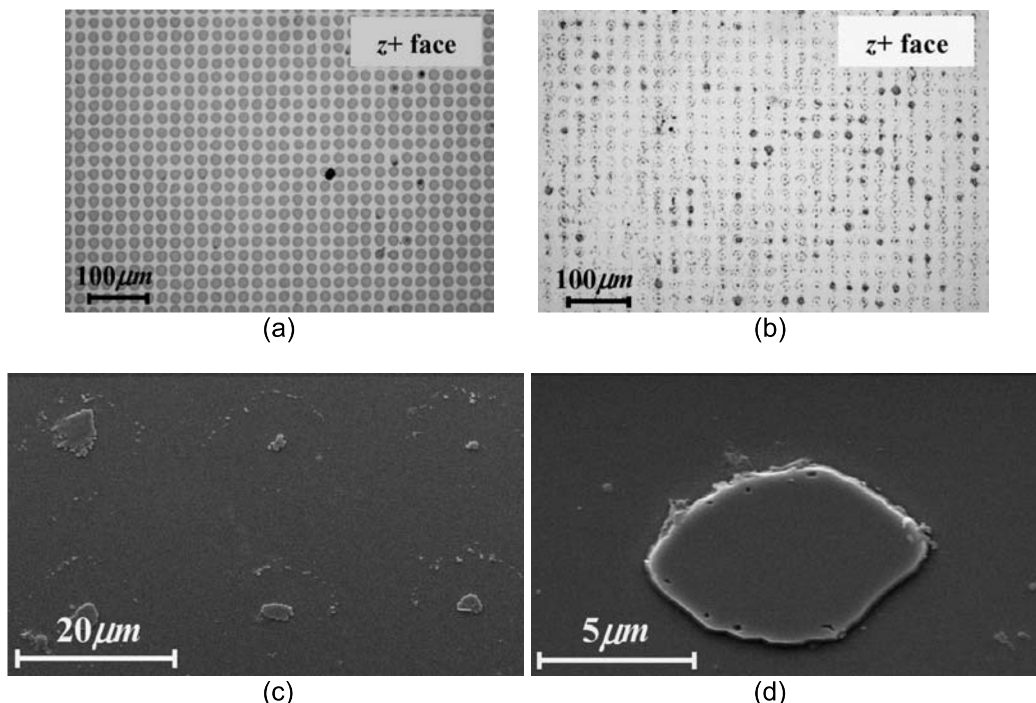

(a) (b)

(c) (d)

Fig. 6.3.2-1: (a) Optical microscope image of the square array of resist dots; (b) optical microscope image of the corresponding dot-like domains after wet etching; (c)-(d) two different SEM magnified views of the dot-like domains.

As explained in the previous Section, the dot-like structures correspond to the regions left unreversed after the domain spreading under the resist dots.

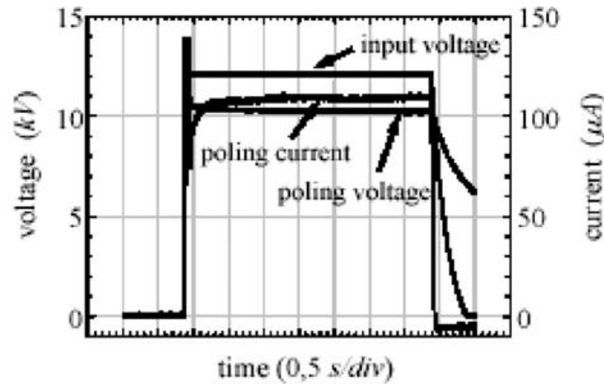

Fig. 6.3.2-2: Waveforms of the poling current, poling voltage and input voltage acquired by the oscilloscope during the EFO of a LN sample patterned by the square array of resist dots at 23 μm period. The EFO process took about 3.5 s.

The SEM image in Fig. 6.3.2-1(c) shows that each dot-like domain is surrounded by smaller dot structures similar in nature to those obtained in case of 1D resist pattern (see Fig. 6.3.1-1(a)) and forming a circle-like structure. The etching process reveals that the surrounding dots have the same polarization direction as the central ones. This means that the domain spreading under the resist dots evolves leaving such smaller dot-like regions unreversed. In other words, the central dots correspond to the regions not reached at all by the domain spreading, whereas the surrounding ones result from non-homogeneous advancing of the domain wall towards the central part of the resist dots. The diameter of the circle-like structures is everywhere smaller than that of the printed resist dots by about 2 μm. This means that they originate under the resist dots but not in correspondence of their edges. A quantitative characterization of these surrounding dots is carried out by comparing the mean value of the ratio *p/d* estimated for the resist array (Fig. 6.3.2-1(a)) and for the etched domain structure (Fig. 6.3.2-1(b)), *p* being the pitch of the periodic structure and *d* the diameter of the resist dots and of the circle-like structures, respectively. The measurements give 1.6 in case of the resist array and 1.9 in the other. This confirms the geometrical non correspondence between the surrounding dots and the resist edges. Moreover, the z- face of the sample in Fig. 6.3.2-1(b) is perfectly flat, meaning that any structure is revealed by the etching process and thus a surface reversed domain structure has been obtained. Therefore the EFO clearly evolves from the *z-* to the *z+* face leaving shallow dot-like unreversed domains under the resist dots, as shown by the schematic cross section view in Fig. 6.3.2-3.

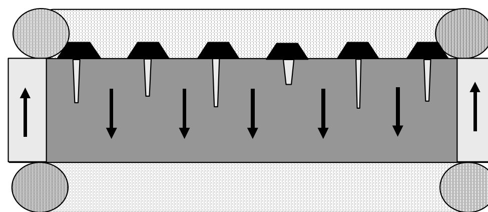

Fig. 6.3.2-3: Schematic cross section view of the unreversed domains (white regions) formed under the resist dots after EFO of 2D HL patterned LN samples.

6.4 Periodic nanoscale surface structuring by electric field overpoling

The first fabrication and accurate characterization of periodic 1D and 2D surface structures in LN with feature sizes and periods down to 200 nm and 530 nm, respectively, is reported here. The fabrication consists in periodic EFO and subsequent selective etching in HF solution. Conventional photolithography techniques are not suitable for patterning periods much below 1 μm so that short period insulating gratings are fabricated over relatively large areas by HL. AFM is used to characterize the fabricated surface structures.

Both sides polished congruent LN samples are resist patterned on *z-* face by single or double exposure HL to get 1D and 2D resist arrays with periods ranging from 2 μm down to about 500 nm. The resist patterned samples are subject to room temperature EFO which enables the fabrication of surface reversed domain patterns on *z-* crystal face. After poling, the resist pattern is removed and the samples are etched in HF solution at room temperature in order to reveal the domain pattern. The etching is selective and targets the surface of *z-* domains thus generating a surface periodic structure while *z+* domains remain essentially intact (see Chapter 2). An AFM is used to investigate the engineered surface structures. The sample alignment, the measurement process and the data storage are easily controlled by software. The measurements are performed in contact mode by scanning silicon probes over volumes up to (200×200×20) μm^3. Topography images (256×256) $pixel^2$ sized are recorded and WSxM® software is used for measuring the main interesting features sizes of the samples.

Four samples with different kinds of topography and periods are investigated here. The samples *A* and *B* have 2D periodic structure consisting of a square array of pillar-like structures (PLS) and hole-like structures (HLS), respectively, with 2 μm period; the sample *C* has a 2D periodic structure consisting of a square array of HLS with 530 nm period; the sample *D* has a 1D periodic structure with 600 nm period. All of these samples are first domain reversed by EFO and then etched in HF solution at room temperature for 5 minutes. The PLS or the HLS are obtained by applying the EFO to samples resist patterned with a grid-like geometry (GLG) or a dot-like geometry (DLG), respectively. In fact, the overpoling process allows to reverse the ferroelectric polarization everywhere in the bulk crystal apart from shallow unreversed regions under the photoresist layer which faithfully reproduce the resist pattern geometry. Figure 6.4-1(a) shows the optical microscope image of the *z-* face of sample *A*, after etching, and that of the corresponding GLG resist pattern as example (see the inset).

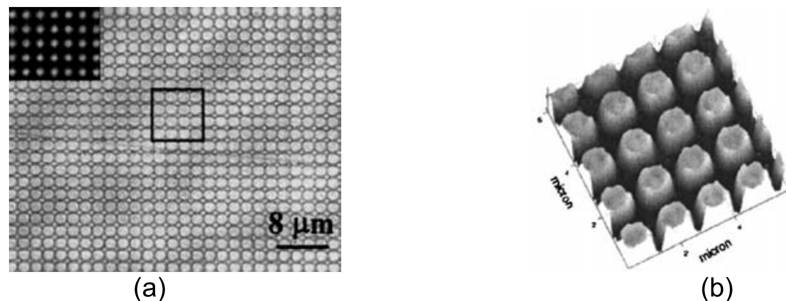

Fig. 6.4-1: (a) Optical microscope image of sample *A* and (b) corresponding surface representation of the region in the square frame. The inset shows the optical microscope image of the corresponding photoresist grid-like geometry.

The PLS, surrounded by canyon-like structures, obtained in sample *A* is clearly visible in the surface representation image in Fig. 6.4-1(b), corresponding to the region highlighted by the square frame in Fig. 6.4-1(a). The AFM topography image taken on the *z*- face of the sample *B* is presented in Fig. 6.4-2(a). The HLS obtained in sample B is clearly visible in the surface view shown in Fig. 6.4-2(b).

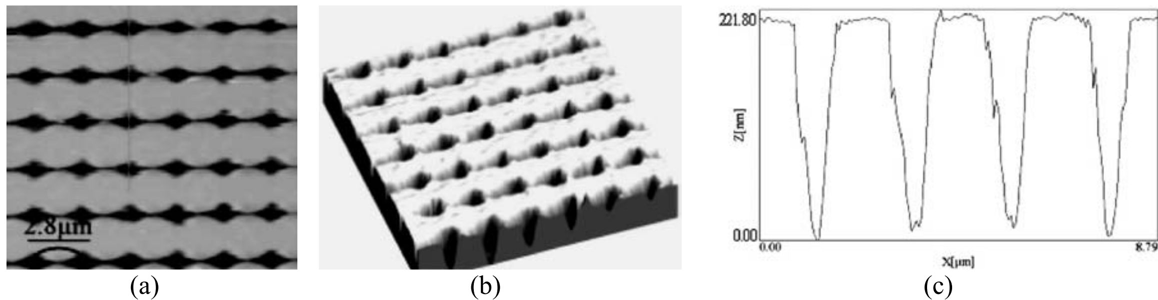

Fig. 6.4-2: (a) AFM topography image of sample B; (b) corresponding 3D representation; (c) depth profile along the line indicated in (a).

The etch depth profile is around 220 nm as shown by the AFM profile measurement in Fig. 6.4-2(c). Figure 6.4-3(a) shows the AFM topography image taken on *z*- face of sample *C* which has been overpoled by using the DLG resist pattern shown in the inset as example. A magnified view of the structure is presented in Fig. 6.4-3(b) while the surface view is shown in Fig. 6.4-3(c). The etch depth is around 1 μm as shown by the AFM profile measurement in Fig. 6.4-3(d). Figure 6.4-4(a),(b) show the AFM topography image and the corresponding profile measurement taken on the z- face of sample *D*. The etch depth is around 200 nm.

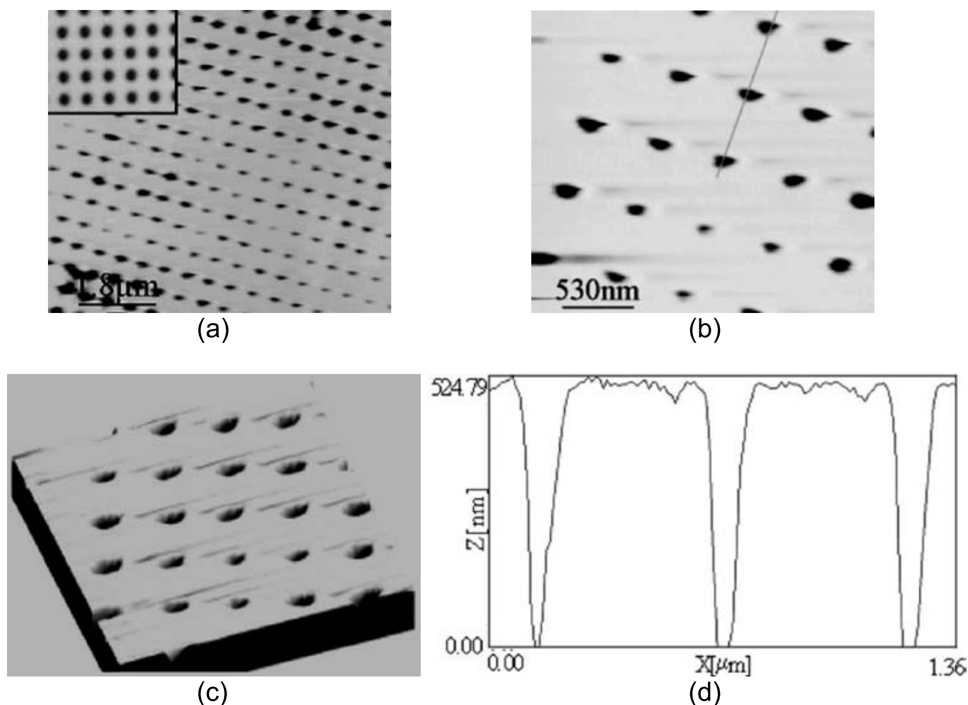

Fig. 6.4-3: (a) AFM topography image of sample *C;* (b) magnified topography view; (c) corresponding 3D image; (d) depth profile along the line indicated in (b). The inset shows the optical microscope image of the corresponding dot-like geometry resist pattern.

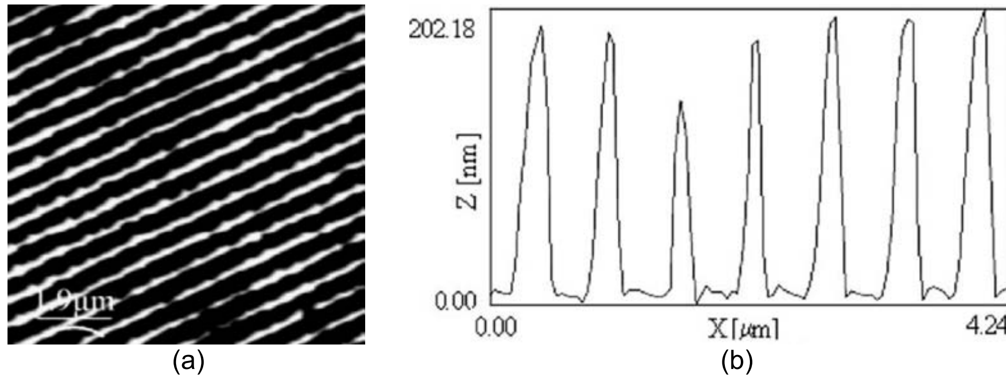

Fig. 6.4-4: (a) AFM topography image of sample *D*; (b) corresponding depth profile along a line perpendicular to the domain direction.

In Tab. 6.4-1 the main measurement results obtained for the samples investigated here are summarized.

	Structure type	Period (nm)	Feature size (nm)	Etch depth (nm)	Area (mm × mm)
Sample *A*	PLS	2000	1500	1000	(4 × 4)
Sample *B*	HLS	2000	900	220	(2 × 2)
Sample *C*	HLS	530	200	530	(2 × 2)
Sample *D*	lines	600	300	200	(1 × 1)

Tab. 6.4-1: List of the main measurements obtained for each sample. In case of PLS the etch depth refers to the surrounding canyon-like structures.

In conclusion, both 1D and 2D periodic surface structures with feature sizes down to 200 nm have been presented here for the first time in a ferroelectric material. Such structures could find applications in the field of nonlinear optics for short-wavelength conversion processes, as well as in the field of photonic band-gap or Bragg grating devices.

6.5 Complex surface structures by moiré HL

Moiré effect [5] is used here in the HL process by the TB set-up (see Section 6.2) to fabricate periodic resist gratings with complex geometries to be transferred into 500 μm thick LN substrates as surface structures by EFO and subsequent wet etching. In particular, three kinds of structures are produced corresponding to three different beating geometries.

Sample *M1* is resist coated on *z*- face and HL patterned with 2 μm period 2D square grating by 90° crossed exposures. Afterwards, *z*+ face is coated and HL patterned by the same 2D pattern. Figure 6.5-1(a) shows the typical square array resist grating obtained on the *z*+ face, after patterning *z*- face. The fringe period is slightly changed before exposing *z*+ face, resulting in a typical moiré fringe pattern obtained on the *z*- face (see Fig. 6.5-1(c)). In fact, since the *z*- face is patterned first,

that effect is due to the residual resist photosensitivity on the *z-* face, during the exposure of *z+*.

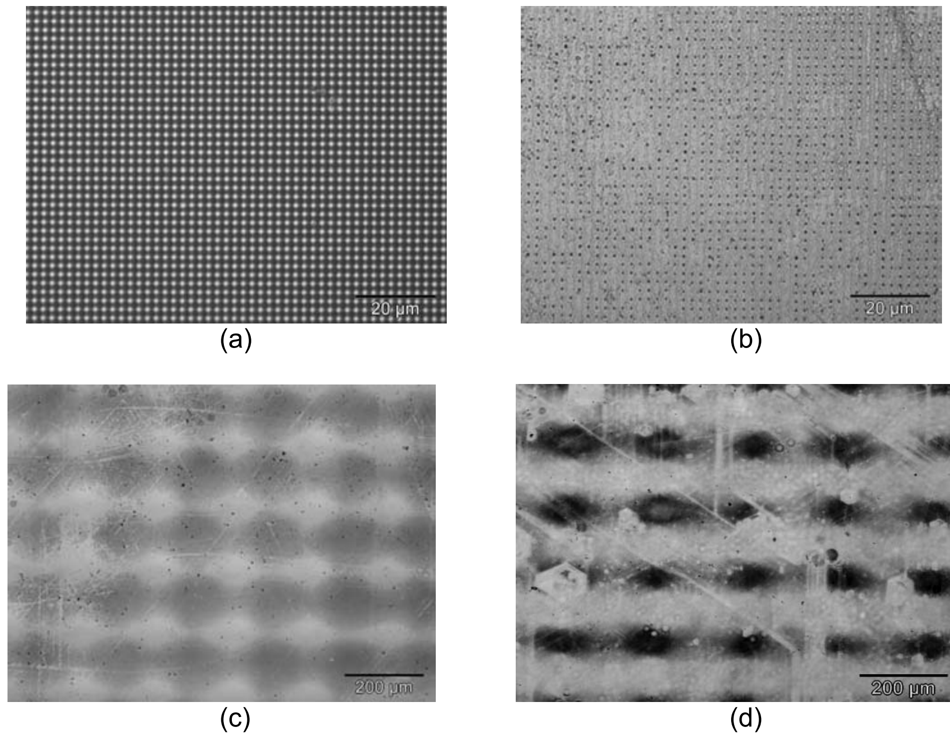

Fig. 6.5-1: Optical microscope image of (a) the resist grating printed on the *z+* face of sample *M1*; (b) the corresponding surface structure on *z+* after poling and etching; (c) the resist grating printed on the *z-* face; (d) the corresponding surface structure on *z-*.

The interference fringes, transmitted by the resist on *z+* face and by the crystal itself, overlap with the resist pattern previously printed on the *z-* face, causing the well known moiré effect [5]. If necessary, this effect can be easily avoided by postbaking the sample after the z- face is developed and before the z+ face is spin-coated. The moiré effect produces on *z-* face a double period resist grating with periods 2 μm and 200 μm (see Fig. 6.5-1(c)). The sample is then subject to EFO and Fig. 6.5-1(b),(d) show the reversed domain pattern revealed by HF etching on *z+* and *z-* face, respectively. Referring to the wide field image in Fig. 6.5-1(d) a magnified optical microscope image is acquired in a dark region (see Fig. 6.5-2(a)), and a SEM image is taken in one of the bright regions (see Fig. 6.5-2(b)). The SEM image clearly shows that periodic hole-like structures around 200 nm sized have been obtained.

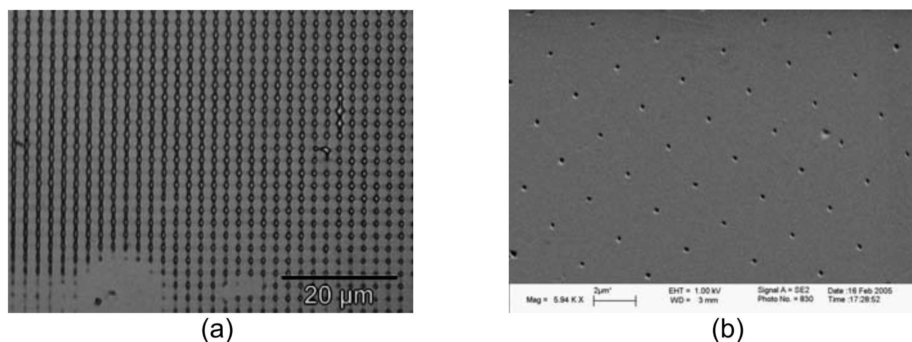

Fig. 6.5-2: (a) Magnified optical microscope image of sample *M1* in correspondence of the regions appearing dark in wide field optical microscope image; (b) SEM image of the bright regions.

Sample *M2* is resist coated on *z*- face and subject to four HL exposures: two 90° crossed exposures at 2.4 μm period and two 90° crossed exposures at 2.5 μm period. A unique development process is performed after the four exposures. A 2D double period (2.4 μm and 2.5 μm) resist grating is obtained on *z*- face as result of the moiré beating between the two fringe gratings, as shown by the optical microscope image in Fig. 6.5-3(a). Subsequent EFO and HF etching allows to transfer such resist geometry into the LN substrate as surface structure shown by the optical microscope image in Fig. 6.5-3(b).

Sample *M3* is resist coated on z- face and subject to three HL exposures: two crossed exposures at 2.4 μm period and one at 2.4 μm period. A unique development process is performed here too, after the four exposures. A 2D grating at 2.4 μm with 1D channels at 2.5 μm period is obtained as shown by the optical microscope image in Fig. 6.5-4(a). The surface structure obtained on z- face by EFO and subsequent HF etching is shown by the optical microscope image in Fig. 6.5-4(b). The 1D channels are periodic with 80 μm period.

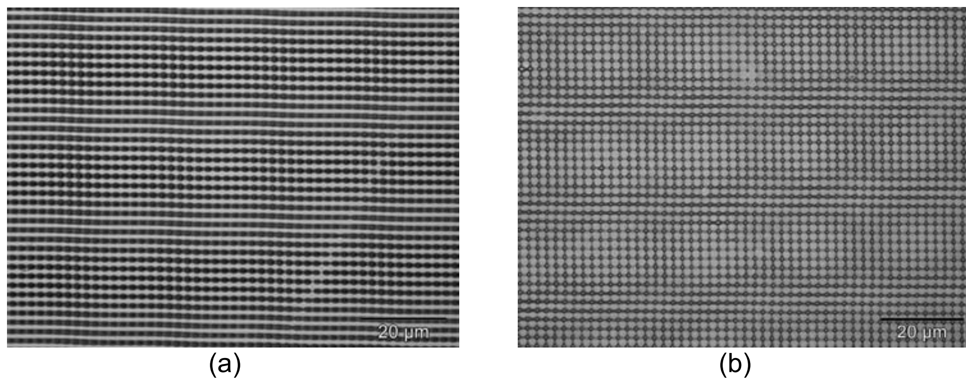

(a) (b)

Fig. 6.5-3: Optical microscope image of (a) the resist grating printed on the *z*- of sample *M2*; (b) the corresponding surface structure.

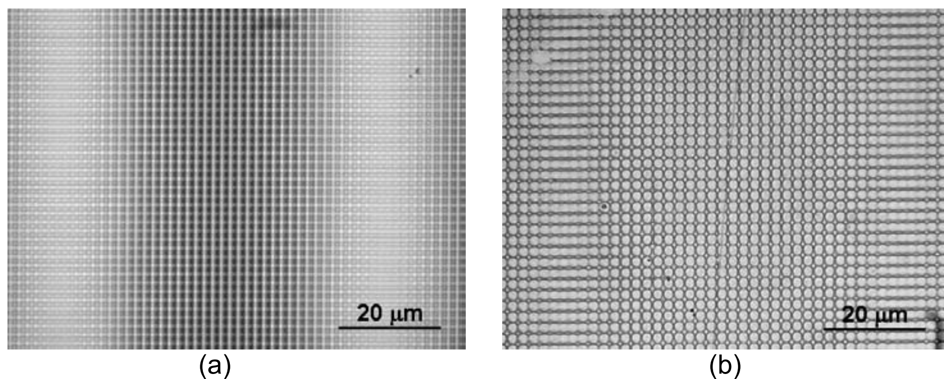

(a) (b)

Fig. 6.5-4: Optical microscope image of (a) the resist grating printed on the *z*- face of sample *M3* and (b) the corresponding surface structure.

The moiré beating geometries and the corresponding structures fabricated here are listed in Tab. 6.5-1. It is important to note that, in every case, the domain pattern obtained by the EFO process on *z*- face faithfully reproduces the resist geometry.

	Sample M1	Sample M2	Sample M3
Moiré process	(*z*+) 2D at 2μm (*z*-) 2D at ~ 2μm	(*z*-) dual 2D (2.4μm; 2.5μm)	(*z*-) 2D at 2.4μm (*z*-) 1D at 2.5μm
Resist grating	(*z*+) 2D at 2μm (*z*-) dual 2D (2μm; 200μm)	(*z*-) dual 2D (2.4μm; 2.5μm)	(*z*-) 2D at 2.4μm + 1D at 2.5μm (channels period 80μm)
Domain structure	(*z*+) 2D pillar at 2μm (*z*-) dual 2D holes (2μm; 200μm)	(*z*-) dual 2D holes (2.4μm; 2.5μm)	(*z*-) 2D holes at 2.4μm + 1D PPLN at 2.5μm (channels period 80μm)

Tab. 6.5-1: Main features of resist gratings and corresponding surface domain structures for the three kinds of samples fabricated here.

6.6 Double-face sub-micron surface structures

This section presents a technique for achieving double-face 1D and 2D sub-micron periodic surface structures in congruent *z*-cut LN crystals, over areas of about (5×5) mm^2. The period of the structures is 2 μm. The technique is based on the following process steps: a) resist coating and HL patterning of *z*- face; b) 200°C bake process to remove the residual photosensitivity of the resist developed on *z*- face; c) resist coating and HL patterning of *z*+ face; d) EFO domain patterning; e) 5 min wet etching in HF solution at room temperature. Different domain pattern geometries are fabricated on *z*+ and *z*- crystal faces to show the reliability of the technique. Sample *M1* in the previous section is an example of double-face patterned sample where the bake process at 200°C of *z*- face has not been performed, thus allowing the moiré effect on *z*- face by using the residual resist photosensitivity. In this Section three different kinds of double-face patterned samples are fabricated: *D1*, *D2* and *D3*.

Sample *D1* is patterned with 1D resist grating on both faces. Figure 6.6-1(a),(b) show the optical microscope images of the *z*- and *z*+ face of the sample *D1*, respectively, after EFO and etching. It is worth noting that several samples have been processed like sample *D1* and the 1D surface structure generated on *z*- face always faithfully reproduces the resist grating in each sample. In contrast, the surface structure fabricated on *z*+ face, even though patterned with the same quality resist grating as *z*-, exhibits a corrupted geometry (see Fig. 6.6-1(b)). This demonstrates that the patterning of *z*- face provides better quality domain gratings.

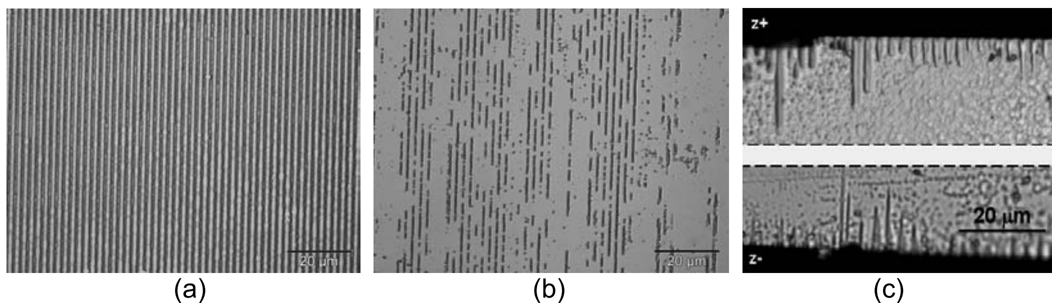

Fig. 6.6-1: Optical microscope image of (a) the etched *z*- face of sample *D1*; (b) the corresponding etched *z*+ face; (c) the corresponding polished and etched *y* face.

Sample *D2* is patterned with a 2D array of resist dots on both faces. Figure 6.6-2(a),(b) show the optical microscope images of the *z*- and *z*+ faces of sample *D2*,

respectively, after EFO and etching. The EFO and etching applied to the array of resist dots clearly gives an array of pillars on *z+* face and an array of holes on *z-* face, as shown also in Section 6.4. Figure 6.6-1(c) shows the optical microscope image of the polished and etched *y* face of sample *D1*. This picture clearly shows that the EFO applied to double-face resist patterned samples generates surface unreversed domains on both faces.

Sample *D3* is fabricated with completely different domain pattern geometries on the two faces. The *z-* face is patterned with a 2D array of resist dots and *z+* face is patterned with a 1D resist grating. Figure 6.6-3(a),(b) show the optical microscope images of the *z-* and *z+* face of sample *D3*, respectively, after EFO and etching.

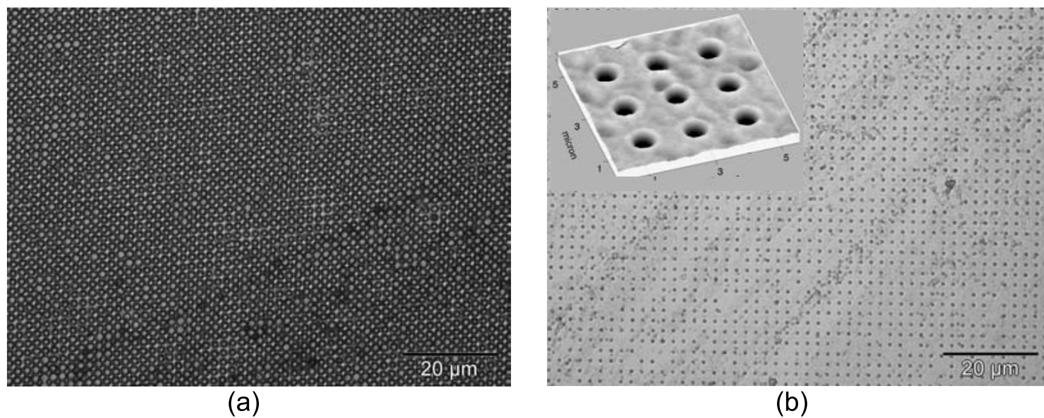

(a) (b)

Fig. 6.6-2: Optical microscope image of (a) the etched *z-* face of sample *D2* and (b) the corresponding etched *z+* face. The inset shows a magnified surface view of the sample *D2*.

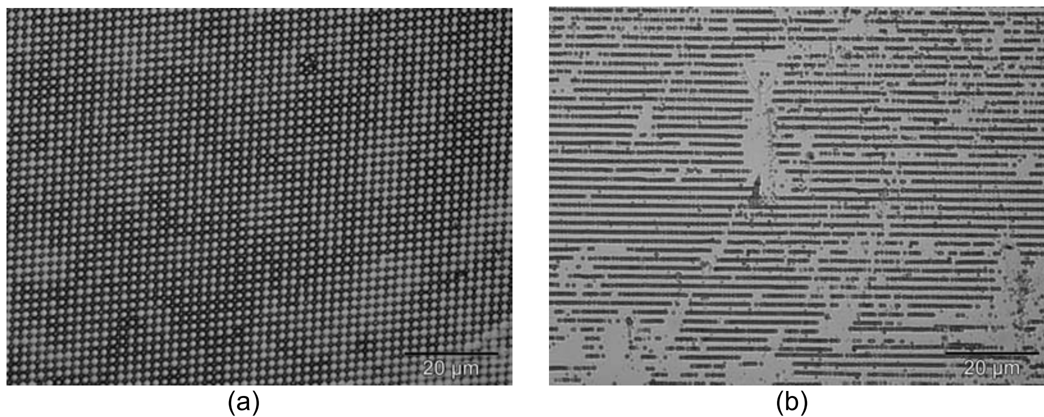

(a) (b)

Fig. 6.6-3: Optical microscope image of (a) the etched *z-* face of sample *D3* and (b) the corresponding etched *z+* face.

The inspection of the polished and etched *y* face of these three samples reveals that the EFO generates unreversed regions under the resist coated areas on both faces, with average depths around 10 μm, largely compatible with waveguide fabrication. Figure 6.6-1(c) shows the optical microscope image of the polished and etched *y* face of sample *D1*, as example.

Figure 6.6-4 shows the optical diffraction pattern of the etched sample *D3*, taken with a He-Ne laser aligned nearly perpendicularly to the *z*+ face.

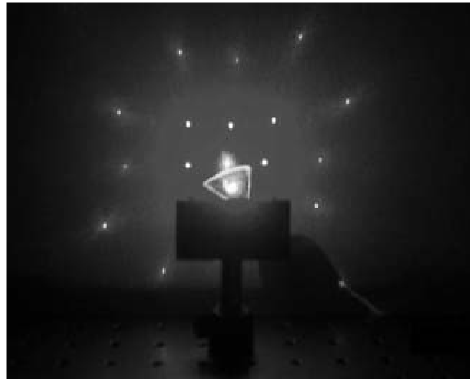

Fig. 6.6-4: Optical diffraction pattern of the sample *D3*.

The resultant diffraction pattern represents the reciprocal lattice of the periodically poled pattern and gives information about the quality of the realized grating. In fact, by scanning the laser beam over the whole structure area of about (5×5) mm^2, the diffraction orders are clear and exhibit constant diffraction angles, thus demonstrating the uniformity of the structures over the whole engineered region. Moreover, the measurement of the diffraction angles is in good agreement with the space periodicity, measured by standard optical microscope.

6.7 Possible applications for novel photonic crystal devices

This section is aimed at proposing the LN structures fabricated here for possible applications in the field of photonic devices. In fact, such structures exhibit specific features which allow to foresee the possibility to fabricate innovative photonic devices exploiting the specific properties of the LN material (EO, PZ, nonlinearity, etc.). Further investigations are currently under consideration in order to demonstrate the actual feasibility of such photonic devices. Moreover, recently the first results have been presented in literature concerning the demonstration of a full photonic band gap in a 2D hexagonally arranged structure fabricated in LN by a technique different from that illustrated in this thesis and based on focused ion beam milling [6,7].

The 1D sub-micron period surface reversed domain gratings (see Fig. 6.4-4) could be used for different purposes in etched as well as un-etched version. In the last case the domain grating could be implemented in waveguide configuration for the fabrication of novel nonlinear devices providing short-wavelength conversions by QPM interaction. Moreover periods down to 300 nm would allow backward nonlinear wavelength interactions. The sub-micron period of these gratings allows to foresee also their implementation in the fabrication of different innovative Bragg reflectors, depending on the etched or un-etched nature of the structure, operating in the infrared wavelength region with subsequent interesting applications in the field of telecommunications. In case of un-etched grating a tunable Bragg reflector device would be possible by exploiting the refractive index step induced electro-optically by appropriate electrodes. In case of etched grating a different tunable Bragg reflector would be possible by using the refractive index step between air and LN where the

tunability could be induced by the EO effect as before or for example by thermal expansion with further applications in the field of sensors.

The 2D short period surface domain gratings after etching could be implemented in planar waveguides for the fabrication of innovative tunable photonic band-gap devices exploiting the refractive index contrast between air and LN and the unique properties of LN (nonlinearity; electro-optics; piezoelectricity; pyroelectricity; etc.).

The moiré method allows to introduce artificial defects in a host photonic band-gap structure, thus providing the possibility to manipulate photons by localizing the electromagnetic states and “trap the light” [8]. For example, photons can propagate through a linear defect within a 2D pattern. This phenomenon may be used in ultra-small optical devices for optical communications.

An interesting advantage of the double-face patterning relies on the possibility to shrink into the same chip size a number of devices twice as many and with completely different geometries on the two faces according to the requirements.

6.8 Periodic domain engineering by proton exchange

A relatively simple approach to inhibit the lateral domain broadening occurring during periodic EFP is demonstrated here. The technique is based on chemical patterning of LN prior to EFP to obtain two materials with slightly different properties, which invert at different poling conditions. Similar technique has previously been proven successful for KTP [9]. The most common patterning technique for LN is proton exchange (PE), which primarily is used for waveguide formation [10]. In the PE process the samples are immersed in a hot acid. The Li^+-ions are then diffusing out from the crystal surface and substituted by H^+-ions. If the exchange is done in a reasonably strong acid most of the Li^+-ions are exchanged and the crystal will go through a phase transition and form a cubic structure, thereby loosing its ferroelectric properties [11]. Under typical exchange conditions a PE layer few micrometers thick is obtained. The material composition and the properties are significantly changed when the crystal undergoes the phase transition, and a sharp interface is formed between the virgin crystal and the PE:LN layer. The exchanged layer is less conductive than the virgin crystal and hence acts as an isolating film in the surface layer when the crystal is exposed to EFP. First the poling conditions for LN and PE:LN are compared. A 500 μm thick *z*-cut congruent LN sample is partly proton-exchanged on the *z*+ face. The polar faces of the sample are coated with a 50 nm thick Al film, except for a (1×5) mm^2 region in the middle of the *z*+ face, that is left uncoated. The sample is immersed in benzoic acid for 3 hours at 240 °C and a 2.7 μm thick PE layer is then formed. The Al film is removed and the sample is contacted with almost saturated KCl liquid electrodes for poling. A 200 ms long triangular electrical pulse of 22.6 kV/mm is applied to the sample while monitoring the poling current. Switching is observed as current flowing in the external circuit between 18.7 kV/mm and 21 kV/mm applied field. No current is further observed at higher field, as shown in Fig. 6.8-1. The sample is then etched in HF solution, and domain reversal is only observed in the un-exchanged regions. Thus, the polarization reversal is selectively inhibited by means of PE, at least for fields below 22.6 kV/mm.

As described in Chapter 2, in conventional periodic EFP an isolating photoresist grating is used to define areas were the domain reversal should take place. In this work a periodic PE grating and simple planar liquid electrodes to obtain the domain

grating is used. No control of the poling current is found necessary. A similar technique has been demonstrated for $LiTaO_3$ where a periodic PE grating is combined with Ta finger electrodes and photoresist isolation to achieve domain patterns of 3.8 μm period in 300 μm thick $LiTaO_3$ samples [12].

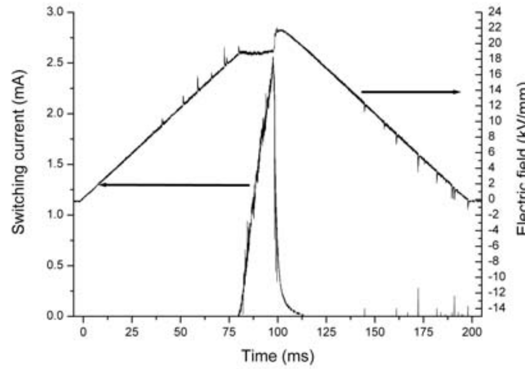

Fig. 6.8-1: Poling current and applied electric field waveforms acquired in case of partly exchanged LN sample.

Samples, (20×20×0.5) mm^3 in size, are obtained by dicing *z*-cut congruent LN wafers. A 21 μm period photoresist grating is fabricated on the *z*+ face with a duty cycle of about 20%, i.e. with 4.2 μm wide resist openings. After deposition of a 50 nm thick Al layer on both *z* faces, the photoresist is removed by lift-off and the Al patterned samples are immersed in a benzoic acid bath at 240°C. After 3 hours the samples are taken out of the melt and allowed to cool down for subsequent Al layer removal. The EFP is performed by applying positive high voltage pulses to the *z*+ face, while the *z*- face is grounded. Electrical contacts to the two faces are obtained using a nearly saturated solution of KCl. Six 25 ms long and 22 kV/mm high pulses are applied to the sample in order to deliver a total charge exceeding the value calculated a priori ($Q=2P_sA$) (see Chapter 2). The voltage value is chosen in order to have domain inversion in the non-exchanged regions only, i.e. with a voltage lower than that required for the PE exchange regions. Figure 6.8-2(a),(b) show the schematic view of the sample cross section after the PE and after the subsequent periodic EFP, respectively.

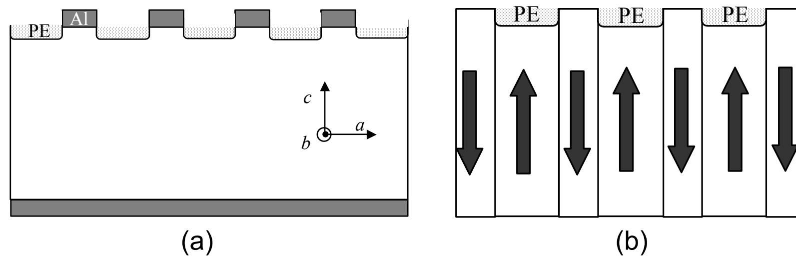

Fig. 6.8-2: Schematic view of the sample cross section (a) after Al patterning and PE; (b) after electric field periodic poling by planar liquid electrodes.

Samples with 1D PE pattern at 21 μm period and 20% duty cycle, namely with around 16.8 μm wide PE regions, have been obtained. They are used to investigate the inhibition of domain spreading by PE. It is well known that the PE regions in LN are selectively etched by HF solution [13], as well as the *z*- side of LN. The latter one is obtained after domain reversal on the patterned side. The PE regions are etched considerably faster than the domain inverted ones, which makes it possible to distinguish between PE, domain inverted and un-inverted LN. Figure 6.8-3 shows the

optical microscope image of the original *z*+ face after EFP and 5 minutes wet etching in HF. The narrower regions are un-etched and correspond to the non-exchanged material, namely to the areas which were protected by Al strips during the PE process. It is important to note that domain reversal is completely inhibited under the PE regions even though the amount of charge delivered to the sample is in excess of the one calculated for the masked area. The reversed domains formed in the non-exchanged regions are stopped from spreading by the PE material and hence keep the width of the Al strips (about 4.2 µm). So the duty-cycle of the reversed domain grating faithfully reproduces that of the chemical pattern. The complete inhibition of lateral domain spreading by the PE process is also shown by the cross section view of the etched sample in Fig. 6.8-4. Figure 6.8-4(a),(b),(c) refer to the regions underneath the patterned face, at about 250 µm depth, and close to the non-patterned face, respectively.

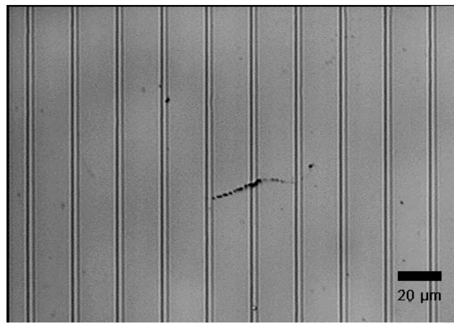

Fig. 6.8-3: Optical microscope image of the reversed domain pattern on the *z*+ face after HF etching.

Figure 6.8-4(a) shows that the PE regions are about 2.7 µm deep. The reversed domains are 4.2 µm wide along the whole sample thickness, and their walls are parallel to the *x*-face. It is reasonable to believe that the domain broadening has been inhibited by the fact that the domains cannot broaden at the surface of the crystal and hence not broaden further down. Therefore they do not take the normal triangular shape that otherwise is common for PPLN. Moreover, Fig. 6.8-4(a) shows that some nucleation has occurred just underneath the PE regions, possibly due to local inhomogeneities in the material.

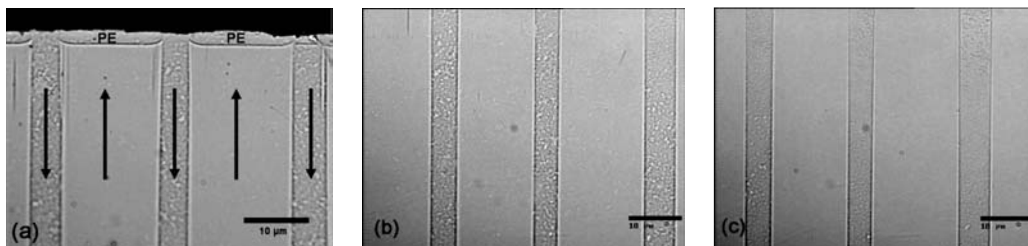

Fig. 6.8-4: Optical microscope image of the *y*-face of the reversed domain pattern (a) underneath the *z*+ face; (b) at about 250 µm depth into the crystal; (c) underneath the unpatterned *z*- face.

However, these tips are no longer than 100 µm indicating that the PE suppresses both the sideways domain growth and the forward growth of domains in PE regions. The forward growth cannot take place because no charge is injected from above through the isolating PE layer.

References Chapter 6

[1] J.P. Spallas, A.M. Hawryluk, D.R. Kania, J. Vac. Sci. Tech. B 13,1973 (1995).

[2] M.L. Shattenburg, R.J. Aucoin, R.C. Fleming, J. Vac. Sci. Tech. B 13, 3007 (1995).

[3] M. Yamada, N. Nada, M. Saitoh, K. Watanabe, Appl. Phys. Lett. 62, 435 (1993).

[4] A.C. Busacca, C.L. Sones, V. Apostolopoulos, R.W. Eason, S. Mailis, Appl. Phys. Lett. 81, 4946 (2002).

[5] O. Kafri and A. Livnat, Opt. Lett. 4, 314 (1979).

[6] M. Roussey, M.P. Bernal, N. Courjal, F.I. Baida, Appl. Phys. Lett. 87, 241101 (2005).

[7] F. Lacour, N. Courjal, M.P. Bernal, A. Sabac, C. Bainier, M. Spajer, Opt. Mat. 27, 1421 (2005).

[8] J.D. Joannopoulos, P.R. Villeneuve, S. Fan, Nature 386, 143 (1997).

[9] H. Karlsson, F. Laurell, Appl. Phys. Lett. 71, 3474 (1997).

[10] C.E. Rice and J.L. Jackel, J. Solid State Chem. 41, 308 (1982).

[11] Y.N. Korkishko, V.A. Fedorov, F. Laurell, IEEE Journal of Selected Topics in Quantum Electronics 6, 132 (2000).

[12] K. Mizuuchi, K. Yamamoto, Appl. Phys. Lett. 66, 2943 (1995).

[13] F. Laurell, J. Webjorn, G. Arvidsson, and J. Holmberg, J. Lightwave Technol. 10, 1606 (1992).

Chapter 7

Electro-optic device based on domain engineered $LiNbO_3$

A LN based electro-optically addressable device with both optical deflector and/or optical switch functionality is presented here. A similar device has been originally developed in [1,2] but for the first time here its operation is visualized by an imaging camera. Moreover, the device is here tested as an amplitude modulator in the mid-infrared region as well, at a wavelength of about 4.3 μm where no Pockels cells are available. The device is based on a LN sample EFP engineered with a sharp boundary, between two oppositely oriented ferroelectric domain regions, along the *y* crystal axis. According to the EO properties of LN (see Chapter 2), equal magnitude refractive index changes of opposite sign occurs between the two adjacent domain regions when applying an external electric field. In this way, the normal EO induced refractive index change is duplicated. Thus, an optical beam crossing the interface along the *x* crystal axis is subject to both reflection and refraction. A great improvement in the angular deflection sensitivity can be obtained by using a so called *grazing angle* geometry, namely when the angle of the beam impinging on the interface approaches the total internal reflection (TIR) limit angle. In this configuration relatively large deflection angles are achievable by using a control signal of a few hundred volts. Moreover, when the incident angle exceeds the limit angle, namely when the TIR phenomenon onsets, the device operation is not continuous, exhibiting an abrupt deflection of the light beam. In other words, in absence of external voltage the light passes through the boundary basically undisturbed, since only a residual poling-induced strain occurring at the boundary can slightly affect the beam propagation. In case of external voltage, an opposite refractive index change is induced across the adjacent reversed domains. In this case, the beam light impinging on the interface at angles larger than the limit, and from the region with increased refractive index, is reflected with a theoretical efficiency of 100%. The angle necessary for TIR, at an EO controlled interface, is given by the usual expression:

$$\sin\theta_{TIR} = \frac{n-|\Delta n|}{n+|\Delta n|} \qquad (7\text{-}1)$$

The refractive index change Δn induced by the external voltage V along the x crystal axis is given by

$$\Delta n = -\frac{1}{2} r_{33} n_e^3 \frac{V}{d} \qquad (7\text{-}2)$$

where r_{33} is the largest EO coefficient accessed by extraordinary *s*-polarized light, n_e is the wavelength dependent value of the extraordinary refractive index and *d* is the device thickness. The induced refractive index change related to *p*-polarized light can be derived from Eq.(7-2) by replacing the EO coefficient r_{33} with r_{13} and the extraordinary refractive index n_e with the ordinary refractive index n_o. Anyway, this

refractive index change is not particularly useful because its value is only about one-third of that obtained using r_{33} and n_e in the above equation. The aforesaid device provides several advantages, including an easy to accomplish fabrication, with the possibility of achieving high contrast ratios, relatively low electric drive power, and finally a wavelength dependence that is much less critical than in other EO devices, such as Pockels cells. In fact, the function of a Pockels cell is characterized by the half wave driving voltage $V_\pi = \lambda / \left(2 n_e^3 r_{33}\right)$ that is directly proportional to the wavelength. In contrast, the switching voltage $V = (d\Delta n) / \left(n_e^3 r_{33}\right)$ of the LN domain engineered device is effectively wavelength independent, because intrinsic wavelength dispersion characteristics of both the EO coefficient r_{33} and the refractive index n_e are almost negligible in a relatively small wavelength range. This feature is particularly interesting in case of spectral ranges where Pockels cells are not available and switching performances faster than that of mechanical chopping are desirable.

The device presented here has been fabricated by the EFP described in Chapter 2 applied to a congruent z-cut both sides polished LN sample 500 μm thick. Half area has been resist patterned through standard mask lithography prior to the application of the external voltage. Figure 7-1 shows the optical microscope image of the fabricated sample after slight conventional etching.

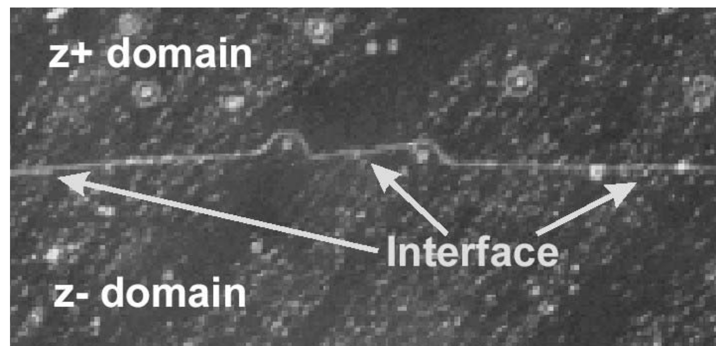

Fig. 7-1: Optical microscope image of the engineered sample after slight conventional etching. The interface between the two reversed domains is clearly visible.

The interface between the two reversed ferroelectric domains is clearly visible. The EO device is fabricated by cutting a (20×15×0.5) mm^3 sized sample from the obtained domain engineered LN wafer and by appropriate polishing the edges to have optical quality facets for light coupling. Gold electrodes are sputtered on both z– and z+ faces across the domain interface, thus allowing the application of an electrical field E_z which induces the refractive index change. The performance of the device is tested for different wavelengths: visible at 632.8 nm; typical telecom at 1532 nm; mid-infrared at 4.3 μm, where Pockels cells are not available.

The device can work as a beam deflector or as an optical switch, based on TIR effect, depending on the set-up used. Both operation modes are characterized by mounting the device on an insulating goniometric support allowing a fine control of the incidence angle of the light beam (see Fig. 7-2). A He-Ne polarized laser source emitting at λ=632.8 nm and with an output optical power of about 1.0 mW is used for characterizing the device in the visible wavelength range. A half-wave plate is inserted at the output of the laser to select the required linear light polarization. The laser beam is focused onto the LN sample edge and the output beam is collected by

means of a (560x800) pixel^2 silicon CCD array with 10 µm pixel size. The electrical CCD output is acquired by a standard PCI frame grabber card.

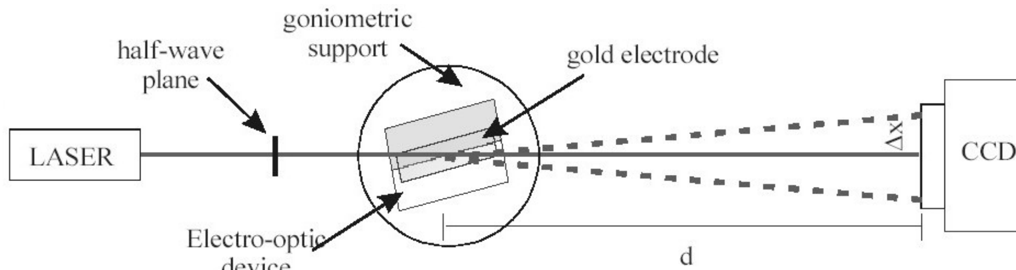

Fig. 7-2: Schematic view of the set-up used to characterize the domain engineered device.

In case of visible wavelength the EO coefficient r_{33} and the extraordinary refractive index n_e are assumed to be 33×10^{-12} m/V and 2.14, respectively [3]. The characterization in the near-infrared range is performed at a telecommunication wavelength by employing a He-Ne laser source emitting at λ=1532 nm (output power of about 5.0 mW) and by replacing the CCD array with an infrared Vidicon camera. Moreover, a GT filter is used instead of the half-wave plate. The device is characterized in the infrared range at about 4.3 µm wavelength generated by a nonlinear difference-frequency process in a periodically poled LN crystal [4]. In this case an InSb liquid-N_2-cooled photodiode and CaF_2 lenses are used. The experimental results, obtained for both operation modes, are illustrated in the following sections.

7.1 Beam deflector

Figure 7.1-1 shows the geometry used for the beam deflection operation in case of incidence angle θ_i smaller than the limit angle θ_{TIR}.

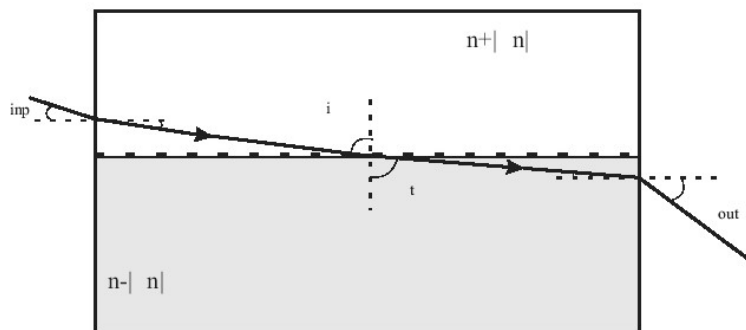

Fig. 7.1-1: Schematic view of the device geometry used in case of beam deflector operation.

Fig. 7.1-2 presents the behaviour of the measured transmission angle θ_t as function of the applied voltage and for different incidence angles at the visible wavelength of 632.8 nm.

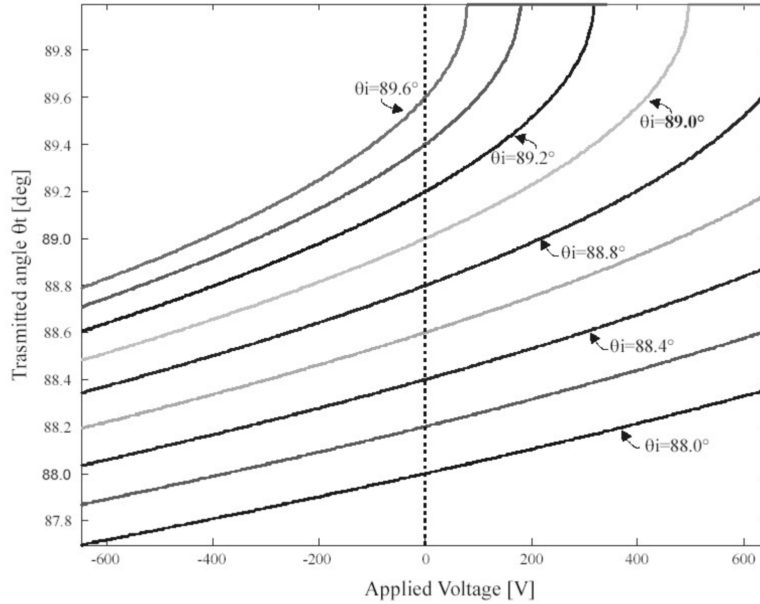

Fig. 7.1-2: Transmission angle measured as function of the applied voltage, for different incidence angles at the visible wavelength of 632.8 nm.

The relationship between the transmission angle and the applied voltage is approximately linear in case of small values of the incidence angle θ_i, such as 88.0° and 88.4°, whereas when the incidence angle approaches 89.0° the TIR phenomenon occurs and the relationship is no more linear. It is worth noting that, differently from other kinds of EO scanner geometries such as the prism based one, the grazing incidence geometry used here is extremely sensitive to small changes of the local refractive index. Substantial beam deflection can be achieved even for low control voltage amplitude when approaching the limit incidence angle. This means that, in order to obtain maximum deflection for a few hundreds of applied voltage, the beam deflector has to be used with an incidence angle approaching the limit angle. The application of a voltage ranging from negative to positive values provides the advantage to have a duplicated total deflection angle. Figure 7.1-3 shows both the simulated and the measured shift of the transmitted optical beam, in the visible range and for three values of the input angle θ_{inp}. The sign of the displacement is related to the initial position (without any voltage) of the light beam, so that the minus (plus) sign corresponds to a separation from the initial position towards right (left). Simulated values are obtained by the following relation:

$$\Delta x = d\ tg\theta_{out} \cong d\ \theta_{out} \tag{7.1-1}$$

where d=20 cm is the distance between the sample and the CCD array (see Fig. 7-2), and θ_{out} is evaluated by taking in account the change of the refracted beam direction at the EO addressed interface and refractions due to both the input and output interfaces between LN and air (see Fig. 7.1-1). Therefore, the application of Snell's law to the three interfaces and of fundamental trigonometrical relations leads to the expression for the output angle θ_{out}:

$$\theta_{out} = \sin^{-1}\left[\left(n - |\Delta n|\right)\sqrt{1 - \left(\frac{n + |\Delta n|}{n - |\Delta n|}\right)^2 \left[1 - \left(\frac{\sin\theta_{inp}}{n + |\Delta n|}\right)^2\right]}\right] \quad (7.1\text{-}2)$$

where Δn is defined in Eq.(7-2). A good agreement between simulated and theoretical values of the transmitted beam displacement is clearly visible in Fig. 7.1-3. The slight discrepancy is mainly due to the non-ideal sharpness of the domain wall interface and to the measurement uncertainty of both the absolute value of the input angle θ_{inp} and of the distance d between the device and the CCD array. The output angle corresponding to an input angle of 2.0° has not been measured for an applied voltage larger than 300 V because the beam is deflected outside the sensitive area of the CCD array and thus not detectable.

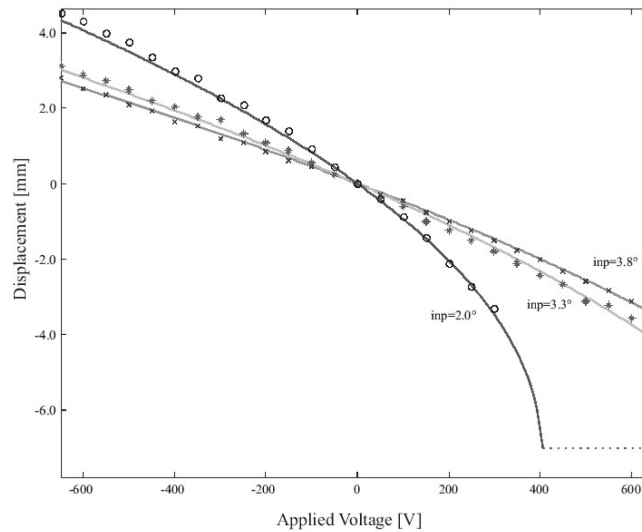

Fig. 7.1-3: Comparison between the simulated and measured displacement of the transmitted optical beam for three different values of the input angle in the visible wavelength range.

In case of 2.0° input angle the theory predicts that for an applied voltage larger than 400 V the TIR effect occurs and thus the deflected beam is no more present. Figure 7.1-4 shows the optical field intensity distribution acquired by the CCD camera at a distance of 20 cm far from the sample in case of three deflected beams corresponding to the same input angle of 3.3° but for three voltage values corresponding to absence of voltage and to the extreme positive and negative values above which the deflected beam is no more detectable: V=0, V=±650 V.

A lateral shift of about 3.5 mm and of about 3.0 mm is measured for the positive and the negative voltage value, respectively. The slight asymmetry is strictly related to the characteristic behaviour of the device as shown in Fig. 7.1-2. In fact, in case of positive voltages the deflector approaches the TIR condition, where a non linear behaviour is detected. In contrast, in case of negative voltages the deflector behaviour is far from the more efficient non linear region.

Figure 7.1-5 shows representative frame of the movie acquired by the CCD camera (see the original movie in Paper XV) showing the evolving propagation direction of the beam under the deflector operation for a voltage value ranging from – 650 V to +650 V.

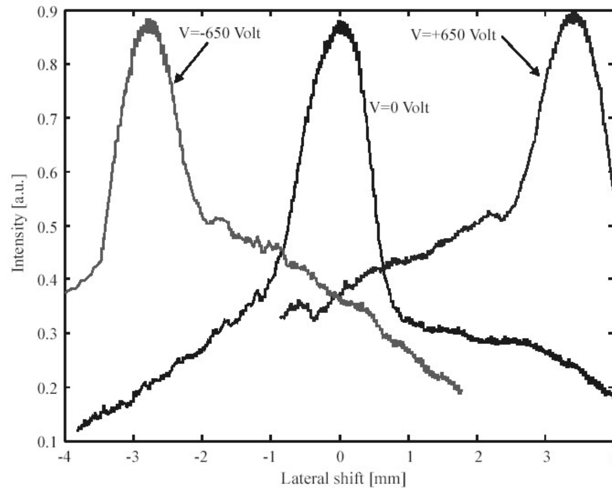

Fig. 7.1-4: Optical field distribution acquired by the CCD at a distance of 20 cm from the device, for three different values of the applied voltage at visible wavelength range.

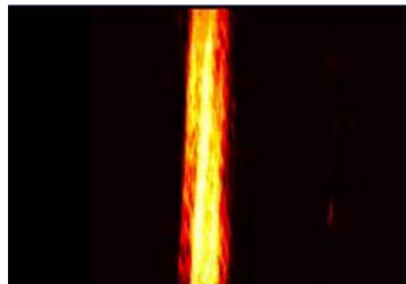

Fig. 7.1-5: Representative frame of the movie showing the evolving beam during the deflector operation (external voltage ranging from –650 V to +650 V). (see the movie in Paper XV)

The acquired movie clearly shows that the device could be used as an optical scanner. The same device is characterized in the near infrared wavelength range by the set-up described previously and Fig. 7.1-6 shows the beam lateral shift obtained placing the Vidicon camera at a distance 27.5 cm from the device. These data obtained for a large input angle θ_{inp} confirm the linear relationship between the applied voltage and the beam lateral shift.

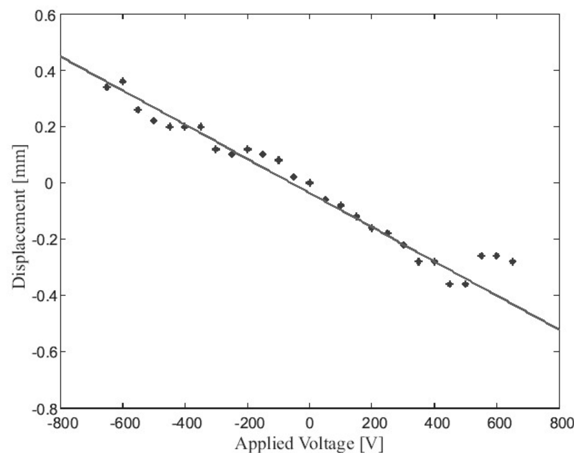

Fig. 7.1-6: Lateral shift of the transmitted beam measured at telecom wavelength of 1532 nm.

7.2 TIR-based switch device

The same device can be used as a digital optical switch by exploiting the TIR effect in order to obtain an abrupt deflection of the light beam from the transmitted path to the reflected one. This effect occurs when the incidence angle θ_i is larger than the limit angle θ_{TIR}. This angle can be evaluated from the Eq.(7-1) for both crystal polarizations, and its value becomes handy only for applied voltage larger than 300 V. The schematic view of the interaction geometry across the device interface is reported Fig. 7.2-1.

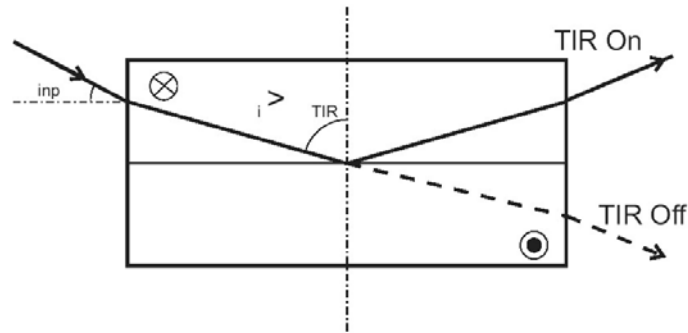

Fig. 7.2-1: Schematic view of the interaction geometry across the device interface in case of the switch operation by exploiting the TIR effect.

The characterization of the switch device is performed at an incidence angle of about 89.0°, determined with an error of ±0.1°. Figure 7.2-2(a) shows the measured behaviour of the reflected beam power as function of the applied voltage, for both *s* and *p* light polarization, in case of visible wavelength at λ=632.8 nm.

The switching of the *s*-polarized light occurs for smaller values of the applied voltage compared to the *p*-polarized light, as expected. In fact, the magnitude of the appropriate EO tensor element for the *s* polarized light is larger than that for the *p* polarized light. An extinction ratio between the TIR-on and the TIR-off state greater then 20 dB is evaluated in case of *p* polarized light.

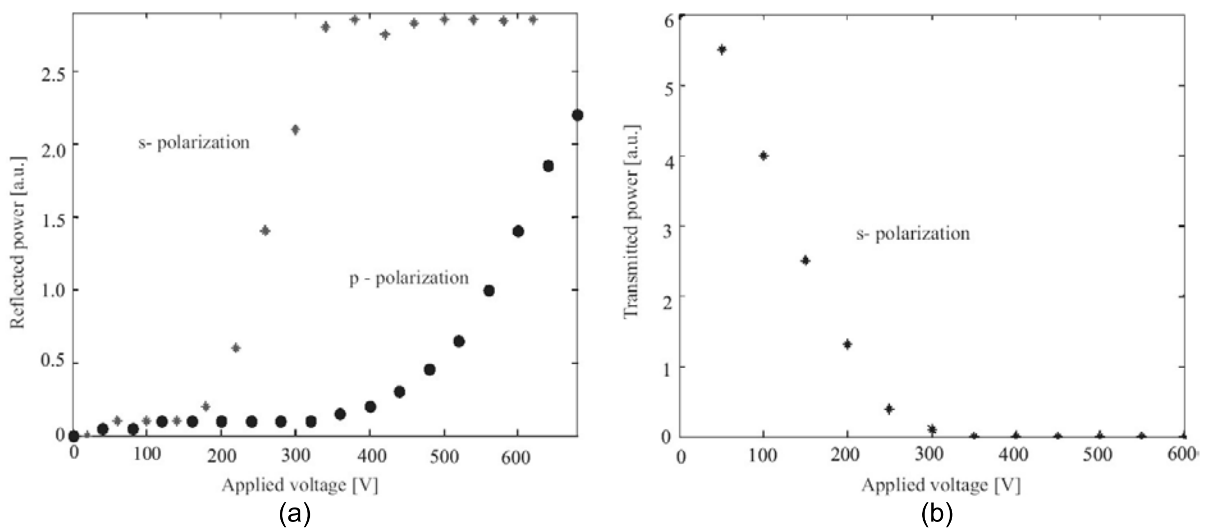

Fig. 7.2-2: Measured behaviour of (a) the reflected beam power for both *s* and *p* polarization state and of (b) the transmitted beam power for the *s* polarization, as function of the applied voltage.

Moreover, Fig. 7.2-2(b) reports the transmitted beam power as function of the applied voltage for the *s* polarization state, namely the more efficient. A contrast of more than 20 dB is reachable also in this case. Figure 7.2-2(a),(b) show that the variation of the reflected and transmitted beam is not sharp in correspondence of the TIR effect. In fact, since the beam is slightly un-collimated, each portion of the beam experiences a different incidence angle and, as consequence, the voltage required for TIR condition is different for each portion of the beam. Therefore, when approaching the TIR condition, the transition from the transmitted to the reflected beam appears smooth. Figure 7.2-3 reports a representative frame of the movie showing the evolving propagation direction of both the deflected and reflected beam for an *s* polarized light at visible wavelength and during the application of an external voltage ranging from 0 V up to +650 V.

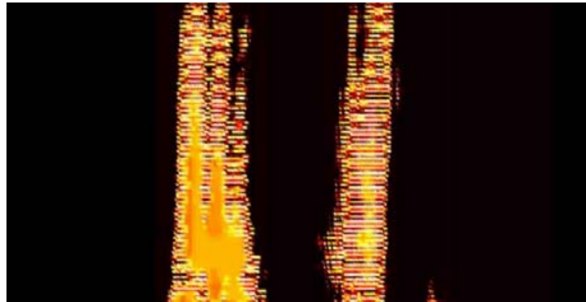

Fig. 7.2-3: Representative frame of the movie showing the TIR functionality of the domain-engineered-based device at the visible wavelength of 632.8 nm. (see the movie in Paper XV)

Even though the image of the optical beam is influenced by the non perfect optical alignment, the behaviour of the device is clearly shown by Fig. 7.2-3 (see the movie in Paper XV). In case the TIR condition is not satisfied both the transmitted angle and the optical reflected power increase with the voltage, whereas in case the TIR condition is fulfilled, the optical transmitted power becomes null and the reflected power gets the maximum value.

The LN TIR switch has been tested with a 4.3 µm optical radiation too. This radiation, generated in a PPLN crystal, is useful for spectroscopy applications [5]. A positive sinusoidal voltage, 500 V peak-to peak, has been applied between the upper and lower golden electrodes of the device. A knife edge stopped the beam transmitted by the internal interface between the two domains. A maximum modulation depth of 70% on the reflected beam has been measured, up to a 10 kHz frequency, limited by the bandwidth of employed high-voltage amplifier. This experiment has demonstrated the possibility to perform amplitude modulation faster than mechanical chopping, in a wavelength region where no Pockels cells are available.

References Chapter 7

[1] A.J. Boyland, S. Mailis, J.M. Hendrickes, P.G.R. Smith, R.W. Eason, Opt. Comm. 197, 193 (2001).

[2] R.W. Eason, A.J. Boyland S. Mailis, P.G.R. Smith, Opt. Comm. 197, 201 (2001).

[3] A. M. Prokhorov and Y. S. Kuzminov, *Physics and Chemistry of Crystalline Lithium Niobate,* Hilger, Bristol, UK (1990).

[4] D. Mazzotti, P. De Natale, G. Giusfredi, C. Fort, J.A. Mitchell, L.W. Hollberg, Appl. Phys. B 70, 747 (2000).

[5] D. Mazzotti, S. Borri, P. Cancio, G. Giusfredi, P. De Natale, Opt. Lett. 27, 1256 (2002).

Chapter 8

Description of the original work and author contribution

Paper I

Whole optical wavefields reconstruction by digital holography
S. Grilli, P. Ferraro, S. De Nicola, A. Finizio, G. Pierattini, R. Meucci
Optics Express 9, 294 (2001).

The potentialities of DH for the whole reconstruction of optical wavefields are investigated here. This paper demonstrates that DH provides quantitative information about the 2D distribution of both the amplitude and phase shift of the object wavefield in correspondence of different reconstruction planes along the propagation direction. The numerical reconstruction of the amplitude and phase shift is performed for both digitally recorded and simulated holograms and the results are presented and discussed. Moreover, hologram patterns affected by astigmatism are also processed to demonstrate the possibility for analysing aberrated wavefronts.

Contributions by the author: The author participated in the experiments, performed the numerical elaborations and wrote the paper.

Paper II

A Mach-Zehnder interferometric system for measuring the refractive indices of uniaxial crystals
S. De Nicola, P. Ferraro, A. Finizio, P. De Natale, S. Grilli, G. Pierattini
Optics Communications 202, 9 (2002).

A new interferometric technique for measuring the ordinary and extraordinary refractive indices of uniaxial crystals is reported here. The technique is based on the measurement of the rotation-dependent phase changes of the optical path length in crystal plates. A FFT based fringe analysis allows to have accurate measurement of the phase shift as a function of the rotation of the sample. The principle of the method is discussed and measurements of the ordinary and extraordinary refractive indices of a $LiNbO_3$ crystal are reported.

Contributions by the author: The author participated in the measurements, discussions and in writing of the paper.

Paper III

Two-dimensional mapping of electro-optic phase retardation in lithium niobate crystals by digital holography
M. de Angelis, S. De Nicola, A. Finizio, G. Pierattini, P. Ferraro, S. Grilli, M. Paturzo, L. Sansone, D. Alfieri, P. De Natale
Optics Letters 30, 1671 (2005).

An accurate 2D mapping of the phase retardation induced by the EO effect in $LiNbO_3$ crystals is reported here. Off-axis DH is used to investigate congruent *z*-cut crystals. The spatially resolved optical path difference is measured by an interferometric procedure while a linearly rising voltage ramp, below the coercive field of the material, is applied to the crystal. This procedure provides information on the uniformity of the electro-optic properties and gives the possibility to detect the presence of crystal defects which is of fundamental importance in the fabrication of $LiNbO_3$ based photonic devices.

Contributions by the author: The author participated in the measurements, digital holography elaborations, discussions and in writing of the paper.

Paper IV

In-situ visualization, monitoring and analysis of electric field domain reversal process in ferroelectric crystals by digital holography
S. Grilli, P. Ferraro, M. Paturzo, D. Alfieri, P. De Natale, M. de Angelis, S. De Nicola, A. Finizio, G. Pierattini
Optics Express 12, 1832 (2004).

A DH based technique is presented here for the first time for monitoring the domain reversal in $LiNbO_3$ by EFP. An interferometric set-up is used to acquire a sequence of holograms of the crystal during the EFP. The 2D distribution of the phase shift, occurring across adjacent opposite domains by the EO and PZ effects, and of the wavefield amplitude are then reconstructed by DH. The amplitude and phase images are collected into movies which provides both qualitative and quantitative *in-situ* information about the domain switching evolution over the *z* crystal face. This technique could be used as a novel tool for *in-situ* visual controlling of the EFP in ferroelectric crystals and thus for high fidelity domain patterning.

Contributions by the author: The author did both the measurements and the DH elaborations and wrote the paper.

Paper V

Characterization of fast dynamic evolution of ferroelectric domains in $KTiOPO_4$ by digital holography
S. Grilli, P. Ferraro, D. Alfieri, P. De Natale, C. Canalias, V. Pasiskevicius, F. Laurell
Submitted to Optics Express.

The DH technique described in Paper IV is here used for *in-situ* visualization and characterization of domain switching in flux-grown $KTiOPO_4$ crystals. Differently from Paper IV here the CMOS camera is strictly required in order to record the very fast switching dynamics exhibited by $KTiOPO_4$. The technique is applied for three different poling voltage waveforms in order to characterize the poling behaviour under different electric field conditions used for domain patterning. High-contrast phase movies of the evolving domains are reconstructed and discussed. The results show how different are the morphology and the dynamics of the reversing domains in $KTiOPO_4$ compared to $LiNbO_3$. The reliability of the technique in case of $KTiOPO_4$, where very fast domain switching exists, allows to foresee its applicability for *in-situ* visual monitoring of domain patterning in $KTiOPO_4$ for which the conventional control of the poling current is not suitable due to the high ionic conductivity.

Contributions by the author: The author designed and built the experimental set-up, did the measurements and the elaborations and wrote the paper.

Paper VI

In-situ visualization of domain kinetics in flux grown $KTiOPO_4$ by digital holography
C. Canalias, V. Pasiskevicius, F. Laurell, S. Grilli, P. Ferraro, P. De Natale
Submitted to Applied Physics Letters.

The technique used in Paper IV is here used for in-situ imaging of domain switching in $KTiOPO_4$ crystals. As in Paper V different electric field conditions are used but the domain reversal dynamics is here investigated for both forward and backward poling. The incubation time, the total poling time and the morphology of the reversing domains are studied in both cases.

Contributions by the author: The author designed and built the experimental set-up and performed the measurements. The author participated in the elaborations, discussions and in writing of the paper.

Paper VII

Evaluation of the internal field in lithium niobate ferroelectric domains by an interferometric method
M. de Angelis, S. De Nicola, A. Finizio, G. Pierattini, P. Ferraro, S. Grilli, M. Paturzo
Applied Physics Letters 85, 2785 (2004).

The evaluation of the IF in a domain engineered congruent $LiNbO_3$ wafer is reported here. The optical path length variation is measured across a domain wall by a non-invasive interferometric method. The $LiNbO_3$ crystal is resist patterned and subjected to EFP to obtain two antiparallel ferroelectric domains. The crystal is then mounted into one arm of a MZ interferometer to study the phase map over the *z* face and to evaluate the effects of domain inversion by a DH technique. The internal field is evaluated by measuring the electro-optically induced phase shift across two antiparallel domains by the IF.

Contributions by the author: The author participated in the measurements, discussions and in writing of the paper.

Paper VIII

Investigation of electric internal field in congruent $LiNbO_3$ by electro-optic effect
M. Paturzo, D. Alfieri, S. Grilli, P. Ferraro, P. De Natale, M. de Angelis, S. De Nicola, A. Finizio, G. Pierattini
Applied Physics Letters 85, 5652 (2004)

The effect of the defect-induced internal field on the EO behaviour of *z*-cut congruent $LiNbO_3$ crystals is investigated here. A spatially resolved interferometric technique allows to measure the phase retardation induced by an external voltage across two adjacent reversed domains. The two opposite domains show different EO behaviour when the experiment is performed just after EFP. The measurements demonstrate the existence of an elastic component of the IF, never explored before.

Contributions by the author: The author participated in the measurements, discussions and in writing of the paper.

Paper IX

On the origin of internal field in lithium niobate crystals directly observed by digital holography
M. Paturzo, P. Ferraro, S. Grilli, D. Alfieri, P. De Natale, M. de Angelis, A. Finizio, S. De Nicola, G. Pierattini, F. Caccavale, D. Callejo, A. Morbiato
Optics Express 13, 5416 (2005).

This paper shows the direct observation of the defect dependence of the IF in $LiNbO_3$ crystals. A full-field interferometric method allows to evaluate the IF across some clusters of defects embedded in a stoichiometric lattice structure. The results show that the value of the IF grows in the proximity of the defects and vanishes far from them, thus addressing the long-standing issue about the origin of the IF in $LiNbO_3$.

Contributions by the author: The author participated in the measurements, discussions and in writing of the paper.

Paper X

Surface topography of microstructures in lithium niobate by digital holographic microscopy
S. De Nicola, P. Ferraro, A. Finizio, S., Grilli, G. Coppola, M. Iodice, P. De Natale, M. Chiarini
Measurement Science and Technology 15, 961 (2004).

This paper deals with the first application of a DH microscope for topography characterization of surface structures realized in congruent $LiNbO_3$. The structures are fabricated by HL insulating patterning, EFP and conventional wet etching. These structures have a range of applications in optical ridge waveguides, alignment structures, V-grooves, micro-tips and micro-cantilever beams where precise control of the surface quality and topography is required. The DH technique allows to obtain digitally a high-fidelity surface topography description of the specimen with only one image acquisition, thus providing relatively simple and compact set-ups able to give quantitative information on object morphology.

Contributions by the author: The author fabricated the samples, participated in the measurements, discussions and in writing of the paper.

Paper XI

Investigation on reversed domain structures in lithium niobate crystals patterned by interference lithography
S.Grilli, P. ferraro, S. De Nicola, A. Finizio, G. Pierattini, P. De Natale, M. Chiarini
Optics Express 11, 392 (2003).

Periodic domain inversion is here performed in $LiNbO_3$ by using resist gratings realized by HL instead of the usual mask lithography process. Furthermore the poling process is investigated in the *overpoling* regime which allows the formation of sub-micron reversed domains. Etching these structures at high rates provides the fabrication of pyramidal-like relief structures which, in principle, could find application in the field of PCs.

Contributions by the author: The author built the interference lithography set-up, arranged the electric field poling set-up, fabricated the samples, participated in the discussions and wrote the paper.

Paper XII

Surface nanoscale periodic structures in congruent lithium niobate by domain reversal patterning and differential etching
S. Grilli, P. Ferraro, P. De Natale, B. Tiribilli, M. Vassalli
Applied Physics Letters 87, 233106 (2005)
[selected for The Virtual Journal of Nanoscale Science & technology].

Novel one and 2D periodic structures fabricated in congruent $LiNbO_3$ with size down to 200 nm are reported in this paper. The periods range from about 2 μm down to 530 nm. HL is used to obtain short pitch insulating gratings, and subsequent EFP, in the overpoling regime is performed for periodic domain inversion. Nanoscale structures are obtained by selective chemical etching, and topographic investigations are performed by AFM. The fabricated structures are attractive in nonlinear optics for short-wavelength conversion and in the field of PCs for Bragg and band-gap applications.

Contributions by the author: The author designed and built the new holographic lithography set-up for sub-micron period patterning, implemented the overpoling process, fabricated the samples, discussed the applications and wrote the paper.

Paper XIII

Double-face and submicron two-dimensional domain patterning in congruent lithium niobate
S. Grilli, P. Ferraro, L. Sansone, M. Paturzo, S. De Nicola, G. Pierattini, P. De Natale
IEEE Photonics Technology Letters 18, 541 (2006).

The fabrication of novel dual-face periodic sub-micron structures in $LiNbO_3$ crystals is reported in this paper. The fabrication technique follows that described in Paper XII with the additional dual-face resist patterning process. HL is used to generate periodic gratings on both faces of *z*-cut crystal samples and EFO and wet etching are used to transfer such gratings onto the substrates as surface structures. Samples with both equal and different geometric structures on the two faces have been fabricated. Such dual-face structures, compatible with waveguide implementation on both faces, would be useful for realizing PC based chips with twice as many devices.

Contributions by the author: The author fabricated the samples, discussed the applications and wrote the paper.

Paper XIV

Control of lateral domain spreading in congruent lithium niobate by selective proton exchange
S. Grilli, C. Canalias, F. Laurell, P. Ferraro, P. De Natale
Accepted by Applied Physics Letters.

The increase of the poling voltage by PE is demonstrated here in case of congruent $LiNbO_3$ crystals. Patterned PE has been used to control the domain nucleation and

inhibit the broadening of reversed domains. Periodically proton exchanged samples have been used to form domain gratings by EFP just using planar electrodes and without need for poling current control. The reversed domain gratings show a duty-cycle faithfully reproducing that of the proton exchanged pattern, thus demonstrating that high-fidelity reversed domain patterning is possible to obtain by a relatively simple process.

Contributions by the author: The author fabricated the samples, participated in discussions and wrote the paper.

Paper XV

Visualization of optical deflection and switching operations by a domain-engineered-based $LiNbO_3$ electro-optic device
G. Coppola, P. Ferraro, M. Iodice, S. De Nicola, S. Grilli, D. Mazzotti, P. De Natale
Optics Express 11, 1212 (2003).

An EO device applied as an optical beam deflector and switch at different wavelengths has been built and tested in this paper. The EO device is based on a domain-engineered $LiNbO_3$ sample. For the first time in this work the operation of such device is visualized by an imaging camera. The device has been characterized both at the visible wavelength (632.8 nm) and at a typical telecom wavelength (1532 nm). Furthermore, the device has been tested as an amplitude modulator in the mid-infrared region as well, at a wavelength of ~4.3 µm, where no Pockels cells are available. A detailed description of this device is given, and the experimental results are discussed.

Contributions by the author: The author fabricated the sample, participated in the experiments, discussions and in writing of the paper.

Chapter 9

Summary

This thesis has focused on two main areas of interest: the high resolution characterization of specific properties of $LiNbO_3$ and $KTiOPO_4$ crystals and the engineering of novel domain structures with sub-micron periods in congruent $LiNbO_3$. All of these techniques make use of interferometric methods and, for the first time to the best of my knowledge, the DH has been used here to characterize ferroelectric crystals.

The characterization experiments have included the accurate measurement of the ordinary and extraordinary refractive indices of $LiNbO_3$ crystals by using an interferometric technique based on an automated FFT fringe analysis. The results demonstrate the possibility to use this technique as a valid alternative to other existing techniques which suffer poorer accuracy. In principle this technique can be applied to any uniaxial crystal.

A DH based technique has been presented for the measurement of the 2D distribution of a selected EO coefficient in $LiNbO_3$ crystals. The results are accurate and the 2D spatially resolved information is of considerable interest in all of those device applications where the pointwise information provided by the existing techniques is not sufficient.

The characterization of different properties related to the EFP has been performed by DH based methods. The first experiment has concerned the investigation of the domain switching dynamics in case of free poling, namely on crystals without insulating patterning. The *in-situ* and non-invasive imaging of domain reversal in $LiNbO_3$ and $KTiOPO_4$ crystals has been presented by making use of the phase shift occurring across adjacent reversed domains due to the linear EO and PZ effects. The 2D amplitude and phase images of the reversing domains are reconstructed and collected into movies. The amplitude movie provides qualitative information about the spatial and temporal evolution of the domain walls while quantitative images of the evolving phase shift occurring across adjacent reversing domains are provided by the phase movie. Such phase shift information gives unambiguous information about the polarization orientation over the sample. These movies are useful for different purposes such as the characterization of the poling kinetics, that of the poling behaviour across crystal defects. Moreover high fidelity control of poling for periodic domain engineering as an alternative to the conventional non-imaging methods can be provided by this approach. The results show that in $LiNbO_3$ the domain reversal basically consists in the formation of a few domain walls across the electrode edges and in their successive evolution spanning the whole area in contact with the liquid electrolyte. The kinetics of the reversing domains has been studied both in slow and fast poling dynamics by exploiting the non-conductive nature of $LiNbO_3$ and by using a CCD and a CMOS camera, respectively. Other techniques are available in literature for *in-situ* video observation of domain walls in $LiNbO_3$ during EFP, but with various limitations which are instead overcome by the procedure proposed in this thesis. All of those methods provide only qualitative information about the domain switching process and are limited b the focus tracking. The technique presented here exploits all of the advantages provided by the DH, including the refocusing of the

image by post-acquisition numerical procedure and the possibility of correcting the eventual aberrations due to the optical components in the acquisition set-up.

In case of $KTiOPO_4$ the domain reversal starts with the formation of different nucleation sites across electrode edges corresponding to the lower conductive regions. The poling then proceeds towards the centre of the sample in the form of reversed regions exhibiting a typical pencil-like shape elongated along the *y* crystal axis. The kinetics of the domain reversal has been studied for different voltage pulse waveforms: square, train of square and triangular pulses. The phase movies of the domain switching evolution are reconstructed and show that more uniform nucleation is obtained in case of triangular pulses. Moreover the "jerking" behaviour observed in case of square pulses appears to be avoided in case of the train waveform. Another method for *in-situ* imaging of reversing domains has been proposed in the past by the Laser Physics Department of The Royal Institute of Technology but the technique presented in this thesis provides phase movies of the reversing domains with better spatial and temporal resolution. In these measurements the use of a non-conventional camera based on CMOS technology has been strictly required for the appropriate acquisition of domain switching in a ferroelectric crystal like $KTiOPO_4$ for which very fast domain switching has been found out.

The DH based technique for the *in-situ* imaging of domain walls has also been used here in static mode for the *in-situ* investigation of the IF in $LiNbO_3$ by using external fields lower than the coercive field of the material. The IF in $LiNbO_3$ and similar crystals is well known in the field. Various theoretical interpretations have been proposed in literature but further investigations remain desirable. The quantitative measurement of the IF in $LiNbO_3$ presented in literature has been mainly performed by evaluating the asymmetric behaviour of the polarization hysteresis loop. On the contrary this thesis has presented a technique for the *in-situ* direct evaluation of the IF intensity in congruent $LiNbO_3$ by making use of the EO and PZ effects induced by this field. Moreover the results of the experiment in case of off-congruent $LiNbO_3$ samples provide a direct and experimental demonstration of the strong relationship existing between the IF and the crystal defects, thus opening the way to a deeper understanding of the effects related to the IF in domain engineering of $LiNbO_3$ crystals.

A simple domain engineered $LiNbO_3$ device has been fabricated in this thesis and the corresponding operation as switching or deflector device has been presented in the visible and IR wavelength region.

Finally the recent results concerning the engineering of ferroelectric domains in $LiNbO_3$ crystals have been presented. A PE patterning has been used in congruent LiNbO3 for selective increment of the coercive field. The results for relatively large periods around 20 μm show that high fidelity domain patterning has been achieved by this technique thus foreseeing the possibility to use of this technique for realizing bulk dense gratings. An overpoling technique, relatively easy to accomplish, has been instead implemented for the fabrication of sub-micron period 1D and 2D reversed domain patterns. The depth of these structures is compatible with waveguide configuration, thus allowing their use for the fabrication of new QPM devices for UV generation. The selective wet etching has been used to transfer such domain patterns onto the substrate as surface structures with different 1D, 2D and also more complicated geometries which open the way to possible applications in the field of PCs for optical fibre telecommunications. In fact, the implementation of such PC devices basically requires a material with high refractive index, waveguide compatibility and possibility for surface engineering at sub-micron scale. Thus the

fabrication of novel surface periodic structures at sub-micron scale presented here together with the relatively high refractive index of $LiNbO_3$ and the well established technology for waveguide fabrication in this material can be considered promising for future implementation of innovative PC based devices in $LiNbO_3$. PCs based on $LiNbO_3$ material would provide additional functionalities compared to the emerging ones fabricated on semiconductor substrates. In fact, the EO and nonlinear properties of $LiNbO_3$ would provide the possibility o manipulate the light by light itself in PC based devices.

List of acronyms

LN - Lithium Niobate or $LiNbO_3$
KTP – Potassium Titanyl Phosphate or $KTiOPO_4$
EO – Electro-Optic
PZ – Piezoelectric
SHG – Second Harmonic Generation
OPO – Optical Parametric Oscillator
QPM – Quasi Phase matching
EFP – Electric Field Poling
PEFP – Periodic Electric Field Poling
PPLN – Periodically Poled Lithium Niobate
PPKTP – Periodically Poled KTP
HVA – High Voltage Amplifier
AFM – Atomic Force Microscope
DH – Digital Holography
CCD – Charge Coupled Device
ESPI – Electronic Speckle Pattern Interferometry
DSPI – Digital Speckle Pattern Interferometry
FFT – Fast Fourier Transfrom
MZ – Mach Zehnder
OPL – Optical Path Length
GT – Glan Thompson
WFA – White Filled Area
RG – Reflective Grating
RGI – Reflective Grating Interferometer
CMOS – Complementary Metal Oxide Semiconductor
SP – Single Pulse
TSP – Train of Square Pulses
TP – Triangular Pulse
IF – Internal Field
OPD – Optical Path Difference
OCLN – Off Congruent Lithium Niobate
SEM – Scanning Electron Microscope
EFO – Electric Field Overpoling
HL – Holographic Lithography
M – Michelson
TB – Two Beams
LM – Lloyd’s Mirror
HF – Hydrofluoric Acid
PLS – Pillar Like Structure
HLS – Hole Like Structure
GLG – Grid Like Geometry
DLG – Dot Like Geometry
PC – Photonic Crystal
PE – Proton Exchange
TIR – Total Internal Reflection
PCI – Peripheral Component Interconnect

Acknowledgements

This thesis is the result of several years of work and I wish to express here my gratitude to the people that helped and supported me during this adventure.

I would like to thank Paolo De Natale and Pietro Ferraro (CNR-INOA, Naples) for different reasons. Paolo, thanks to your idea to start my studies in the Laser Physics Group headed by Fredrik Laurell, the birth of this work was possible. Pietro, my home supervisor, thanks a lot for your great support and encouragement in my studies and experiments related to this PhD work during my Research Grant first and Researcher position later in CNR-INOA.

I wish to thank Fredrik Laurell and Valdas Pasiskevicius for accepting me as PhD student in their Laser Physics Group in KTH. Fredrik, thank you for sharing your knowledge and for always supporting and appreciating my efforts and work. Moreover I cannot forget the great fun and laughs we had together out of work. Fredrik, I know that you are very busy but I hope that one day you will have time for a tennis match with me… do not forget that my invitation is always valid!

I would like to thank all my colleagues in Naples:Melania Paturzo, Lucia Sansone, Domenico Alfieri, Felice Pignatiello, Andrea Finizio, Giovanni Pierattini, Sergio De Nicola, Marella de Angelis. Thank you for your support, help and enthusiasm although the difficulties in working with a shark!

I thank Giuseppe Coppola and Mario Iodice from CNR-IMM (Naples) for sharing the experiments on the $LiNbO_3$ switch and for the fruitful discussions.

I would like to thank Bruno Tiribilli and Massimo Vassalli from CNR-ISC (Florence) for sharing their knowledge about the AFM and for the fruitful discussions.

I would like to thank Carlota Canalias (KTH) for so many reasons that I fear to forget something. First of all, you were always at my disposal for helping me in the labs in KTH although you were very busy. Thank you also for sharing experiments and research discussions always with pleasure and enthusiasm. Thank you for staying by my side when some days things in the lab never worked! Thank you for the great hospitality and for providing me with a wonderful stay in Stockholm during my Swedish periods. We had a lot of fun and laughs that helped me in feeling at home. I wait for you in Naples.. we still have a lot of calamari to fight with!

I would like to thank Junjii Hirohashi for the fruitful discussions and support in the lab. Your kindness and help was really precious in many occasions!

Many thanks to Jonas Hellström and På Jelger for solving computer problems.

I would like to thank Prof. Jens A. Tellefsen for helping me in different occasions. Thank you for your hospitality and for arranging my stay in Stockholm.

I would like to thank Agneta Falk for always being helpful and for all kinds of assistance.

I would like to thank my parents and my whole family for their unconditional support and love and for making the physical distance unnoticeable during my stays in Stockholm.

Finally, special thanks to Luigi, I cannot find the words but I try. Thank you for your love, understanding, supporting, care… always and especially in the hard times of this life! Thank you so much for helping me in formatting this thesis as best as possible. Thank you for being so patient every time the stress at work tried to spoil my life with you. Thank you for reminding me of what is important in life. You changed my life in such a wonderful way! Thank you!